# Active Integrated Optic Devices for Sensing: Optical Rate Gyroscopes and Stellar Interferometers

by

Hsien-kai Hsiao

A dissertation submitted in partial fulfillment
of the requirements for the degree of
Doctor of Philosophy
(Electrical Engineering)
in The University of Michigan
2010

Doctoral Committee:

Professor Kim A. Winick, Chair
Professor Almantas Galvanauskas
Professor Herbert G. Winful
Associate Professor John D. Monnier

Dedicated to my loving wife, Kuei-yu, and my caring parents, Mei-chi and Tsang-hai

and in memory of my grandmother, Bi-yue

# ACKNOWLEDGEMENTS

First, I would like to express the deepest gratitude to my research advisor and doctoral committee chair, Professor Kim A. Winick, for his support and guidance throughout my PhD study. Since joining his research group in 2004, I have been feeling that I am very fortunate to have him as my mentor, who always finds the time to help me with the research problems and provides insightful advices, always encourages me when I am stuck with the experiments under deep frustration, and always has faith in me. Without his invaluable technical and editorial guidance, I would never have been able to complete this dissertation. In addition, it is my great honor to have him as the witness to my wedding in Ann Arbor and the special guest at my wedding reception in Taiwan in 2010.

I would also like to thank other doctoral committee members, Professor John D. Monnier, Professor Almantas Galvanauskas and Professor Herbert G. Winful, for their time and effort to assist in this endeavor and other academic activities. The opportunity to work with Professor Monnier on the astronomy project as part of this dissertation is highly appreciated. His constant support and expertise in astronomical imaging are essential to the completion of the astronomy work. I enjoyed taking the photonic crystal class and optical waves in crystal class taught by Professor Galvanauskas, and nonlinear optics class taught by Professor Winful. They have been very helpful to my education in optics.

Special thanks go to Dr. Guangyu Li and Dr. Tobias Eckhause for their training and help in the integrated optics laboratory. Dr. Li always offers her professional

advices and warm friendship when I am in need. I enjoyed working and discussing research problems with Dr. Eckhause when he was in our research group as a post-doctoral researcher. Dr. KK Wong receives my deep thanks for his advices on the lithium niobate work.

I must also acknowledge the excellent support from the staff members at the University of Michigan: Gregory Allion, Jim Kulman, Edward Tang, Steven Sostrom, and Phil Collica from the Lurie Nanofabrication Facility; Michelle Chapman, Shonda Bottke, Ann Pace, Karen Liska, Beth Stalnaker, and Beth Lawson from the Department of Electrical Engineering and Computer Science.

I would also like to thank all my friends: Yi-hao Chen, Hsun-yi Chen, Dr. Richard Hou, Dr. Wei-chen Chien, Dr. Mingyuan Cheng, Dr. Tsai-wei Wu, Dr. Meng Cui, Yi-chen Tu, Chih-heng Chen, Chun-wei Chang, Hao-wei Pang, Chih-hao Sun, Iris Liu, Frank Hsieh, Peter Ho, Ojas Kulkarni, Malay Kumar, Nigel Wu, Chu-Sheng Yang, Dr. Dingyuan Chen, Mei-yi Chung, and many others for their friendship and joyful company in Ann Arbor.

Last but not least, I would like to thank my loving wife, Kuei-yu, for her support and love. She makes me the happiest man in the world. I am very grateful to my parents, Mei-chi and Tsang-hai, for their endless support, understanding, and love. Without them, it would not have been possible for me to finish my PhD education. My grandfather, Feng-chin, and other family members also receive my deepest gratitude and love, especially to my brother, Hsien-wen, for taking care of our parents while I was away from home.

# TABLE OF CONTENTS

# LIST OF FIGURES

**Figure**

# LIST OF TABLES

**Table**

# LIST OF APPENDICES

**Appendix**

# ABSTRACT

## Active Integrated Optic Devices for Sensing: Optical Rate Gyroscopes and Stellar Interferometers

by

Hsien-kai Hsiao

Chair: Kim A. Winick

The concept of integrated optics was first conceived by Miller at AT&T Bell Laboratories in 1969. In the intervening years, this field has attracted significant attention and has led to the development of multi-functioned, miniaturized, optical devices on a single chip. Integrated optical devices are free from the alignment and stability issues that bedevil bulk optical devices and systems. Integrated optics has much in common with semiconductor integrated circuit technology. As with this later technology, integrated optical devices can be produced using batch processing techniques, such as optical and e-beam lithography, thin film deposition and etching. Integrated optical circuits, comprising optical devices interconnected via channel optical waveguides, have been fabricated on a wide range of substrates, including crystals, glasses, polymers and semiconductors. Integrated optical devices are now widely deployed in fiber optic telecommunication systems and as sensor components. This thesis is a theoretical and experimental study of two new integrated optical sensors. The first is an integrated optic ring resonator gyroscope for measuring angular rotation rate, and the second is an integrated optic beam combiner for astronomical stellar interferometry.

Although passive integrated optic ring resonators for gyroscopes have been previously reported, little work has been performed for active rings. The operation of ring resonator gyroscopes is based on the Sagnac effect. According to this effect, optical beams counter-propagating along the ring will experience a phase difference proportional to the ring's rotation rate. The sensitivity of the gyroscope is limited by the propagation losses in the ring, and hence can be improved by the introduction of loss-compensating gain inside the ring. In this thesis the first active ring resonator for gyroscopic applications is designed, fabricated and characterized. A 1.6 cm diameter active ring resonator is fabricated in a neodymium-doped glass by silver ion exchange. The finesse of the ring resonator is measured and is observed to increase from approximately 11 to 250 when the neodymium ions inside the ring are optically pumped to produce gain. The saturation of the gain medium is also observed as the injected signal strength increases. The ultimate sensitivity of a ring resonator gyroscope is shown from theoretical considerations to be fundamentally limited by the spontaneous emission noise generated within the gain medium. In a passive cavity ring resonator gyroscope the improvement in the noise-limited sensitivity is inversely proportional to the increase in the resonator finesse. In this thesis it is demonstrated that the noise-limited sensitivity of an active (i.e., one with gain) ring resonator gyroscope only increases as the reciprocal of the square-root of the improvement in resonator finesse, and thus the full benefit of the gain cannot be realized.

Astronomical imaging techniques based on interferometric (i.e., beam combining) methods have a long history dating back to Albert Michelson's seminal work at the Mt. Wilson observatory in 1890. Starting with Kern's work in 1996, the use of integrated optics for telescope beam combining has been pursued. In the context of interferometric imaging, integrated optic beam combiners offer many advantages over conventional bulk optic implementations, including spatial mode filtering, enhanced stability and a small, robust platform. To date, integrated optic beam combiners

have only been demonstrated at wavelengths below 2 $\mu$m. Operation in the mid-IR, however, is highly desirable. In this thesis an integrated optic beam combiner for stellar interferometry that operates in the mid-IR is demonstrated for the first time. In particular, a two-beam, integrated optic, combiner is fabricated on a lithium niobate substrate for operation in the vicinity of 3.4 $\mu$m. White light, mid-infrared, fringes, as well as electro-optic on-chip fringe scanning, is demonstrated in the laboratory for the first time using an integrated optical device. Some interferometric imaging applications, such as nulling, require achromatic, i.e., wavelength insensitive, beam combining. As proposed by Bracewell, one important use of nulling interferometers is to search for planets lying outside of our solar system. Integrated optic reversed Y-junction beam combiners are achromatic, but suffer a 3 dB power loss. On the other hand, the widely used asymmetric two waveguide directional couplers are in principle lossless, but they do not achieve broadband, achromatic, beam combining. In this thesis, a theoretical design technique, based on a three waveguide directional coupler, is developed to achieve fully achromatic, broadband, polarization-insensitive, lossless beam combining. This design may make it possible to achieve the very deep broadband nulls needed for exoplanet searching.

# CHAPTER I

# Introduction

## 1.1 Overview

The concept of integrated optics (IO) was first conceived by Miller at AT&T Bell Laboratories in 1969 [1]. In the intervening years, this field has attracted significant attention and has led to the development of multi-functioned, miniaturized, optical devices on a single chip. Integrated optical devices are free from the alignment and stability issues that bedevil bulk optical devices and systems. Integrated optics has much in common with semiconductor integrated circuit technology. As with this later technology, integrated optical devices can be produced using batch processing techniques, such as optical and e-beam lithography, thin film deposition and etching. Integrated optical circuits, comprising optical devices interconnected via channel optical waveguides, have been fabricated on a wide range of substrates, including crystals, glasses, polymers and semiconductors. Integrated optical devices are now widely deployed in fiber optic telecommunication systems and as sensor components.

During the past decade, there has been a rapidly growing interest in new classes of IO-based sensors. These sensors have been implemented using a wide variety of waveguide components, including interferometers, resonators and couplers. IO sensors are compact, immune to electromagnetic interference, free of alignment issues and can provide high sensitivity. Furthermore active functionalities, such as electro-optic,

acousto-optic, and thermo-optic control can be incorporated on-chip.

This thesis is a theoretical and experimental study of two new integrated optical sensors. The first is an integrated optic ring resonator gyroscope for measuring angular rotation rate, and the second is an integrated optic beam combiner for astronomical stellar interferometry. Although passive integrated optic ring resonators for gyroscopes have been previously reported, little work has been performed for active rings. The operation of a ring resonator gyroscope is based on the Sagnac effect. According to this effect, optical beams counter-propagating along the ring will experience a phase difference proportional to the ring's rotation rate. The sensitivity of the gyroscope is limited by the propagation losses in the ring, and hence can be improved by the introduction of loss-compensating gain inside the ring. In this thesis the first active ring resonator for gyroscopic applications is designed, fabricated and characterized. The device is a 1.6 cm diameter active ring resonator fabricated in a neodymium-doped glass by silver ion exchange. The finesse of the ring resonator is measured and is observed to increase from approximately 11 to 250 when the neodymium ions inside the ring are optically pumped to produce gain. The saturation of the gain medium is also observed as the injected signal strength increases. The ultimate sensitivity of a ring resonator gyroscope is shown from theoretical considerations to be fundamentally limited by the spontaneous emission noise generated within the gain medium. In a passive cavity ring resonator gyroscope the improvement in the noise-limited sensitivity is inversely proportional to the increase in the resonator finesse. In this thesis it is demonstrated that the noise-limited sensitivity of an active (i.e., one with gain) ring resonator gyroscope only increases as the reciprocal of the square-root of the improvement in resonator finesse, and thus the full benefit of the gain cannot be realized.

Astronomical imaging techniques based on interferometric (i.e., beam combining) methods have a long history dating back to Albert Michelson's seminal work at the

Mt. Wilson observatory in 1890. Starting with Kern's work in 1996 [2], the use of integrated optics for telescope beam combining has been pursued. In the context of interferometric imaging, integrated optic beam combiners offer many advantages over conventional bulk optic implementations, including spatial mode filtering, enhanced stability and a small, robust platform. To date, integrated optic beam combiners have only been demonstrated at wavelengths below 2 $\mu$m. Operation in the mid-IR, however, is highly desirable. In this thesis an integrated optic beam combiner for stellar interferometry that operates in the mid-IR is demonstrated for the first time. In particular, a two-beam, integrated optic, combiner is fabricated on a lithium niobate substrate for operation in the vicinity of 3.4 $\mu$m. White light, mid-infrared, fringes, as well as electro-optic on-chip fringe scanning, is demonstrated in the laboratory for the first time using an integrated optical device. Some interferometric imaging applications, such as nulling, require achromatic, i.e., wavelength insensitive, beam combining. As proposed by Bracewell, one important use of nulling interferometers is to search for planets lying outside of our solar system. Integrated optic reverse Y-junction beam combiners are achromatic, but suffer a 3 dB power loss. On the other hand, the widely used asymmetric two waveguide directional couplers are in principle lossless, but they do not achieve broadband, achromatic, beam combining. In this thesis, a theoretical design technique, based on a three waveguide directional coupler, is developed to achieve fully achromatic, broadband, polarization-insensitive, lossless beam combining. This design may make it possible to achieve the very deep broadband nulls needed for exoplanet searching.

## 1.2 Dissertation outline

This dissertation consists of five chapters and several appendices. In Chapter II, the design of a 1.6 cm diameter neodymium-doped, glass waveguide, active ring resonator is described, and the fabrication and characterization of the device is pre-

sented. The finesse of the resonator, operating in the vicinity 1.06 $\mu$m, is measured and shown to increase from approximately 11 to 250 when the neodymium medium inside the ring is pumped to produce optical gain. The finesse value of 250 corresponds to an effective propagation loss on the order of 0.013 dB/cm, which we believe to be the lowest value reported to date for rings of this size. The fundamental sensitivity of an optical ring resonator gyroscope is also investigated in Chapter II, and it is shown to be limited by the spontaneous emission noise generated by the gain medium. A closed form expression for the quantum-limited noise performance of the device is derived.

In Chapter III, the design, fabrication and characterization of integrated optic, astronomical, two-beam and three-beam, interferometric combiners for operation in the astronomical L band (3 $\mu$m - 4 $\mu$m) are described for the first time. The devices are fabricated in titanium-indiffused, x-cut lithium niobate substrates. White light fringes are demonstrated in the laboratory using a thermal source, and on-chip, electro-optic fringe scanning is also demonstrated.

In Chapter IV, we describe the theoretical design of a broadband, achromatic, polarization-insensitive, lossless astronomical beam combiner. The device is designed to operate in the mid-infrared and is based on three coupled waveguides. The inner waveguide is uniform along the propagation direction, while the two outer waveguides vary identically along the direction of propagation. Device operation is modeled using coupled mode theory. The three-waveguide structure supports three local normal modes, and the operation of the device is based on the adiabatic evolution of these modes as they propagate along the length of the structure. Adiabatic mode evolution is generally achieved by requiring the waveguide parameters to vary slowly along the direction of propagation. Using a technique introduced by Ishikawa [3], an alternate and more general method of achieving adiabatic operation is used in this chapter to design the beam combiner. This technique allows adiabatic operation to be achieved

with a device of relatively short length. The operation of the device is confirmed using numerical beam propagation. Possible candidate material systems for mid-IR waveguides are also studied in Chapter IV. One particular system, Ge strip waveguides on a silicon substrate is analyzed for operation in the astronomical N band (8 $\mu$m - 12 $\mu$m).

Finally, the contributions of this thesis are summarized and future work is suggested in Chapter V.

# CHAPTER II

# Planar Glass Waveguide Ring Resonators with Gain

## 2.1 Introduction

Planar integrated optic ring resonators have been well-studied and find a host of applications in both telecommunications and sensing. These include optical filtering [4, 5], nonlinear optics [6], optical switching [7], chemical and biological sensing [8] and angular rotation rate sensing [9]. Many of these applications require a resonator of high finesse, and thus a resonator having low loss. When the application also necessitates the use of a large diameter ring, as is the case for an optical gyroscope rotation rate sensor, glass becomes an ideal substrate material because it permits the fabrication of very low loss waveguides.

When two counter-propagating beams of light propagate along a common path in a rotating reference frame, they will experience a phase difference proportional to the rate of rotation. This phenomena, known as the Sagnac effect, is the basis upon which all optical gyroscopes operate [10, 11]. The first passive, free-space, ring resonator gyroscope was proposed and demonstrated by Ezekiel and Balsamo [12] in 1977. Their gyroscope was constructed by a HeNe laser, a pair of acousto-optic (AO) frequency shifters, and a square-shaped cavity made out of aluminum with length 17.5 cm on

a side. Two beams splitters and two mirrors were placed in the four corners of the cavity, and one of the cavity mirrors was mounted on a piezoelectric transducer so that the cavity length can be modulated. The gyro operation was closed-loop and the AO frequency shifts were adjusted in such a way that the counter-propagating beams were driven to their respective cavity resonances. The uncertainty in the measured rotation rate was estimated to be 0.05 deg/hr. Later in 1981, Meyer et al. demonstrated a gyroscope based on Ezekiel and Balsamo's idea where the bulk optics cavity was replaced by a fiber optic loop [13]. The device was constructed using a passive fiber-optic ring resonator of length 3.1 m, and a sensitivity of 0.5 deg/hr was achieved. The first planar ring resonator were reported by Haavisto and Pajer in polymethyl methacrylate films and this work was later extended to glass using ion exchange [14, 15]. These resonators had large propagation losses on the order of 2 dB/cm. Losses of approximately 0.1 dB/cm can now be achieved by ion exchange for ring radii on the order of 1 cm [16], and losses half as large have been reported for similarly sized waveguide rings fabricated using CVD-deposited silica on silicon together with reactive ion etching of the waveguide structure [17]. Currently there are no known methods for achieving even lower loss value for rings of this size. Waveguide losses can be attributed primarily to inhomogeneities in the glass and/or surface roughness at the core-cladding interface. Both of these contributing factors can be reduced by decreasing the refractive index contrast between the core and cladding. Such a decrease, however, will result in significant bending losses unless the ring diameter is increased commensurately. It is possible, however, to reduce the effective resonator loss below the values quoted above by incorporating gain inside the ring. With the presence of gain, lasing in erbium-doped, planar, waveguide, ring resonators has been reported in both glass [18] and $LiNbO_3$ [19] substrates. When operated below the lasing threshold, these devices exhibited a modest reduction of their resonant bandwidths, and hence an increase in finesse. In this chapter we

will study active, integrated optic, ring resonator gyroscopes. The remainder of this chapter is divided into five sections.

In Section 2.2, the basic configurations and the operating principle of an optical rate gyroscope will be discussed.

In Section 2.3, the spectral resolution of an active ring resonator is analyzed. The spectral resolution of a passive ring resonator is limited by shot noise and is a function of the finesse of the resonator and the input signal power level. When gain is added to the ring, the resolution is ultimately limited by spontaneous emission noise generated by the gain medium. In Section 2.3, we derive an expression for this resolution using an analysis previously developed for ring laser gyroscopes [20]. Our analysis shows that in the quantum limit with gain present, the spectral resolution decreases as one over the square root of the product of the finesses of the resonator measured with gain and without gain. We apply this result to determine the minimum, rms, angular rotation rate, random walk error achievable by an active, ring, resonator gyroscope in the quantum limit. A closed-form expression is also derived for the absorbed pump power required by an active ring resonator gyroscope as a function of the launched signal power and the finesse.

In Section 2.4, the fabrication and the characterization of silver ion exchanged waveguides are presented.

The fabrication of an active, waveguide, ring resonator in a neodymium-doped glass by silver ion exchange is described in Section 2.5 and the device is experimentally characterized. When the neodymium gain medium is pumped by a laser diode, the finesse of the 1.6 cm diameter device increases from approximately 10 to 250 at a signal wavelength of 1060 nm, with the later finesse value corresponding to an effective propagation loss value of approximately 0.013 dB/cm. We believe that this is the lowest effective propagation loss and highest finesse reported to date for glass, waveguide, ring resonators of this size. We also observe gain saturation in this ring

resonator as the launched signal power is increased, and we report lasing action at sufficiently high pump powers.

Additional comments on active ring resonator gyroscopes are given in Section 2.6.

## 2.2 Background

### 2.2.1 Types of gyroscopes

The ability to navigate in the absence of external markers is known as *inertial* navigation, and it is an essential element of many commercial and military systems. Inertial navigation systems were originally developed by Germans during World War II.

By measuring the force exerted on a small mass attached to a platform, the linear acceleration of the mass, and hence that of the platform, can be determined in the platform's coordinate system. This information, however, is insufficient to determine the linear acceleration of the platform relative to a fixed external coordinate system, since the accelerometers are attached to the platform and rotate with it. Thus the motion of a platform has six degrees of freedom, three of which are associated with its linear acceleration (in its own frame of reference), and three of which are associated with its angular orientation. Knowledge of the platform's angular orientation, together with its linear acceleration (in its own frame of reference), can be used to determine the linear acceleration of the platform in some fixed external frame of reference. By twice integrating the values of the linear acceleration, computed in this external reference frame, the location of the platform relative to a fixed external reference frame can be found at any future time provided the platform's initial position is known.

Linear accelerometers are relatively easy to construct. For example, the displacement of a small mass attached to a spring, with known spring constant, will yield

a measurement of the applied force and hence the linear acceleration of the mass. Angular orientation, or equivalently angular rotation rate, is more difficult to measure. Rotation rate sensors can be either mechanical or non-mechanical. Until fairly recently, mechanical rotation sensors relied on gimbaled spinning mechanical gyroscopes. The gimbals holding the gyroscope are a set of three rings, initially oriented at right angles to one another, and each gimbals has its own set of bearings. As the platform rotates so do the gimbals, but the spinning gyroscope maintains its orientation. By measuring the angular position of the gimbals relative to the axis around which the gyroscope is spinning, the rotation of the platform may be determined. Mechanical spinning gyroscope rotation rate sensors have, for the most part, been replaced by a newer generation of devices.

There are three general types of gyroscopes that are widely deployed today for inertial navigation and rotation rate sensing. For any particular application, the selection of the type of gyroscope will depend upon performance, complexity, and cost considerations. The first gyro type is a Micro-Electro Mechanical System (MEMS) device [21, 22]. For this gyro, rotation sensing relies on vibrating mechanical elements. In one particular implementation, the out-of-plane motion of a vibrating element will be induced by rotation, and the amount of this motion is electrically sensed and converted to a rotation rate. MEMS gyros are relatively inexpensive and can be easily fabricated using standard semiconductor batch processing methods. MEMS gyros, however, have relatively low sensitivity and accuracy, and these devices are susceptible to errors induced by mechanical vibration and acceleration. The second and the third types of gyros are ring laser gyros (RLG) and interferometric fiber optical gyros (IFOG), respectively, and the operation of both of these are based on the Sagnac effect.

In 1913, G. Sagnac demonstrated inertial rotation sensing by optical means for the first time. When two counter-propagating beams of light propagate along a common

path in a rotating frame of reference, these beams will experience a phase difference that is proportional to the rate of rotation. This phenomenon is known as the Sagnac effect. By combining this effect with optical interferometry, inertial rotation rate sensing devices that have no moving parts can be built [23]. Although RLG and IFOG optical gyros are highly sensitive, accurate, robust, and immune to mechanical vibrations, they are difficult to build and are expensive.

A variant of the IFOG and RLG is the integrated optic ring resonator gyro (IROG), and the active version of this device is the subject of this chapter. The IROG is a promising candidate for some applications due to its small size and the fact that it can be manufactured using standard, low-cost, batch, semiconductor processing. Furthermore, IROGs are also compact, robust, and immune to environmental effects. The basic configurations for RLG, IFOG and IROG optical gyroscopes are shown in Figure 2.1. The operation of RLG requires a bi-directional ring gas laser, where the counter-propagating laser beams are coupled out of the ring laser cavity and beat against each other. Due to the Sagnac effect, the beat frequency is proportional to the angular rotation rate of the ring. An IFOG consists of a fiber loop and a directional coupler. An external optical source, launched into the input port of the device, is split by the directional coupler to produce two counter-propagating beams inside the loop. These beams combine interferometrically at the output port to yield an optical intensity that varies sinusoidally as a function of the relative phase difference between the counter-propagating beams. According to the Sagnac effect, the phase difference is proportional to the angular rotation rate of the fiber loop. Thus by measuring the intensity at the output port, the angular rotation rate can be determined. Generally, long fiber coils (i.e., several km) are required for IFOG to achieve high sensitiviy and accuracy for rotation rate measurements. The operation of IROG is described in Section 2.3.

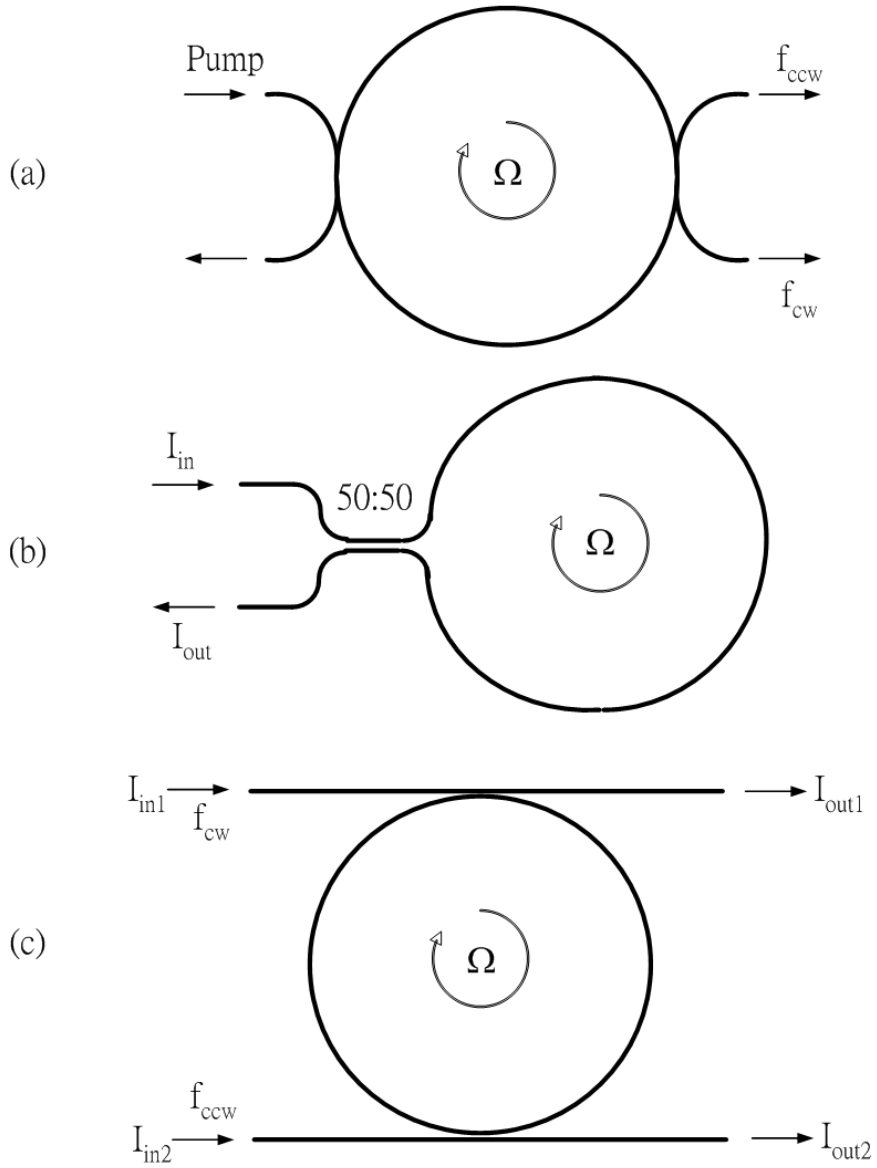


Figure 2.1: Three basic configurations of optical gyroscope for rotation rate sensing: (a) RLG (b) IFOG (c) IROG.

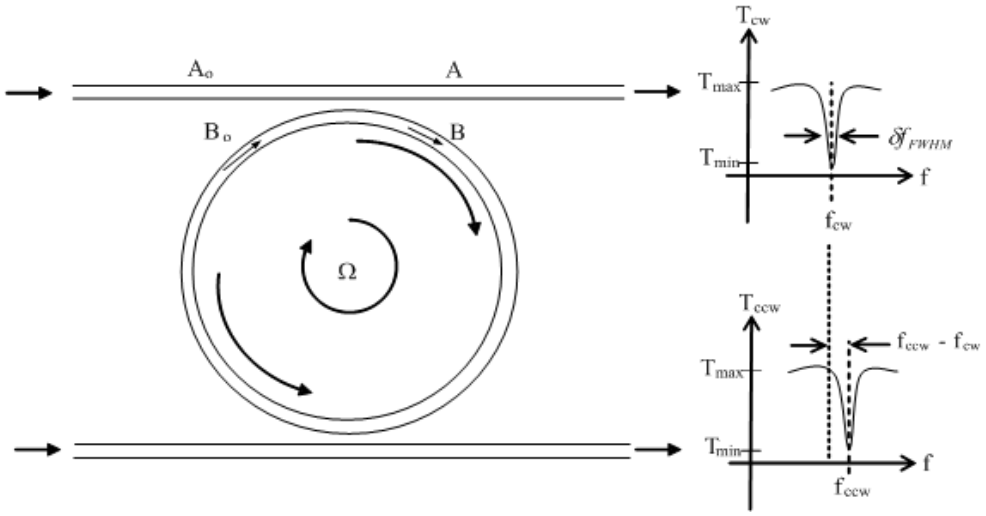


Figure 2.2: Double arm ring resonator.

### 2.2.2 Equations of ring resonators

Consider the double-arm ring resonator shown in Figure 2.2 consisting of a circular ring located in close proximity to two straight waveguides that serve to couple light into and out of the ring. The electric field amplitudes, $A$, $A_0$, $B$ and $B_0$, indicated in Figure 2.2 can be related to one another by [24]

$$A = A_0\sqrt{1-K_{cw}} - jB_0\sqrt{K_{cw}} \tag{2.1}$$

$$B = -jA_0\sqrt{K_{cw}} + B_0\sqrt{1-K_{cw}} \tag{2.2}$$

$$B_0 = B\sqrt{1-K_{ccw}}\exp(-\frac{\rho}{2}L - j\beta L) \tag{2.3}$$

where the coupling coefficient, $K_{cw}$, equals the fraction of optical power coupled into the ring from the top straight waveguides, $L$ is the ring circumference, $1 - \exp(-\rho L)$ equals the fraction of optical power lost upon one round-trip around the ring neglecting coupling losses to the straight waveguides and $\beta$ is the propagation constant. For simplicity, we have neglected any excess insertion losses associated with the coupling

between the straight waveguides and the ring. Combining Eqs. (2.1)– (2.3) yields [24]

$$T(\phi) \equiv \left|\frac{A}{A_0}\right|^2 = 1 - \frac{(1-x^2)(1-y^2)}{(1-xy)^2 + 4xy\sin^2(\phi/2)} \tag{2.4}$$

where

$$x \equiv \sqrt{1-K_{ccw}}\exp(-\frac{\rho}{2}L) \tag{2.5}$$

$$y \equiv \sqrt{1-K_{cw}} \tag{2.6}$$

$$\phi \equiv \beta L = \frac{2\pi}{\lambda}N_{eff}L = \omega N_{eff}L/c \tag{2.7}$$

and the coupling coefficient, $K_{ccw}$, is the fraction of power coupled into the ring from the lower straight waveguide, $\lambda$ is the free-space optical wavelength, $\omega$ is the optical frequency in rad/s and $N_{eff}$ is the effective index of the guided mode. It will be assumed that light is launched into the ring only from the top straight waveguide. The transmittance $T$ achieves a minimum when $\phi$ equals an even integer multiple of $\pi$, corresponding to resonance in the ring. Using Eq. (2.4), the depth, $D$, of the resonance "dip" can be expressed as

$$D \equiv \frac{T_{max} - T_{min}}{T_{max}} = \frac{4xy(1-x^2)(1-y^2)}{(1-xy)^2(x+y)^2} \tag{2.8}$$

and the full-width of the resonance at half maximum, $\delta\phi_{FWHM}$, is equal to

$$\delta\phi_{FWHM} = 2\cos^{-1}\left(\frac{2xy}{1+x^2y^2}\right) \tag{2.9}$$

where this width is defined by the relationship

$$\frac{T(m\pi \pm \delta\phi_{FWHM}/2) - T_{min}}{T_{max} - T_{min}} = 1/2 \tag{2.10}$$

The resonator finesse, $F$, is given by

$$F \equiv \frac{2\pi}{\delta\phi_{FWHM}} = \frac{2\pi c/N_{eff}L}{\delta\omega_{FWHM}} \tag{2.11}$$

where $\delta\omega_{FWHM}$ is the full-width-half-maximum of the resonance in rad/s. Eqs. (2.9) and (2.11) reduce to

$$F \approx \frac{\pi}{1-xy} \tag{2.12}$$

when $xy \approx 1$. The ratio of the power in the ring at resonance to that of the launched power in the straight waveguide is given by

$$\left|\frac{B}{A_0}\right|^2 = \frac{1-y^2}{(1-xy)^2} \tag{2.13}$$

According to Eq. (2.8) the dip will be maximized, achieving a value of 1, when $x = y$. Furthermore when $x = y \approx 1$, Eqs. (2.12) and (2.13) can be combined to yield

$$\left|\frac{B}{A_0}\right|^2 \approx F/\pi \tag{2.14}$$

By measuring the dip and finesse, both the coupling efficiency, $\sqrt{1-K_{ccw}}\exp(-\rho L/2)$ and $K_{cw}$ can be found using Eqs. (2.8), (2.9) and (2.11). When light is launched into the ring using only the bottom straight waveguide, all of the expressions given above remain valid provided that the two coupling coefficients, $K_{cw}$ and $K_{ccw}$, are interchanged in these formula.

## 2.3 Spectral resolution of active ring resonator in quantum limit

Figure 2.2 shows a double arm ring resonator functioning as a resonant optical gyroscope. Light is launched into each of the two resonator arms from separate

laser sources and these two light beams counter-propagate along the ring. In the absence of rotation, the resonance frequencies for propagation in both the clockwise and counter-clockwise directions are given by

$$f_m = m\frac{c}{N_{eff}L} \tag{2.15}$$

where $c$ is the vacuum speed of light and $m$ is positive integer. Due to the Sagnac effect the resonant frequencies, $f_{m,cw}$ and $f_{m,ccw}$, corresponding to the counter-propagating beams will differ when angular rotation takes place about an axis normal to the plane of the ring. The difference in these frequencies is given by [23]

$$f_{m,ccw} - f_{m,cw} = \frac{4A}{\lambda_m L}\Omega \tag{2.16}$$

where $A$ is the area enclosed by the ring, $L$ is the perimeter of the ring, $\lambda_m = c/f_m$ and $\Omega$ is the angular rate of rotation around an axis normal to the plane of the ring. Thus the angular rotation rate can be determined by measuring this frequency difference. Resonant optical gyroscopes were proposed and demonstrated using fiber optics by Ezekiel et al. [12, 13]. Several groups have implemented these gyros using planar, glass, waveguide rings in place of optical fibers [25, 26].

The ultimate accuracy with which the frequency difference, $f_{m,ccw} - f_{m,cw}$, can be measured using a passive resonant optical gyro is limited by shot-noise and is given by [13]

$$\begin{aligned} \delta\Omega_{rms} &\approx \left(\frac{\lambda_m L}{4A}\right)\left[\frac{\sqrt{2}\delta\omega_{FWHM}/(2\pi)}{\sqrt{\eta_D \frac{P_{in}}{hf_m}\tau_{int}}}\right] \\ &= \left(\frac{\lambda_m c}{4AN_{eff}}\right)\left[\frac{\sqrt{2}}{F_c\sqrt{\eta_D \frac{P_{in}}{hf_m}\tau_{int}}}\right] \text{ rad/s} \end{aligned} \tag{2.17}$$

where $\delta\Omega_{rms}$ is the rms, angular rotation rate, random walk error, $\eta_D$ is the detector's

quantum efficiency, $h$ is Planck's constant, $\tau_{int}$ is the observation interval (i.e., detector integration time) and $P_{in}$ is the total power launched bi-directionally into the ring, with half of the power propagating in each direction. Thus the accuracy of the passive resonant gyro can be improved by reducing the width of the resonance,$\delta\omega_{FWHM}$, or equivalently by increasing the finesse,$F_c$, of the ring resonator by reducing propagation losses in the ring. A resonant optical gyroscope of ring perimeter $L$ can, in theory, achieve the same shot noise-limited accuracy as a Sagnac-based interferometric fiber optic gyroscope of fiber length $LF_c/3$ [12, 23]. This effective length enhancement by a factor of $LF_c/3$ is the principal theoretical advantage of a resonant optical gyroscope as compared to a nonresonant, fiber-optic, interferometric gyroscope. The complexity of a resonant optical gyroscope, however, is considerably higher, and other parasitic effects, like Kerr nonlinearities, may make it difficult to achieve the fundamental performance limits given by Eq. (2.17).

The finesse of the resonator can be increased by including gain inside the ring to compensate for propagation loss. Fiber-based, active, ring resonators have been studied both theoretically and experimentally [27–29]. In the presence of gain, the ultimate accuracy of a resonant optical gyroscope will be limited by the spontaneous emission noise inside the ring rather than by shot noise at the detector. Using an analysis technique similar to that employed for ring laser gyroscopes [20], it will be shown below that, in the presence of gain, spontaneous emission noise limits the accuracy of a resonant optical gyroscope to a value given by

$$\delta\Omega_{rms} \approx \left(\frac{\lambda_m c}{4AN_{eff}}\right)\left[\frac{1}{\sqrt{F_c F_a}\sqrt{\frac{P_{in}}{hf_m}\tau_{int}}}\right] \text{ rad/s} \tag{2.18}$$

where $F_c$ is the ("cold" cavity) finesse of the resonator in the absence of gain and $F_a$ is the finesse when gain is present.

For simplicity, a number of assumptions will be made in our analysis. It will be

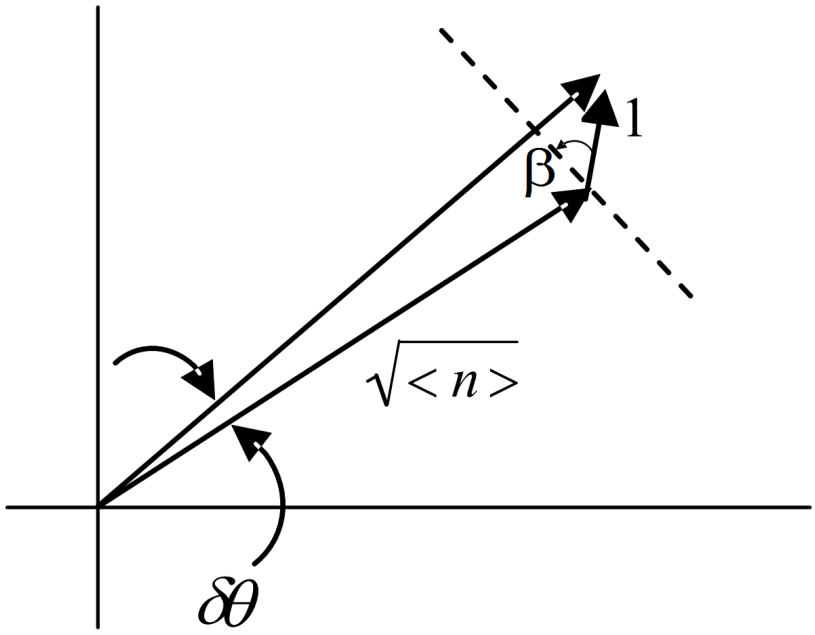


Figure 2.3: Effect of spontaneous emission on frequency.

assumed that the gain is produced by a transition between two levels of an atomic system, e.g., the ${}^4F_{3/2} \rightarrow {}^4I_{11/2}$ neodymium transition. The atomic population in the upper excited level (${}^4F_{3/2}$) will be denoted by $N_2$, while the lower level (${}^4I_{11/2}$) of the transition will be assumed to be unpopulated. The atomic transition will be assumed to be purely homogeneously broadened with a center transition frequency of $f_a$ Hz (wavelength $\lambda_a$), a full-width-half-maximum linewidth of $\delta\omega_a$ rad/s, a stimulated emission cross-section of $\sigma_e$ and a spontaneous emission lifetime of $\tau_{fl}$. The losses in the resonator in the absence of gain will be assumed to be relatively low, and when gain is present, it will be assumed that the gain compensates nearly all of the propagation losses in the ring.

Let $< n >$ denote the average number of photons inside the ring cavity. Thus the strength of the electric field inside the cavity will be proportional to $\sqrt{n}$ and can be represented by a vector as shown in Figure 2.3. The angular position of the vector indicates the phase of the optical field. The short vector in Fig. 2.3 has a length of 1 and represents the spontaneous emission of a single photon from an excited

atom of the gain medium into a single cavity mode. The angular orientation, $\beta$, of this vector relative to the dashed reference line shown in Figure 2.3 is random and uniformly distributed over the interval $[0, 2\pi)$. The addition of this spontaneously emitted photon changes the phase of the optical field in the cavity by $\delta\theta$. Assuming that $< n > \gg 1$, it may be concluded that

$$\delta\theta \approx \frac{1 \cdot \cos\beta}{\sqrt{< n >}} \tag{2.19}$$

and thus

$$< (\delta\theta)^2 > \approx \frac{1}{2 < n >} \tag{2.20}$$

Therefore the total change, $\delta\phi$, in phase of the optical signal field after $M$ photons have been produced by $M$ independent spontaneous emission events that occur in a time interval of duration $\tau_{int}$ will be given by

$$< [\delta\phi(\tau_{int})]^2 > \approx \frac{M(\tau_{int})}{2 < n >} \tag{2.21}$$

In a time interval of $\tau_{int}$ seconds the number of photons, $M(\tau_{int})$, that are spontaneously emitted into a single cavity mode is given by

$$M(\tau_{int}) = \frac{\tau_{int}}{\tau_{fl}} \frac{N_2}{s} \tag{2.22}$$

where $s$ is the number of cavity modes in the ring resonator. $s$ can be found by using the fact that the number of modes per unit volume per unit Hertz is given by [30]

$$\rho_b(f) = \frac{8\pi}{\lambda_a^2} \frac{n_r^3}{c} \tag{2.23}$$

where $n_r$ is the refractive index of the ring. A homogeneous transition has the fol-

lowing Lorentzian spectral lineshape

$$S(f) = \frac{1}{1 + [\frac{2(f-f_a)}{\delta f_a}]^2} \tag{2.24}$$

and the area under this lineshape curve is equal to $\frac{\pi \delta f_a}{2}$. Thus it follows that

$$s = \frac{8\pi}{\lambda_a^2} \frac{n_r^3}{c} V \frac{\delta \omega_a}{4} = \frac{2\pi}{\lambda_a^2} \frac{n_r^3 V}{c} \Delta \omega_a \tag{2.25}$$

where $V$ is the volume occupied by the ring resonator cavity and $\lambda_a$ is the wavelength at the center of the atomic transition. The cold cavity photon lifetime, $\tau_p$, is given by

$$\tau_p = \frac{n_r L/c}{1 - x^2 y^2} \tag{2.26}$$

where $x$ and $y$ are given by Eqs. (2.5) and (2.6). The reciprocal of the cold cavity photon lifetime is approximately equal to the full-width-half-maximum of the cold cavity resonance provided the resonator loss is small, i.e.,

$$\frac{1}{\tau_p} \approx \delta \omega_{FWHM} = \frac{2\pi c}{n_r L F_c} \tag{2.27}$$

where the second equality in Eq. (2.27) follows from Eq. (2.11). The round trip gain, $G$, in the ring is given by

$$G = \exp(\sigma_e N_2 L/V) \approx 1 + \sigma_e N_2 L/V \tag{2.28}$$

It is assumed that the gain nearly compensates the resonator loss, and therefore the following condition is met

$$x^2 y^2 G \approx 1 \tag{2.29}$$

Combining Eqs. (2.26), (2.28), (2.29) yields

$$N_2 \approx \frac{V}{\sigma_e L}(1 - x^2 y^2) = \frac{n_r L}{\sigma_e c}\frac{1}{\tau_p} \tag{2.30}$$

From the Einstein A and B relationship, it follows that [31]

$$\sigma_e = \frac{1}{2\pi}\frac{1}{\tau_{fl}}\frac{\lambda_a^2}{n_r^2 \Delta\omega_a} \tag{2.31}$$

The total optical power, $P_c$, circulating in the resonator can be related to the average number of photons, $< n >$, in the resonator propagating in each direction by

$$< n >= \frac{n_r P_c L}{2 h f_a c} \tag{2.32}$$

Combining Eqs. (2.21), (2.22), (2.25), (2.27) and (2.30)– (2.32) yields

$$< [\delta\phi(\tau_{int})]^2 >= \frac{2\pi\tau_{int} h f_a c^2}{F_c P_c n_r^2 L^2} \tag{2.33}$$

Now according to Eq. (2.14)

$$P_c \approx \frac{1}{\pi} F_a P_{in} \tag{2.34}$$

Also note that

$$< [\delta f_{cw}]^2 >=< [\delta f_{ccw}]^2 >=< [\delta\phi(\tau_{int})]^2 > /(2\pi\tau_{int})^2 \tag{2.35}$$

Combining Eqs. (2.33)– (2.35) yields the following expression for the frequency resolution of an active ring resonator in the quantum limit.

$$(\delta f_{cw})_{rms} = (\delta f_{ccw})_{rms} \approx \frac{c}{\sqrt{2} n_r L}\frac{1}{\sqrt{F_c F_a}\sqrt{\frac{P_{in}}{h f_a}\tau_{int}}} \tag{2.36}$$

It follows from Eqs. (2.16) and (2.35) that

$$\delta\Omega_{rms} =< [\delta\Omega]^2 >^{1/2}= \frac{\lambda_a L}{4\sqrt{2}\pi A\tau_{int}} < [\delta\phi(\tau_{int})]^2 >^{1/2} \tag{2.37}$$

Combining Eqs. (2.33), (2.34) and (2.37) yields the final result for the gyro sensitivity in the quantum limit

$$\begin{aligned} \delta\Omega_{rms} &\approx \left(\frac{\lambda_a c}{4An_r}\right)\left[\frac{1}{\sqrt{F_c F_a}\sqrt{\frac{P_{in}}{hf_a}\tau_{int}}}\right] \\ &= \left(\frac{\lambda_a c}{4An_r}\right)\left[\frac{1}{F_c\sqrt{F_a/F_c}\sqrt{\frac{P_{in}}{hf_a}\tau_{int}}}\right] \text{ rad/s.} \end{aligned} \tag{2.38}$$

A comparison of Eqs. (2.17) and (2.38) indicates that in the quantum limit, the reduction in the rms, angular rotation rate, random walk measurement error is proportional to $1/\sqrt{F_a/F_c}$ rather than to $1/(F_a/F_c)$ when gain is included in the resonator ring. Thus doubling the finesse by using gain only reduces the quantum-limited measurement error by a factor of $\sqrt{2}$ rather than by a factor of 2.

Consider now the operation of the resonant optical gyroscope shown in Figure 2.2 operating under the following conditions: (1) $K_{cw} = K_{ccw} \approx 0$, (2) the gain exactly cancels the propagation loss along the ring, i.e., $\rho_a = 0$, and (3) $\rho_c \approx 0$, where $\rho_c$ and $\rho_a$ denote the propagation loss coefficient, $\rho$, in the ring when gain is absent and present, respectively. It follows from Eq. (2.12) that

$$F_c \approx \frac{\pi}{1-(1-K_{cw})\exp(-\rho_c L/2)} \approx \frac{2\pi}{\rho_c L} \tag{2.39}$$

and

$$F_a \approx \frac{\pi}{K_{cw}} \tag{2.40}$$

Therefore the inclusion of gain will reduce the rms angular rotation measurement

error by a multiplicative factor equal to

$$\text{Reduction Factor} = \sqrt{\frac{F_a}{F_c}} \approx \sqrt{\frac{\rho_c L}{2K_{cw}}} \tag{2.41}$$

As a numerical example suppose the propagation loss in the ring, without gain, is 0.05 dB/cm, the ring diameter is 2 cm and the coupling coefficient is 0.1%, then $F_c \approx 86$, $F_a \approx 3140$ and the measurement error reduction factor due to the inclusion of gain is approximately 6. According to Eq. (2.41), an arbitrarily large improvement in performance should be attainable, in theory, by reducing the coupling coefficient, $K_{cw}$. According to Eqs. (2.34) and (2.40), however, the power, $P_c$, circulating in the ring at resonance is inversely proportional to $K_{cw}$. i.e.,

$$P_c = \frac{P_{in}}{K_{cw}} \tag{2.42}$$

where $P_{in}$ is the power launched into the straight waveguides. Thus as $K_{cw}$ is reduced, the power in the ring increases, and this in turn increases the gain saturation. Furthermore as the gain saturation increases additional pump power is required to maintain the required level of loss compensation, i.e., $\rho_a = 0$. An expression for the required absorbed pump power is derived below

$$\sigma_e N_2^{(sat)} \approx \rho_c \tag{2.43}$$

$$N_2^{(sat)} \approx \frac{N_2^{(unsat)}}{1 + 2P_c/P_{sat}} \tag{2.44}$$

$$P_{sat} \approx \frac{hf_a}{\sigma_e \tau_{fl}} A_{wg} \tag{2.45}$$

where $A_{wg}$ is the cross-sectional area of the ring waveguide. Eq. (2.43) expresses the condition that the gain compensates the losses in the ring, i.e., $\rho_a = 0$, Eq. (2.44) is the relationship between the saturated and unsaturated (i.e., when $P_{in} = 0$) population in

the upper level, and $P_{sat}$ is the saturation power of the gain transition. The absorbed pump power, $P_p$, at wavelength $\lambda_p$ required to maintain an unsaturated upper level population, $N_2^{(unsat)}$, is given by

$$P_p = \frac{hc/\lambda_p}{\tau_{fl}} N_2^{(unsat)} A_{wg} L \tag{2.46}$$

Combining Eqs. (2.41)– (2.46) and invoking the fact that $P_c \gg P_{sat}$ when the gain is highly saturated yields the following final result for the required absorbed pump power.

$$P_p \approx 4 \frac{\lambda_a}{\lambda_p} \frac{F_a}{F_c} P_{in} \tag{2.47}$$

We can see that, from Eq. (2.47), the required absorbed pump power is proportional to the improvement in the resonator finesse, i.e., the square of the reduction factor in the rms angular rotation measurement error as given by Eq. (2.41) when gain is introduced into the ring cavity.

## 2.4 Silver ion exchanged waveguides

### 2.4.1 Introduction of silver ion exchange

Ion exchange is a mature technology for the fabrication of both passive and active glass integrated optical devices. The first IO waveguide was fabricated by ion exchange in 1972 [32]. Since 1972, a large number of studies and reviews on ion exchange in glass have been published [33–36]. There are several types of ion exchange for optical waveguide fabrication in glass substrate [33]. In the discussion to follow, we will only consider ion exchange from a liquid melt in the absence of an externally applied electric field. Under such conditions, sodium cations ($Na^+$) in the glass are generally exchanged with either silver cations ($Ag^+$) or potassium cations ($K^+$) from the melt. Silver ion exchange is advantageous over potassium ion exchange in sev-

eral aspects: lower processing temperature, shorter exchange times, larger refractive index changes, and the absence of stress-induced birefringence [33]. Proper selection of glass substrate, however, is required to fabricate very low propagation loss waveguides using silver ion exchange. The silver ion exchange process occurs in a mixture of molten salt bath of silver nitrate ($AgNO_3$) and sodium nitrate ($NaNO_3$), where $Ag^+$ ions are introduced into the glass at an elevated temperature to replace the $Na^+$ ions in the glass. This process modifies the local concentrations of $Ag^+$ and $Na^+$ inside the glass, thus inducing a local refractive index change. The resulting ion-exchanged waveguide profiles for planar or channel waveguides are directly related to the ion exchange conditions, i.e., melt concentration, diffusion temperature, time and the size of the mask opening used to delineate the channel waveguide.

### 2.4.2 Properties of glass substrate

The glass substrate used to fabricate our active ring resonator is IOG10 glass doped with 2 weight percent $Nd_2O_3$ (Nd-doped IOG10). The glass was produced in a small melt and hence its optical quality was limited. IOG10 is a commercially available silicate glass developed by Schott Glass for silver ion exchange. The glass composition of IOG10 is shown in Table 2.1. The measured absorption spectrum of

| Oxide | IOG10 (weight %) |
|---|---|
| $SiO_2$ | 63.6 |
| $Na_2O$ | 9.2 |
| $K_2O$ | 6.8 |
| $Al_2O_3$ | 3.0 |
| MgO | 2.8 |
| ZnO | 12.5 |
| $Ba_2O_3$ | 1.0 |
| $TiO_2$ | 0.6 |
| $Traces_2$ | 0.5 |

Table 2.1: Glass composition of IOG10.

the Nd-doped IOG10 is shown in Figure 2.4. There are several strong absorption

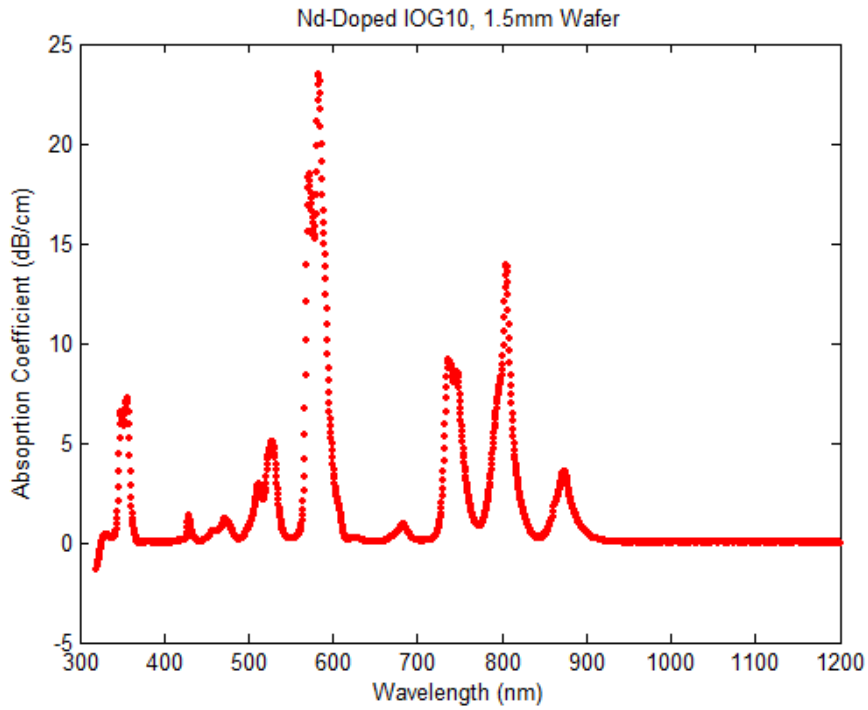


Figure 2.4: Absorption spectrum of neodymium-doped IOG10 glass.

peaks at 580 nm, 740 nm and 808 nm. For our device, optical pumping is achieved using a laser diode operating at a wavelength of $\lambda_p \approx 830$ nm. For the ${}^4F_{3/2} \rightarrow {}^4I_{11/2}$ neodymium transition, the peak fluorescence occurs around $\lambda = 1064$ nm.

### 2.4.3 Characterization of silver ion exchanged waveguides

The single mode condition for the channel waveguide fabricated by silver ion exchange was estimated by the previous modeling work of silver ion exchange [37]. E-beam evaporation was used to deposit a 150 nm thick layer of titanium onto the glass substrate, and then a conventional photolithographic process was utilized to pattern the titanium layer for straight waveguides with different mask openings. For the silver ion exchange parameters, different melt concentrations, diffusion times, and post-annealing cycles are investigated to search for the best recipe to obtain low propagation loss and single mode operation at $\lambda = 1064$ nm. During silver ion exchange, metallic silver clustering can occur at the edges of the titanium mask

openings resulting in large propagation losses. In order to mitigate this effect, the titanium mask was oxidized by placing the wafer in a pure $NaNO_3$ melt at $330^oC$ for one hour. After this step, the ion exchange was performed in a mixed melt of silver nitrate and sodium nitrate (0.35 mol%:99.65 mol%) at $320^oC$ for 15 minutes. Following the exchange, the titanium mask was removed, the waveguide edges were polished and the sample was cleaned. The device was subjected to four cycles of thermal annealing, each of 5 minute duration at a temperature of $320^oC$. The profile of the induced refractive index change (increase) $\Delta n$ for the channel waveguide after four cycles of thermal annealing is obtained using a commercial RNF profilometer (Rinck Elektronik, Germany) operating at $\lambda = 658$ nm and is shown in Figure 2.5. Though not strictly true, for our modeling efforts, the refractive index change ($\Delta n$) is assumed to be independent of wavelength. The fundamental mode profile at $\lambda = 1064$ nm for the channel waveguide given in Figure 2.5 is calculated by beam propagation and is shown in Figure 2.6. The calculated mode profile is used later to design the signal and pump beam waveguide couplers for the active ring resonator described in next section.

## 2.5 Device design and experimental results

A prototype active ring resonator was designed and fabricated in an ion exchangeable silicate glass doped with 2 weight percent $Nd_2O_3$. The ring resonator consists of a pair of straight waveguide arms, a pair of directional couplers and a racetrack ring as shown in Figure 2.7. The racetrack consists of two half circles of radii 8 mm joined together by two 2.915 mm long straight sections. For the directional couplers, the fraction of power coupled from the signal arm into the ring at the signal and pump wavelengths is given by $K_s(\lambda_s)$ and $K_s(\lambda_p)$, respectively, while $K_p(\lambda_s)$ and $K_p(\lambda_p)$ denotes the corresponding coupling coefficients for the pump arm. In order to achieve a high finesse at moderate launched pump powers, the couplers should have small

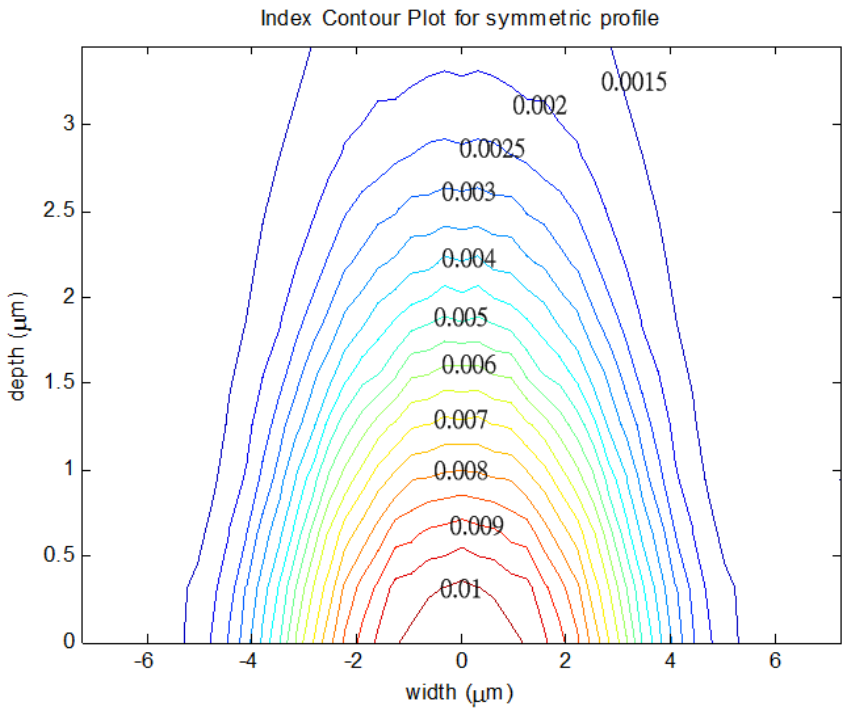


Figure 2.5: 2D profile of refractive index change $\Delta n$ (at $\lambda = 658$ nm) of fabricated silver ion exchanged channel waveguide.

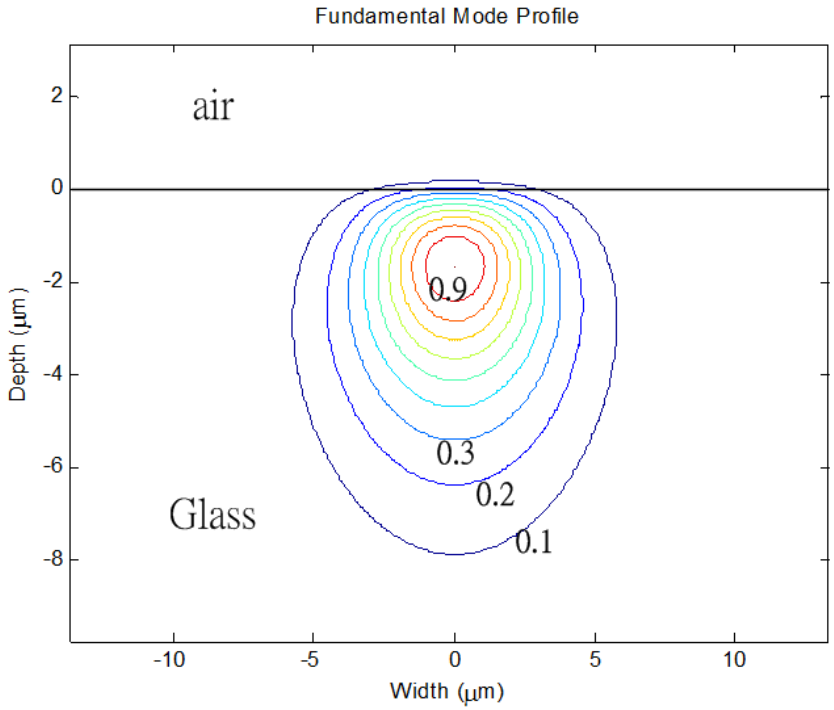


Figure 2.6: Fundamental mode profile at $\lambda = 1064$ nm for fabricated silver ion exchanged channel waveguide.

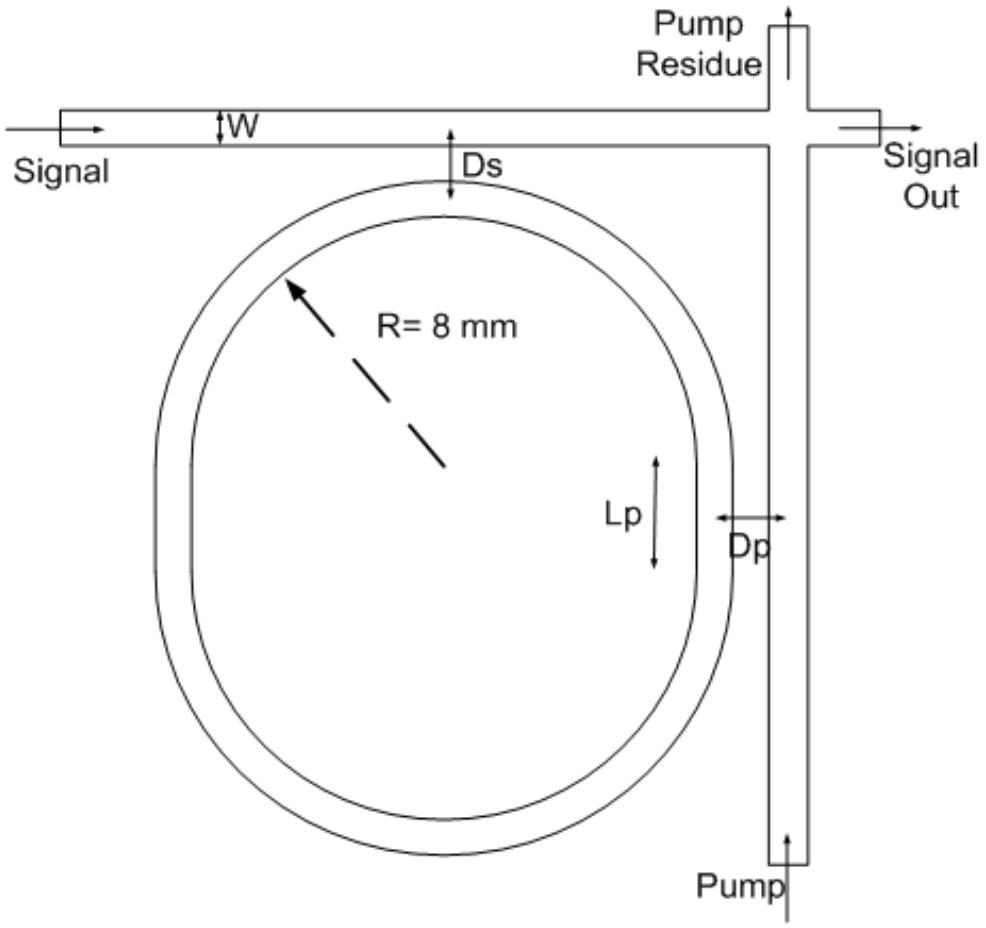


Figure 2.7: Mask layout for single-arm racetrack active ring resonator with pump coupler $W = 1.3$ $\mu$m, $D_s = 8.4$ $\mu$m, $L_p = 2.915$ mm, $D_p = 7.55$ $\mu$m.

values for $K_s(\lambda_s)$, $K_p(\lambda_s)$ and $K_s(\lambda_p)$, while $K_p(\lambda_p)$ should be kept as close to one as possible. Given that the gain medium was chosen to be neodymium-doped glass, $\lambda_s \approx 1060$ nm and a pumping of $\lambda_p \approx 830$ nm was chosen.

Device fabrication is carried out by the silver ion exchange process described in Section 2.4.3 with the device layout shown in Figure 2.7. The un-pumped spectral response of the device was measured after each annealing step using a tunable, external cavity, diode laser manufactured by New Focus operating with a linewidth below 300 KHz. From these measurements, finesse and dip values were found. The pump coupler efficiencies, $K_p(\lambda_p)$ and $K_p(\lambda_s)$, were also measured using separate sets of test couplers that were fabricated together with the resonator on the same chip. The finesse and dip values, along with knowledge of $K_p(\lambda_s)$, allowed us to compute the values of $\rho$ and $K_s(\lambda_s)$. During the thermal annealing steps, diffusion causes the previously indiffused $Ag^+$ ion concentration profile to increases in width and depth, decrease in peak magnitude and assume a smoother shape. These changes reduce the propagation losses due to scattering, but increase the bending loss due to a reduction in $\Delta n$. The overall propagation loss is minimized for some optimal amount of thermal annealing [16]. The coupling efficiencies of the directional coupler will also change as the device is annealed, and these efficiencies are very sensitive to changes in the refractive index profile, thus making accurate design work difficult. Based on our previous experience fabricating passive ring resonators in un-doped version of a similar glass and the corresponding measured refractive index profiles of these devices, the mask parameters specified in Figure 2.7 were chosen [16]. Coupled mode calculations indicated that these parameters should yield small values for $K_s(\lambda_s)$, $K_p(\lambda_s)$ and $K_s(\lambda_p)$ and a relatively large value for $K_p(\lambda_p)$. Several devices with different pump coupler interaction lengths, $L_p$, were fabricated, thus allowing us to select the device that achieved the most favorable values for $K_p(\lambda_p)$ and $K_p(\lambda_s)$, while simultaneously obtaining low values for $K_s(\lambda_s)$ and $K_s(\lambda_p)$. In the absence of pumping, the measured

finesse and dip of the final device were found to be 10.8 and 6.2%, respectively. From these measured values, the propagation loss, $\rho$, and the coupling efficiency, $K_s(\lambda_s)$, for the signal were deduced to be 0.45 dB/cm and 0.94%, respectively. $K_p(\lambda_p)$ and $K_p(\lambda_s)$ were measured to be 52.3% and 3.5%, respectively, using separate sets of test couplers as described above. The high propagation loss for the device reported here is likely due to the small volume of the glass melt used to produce the Nd-doped substrates. Smaller volume melts often result in glasses of lower optical quality. Using similar ion exchange processing, propagation losses on the order of 0.1 dB/cm have been obtained in the un-doped, commercially available version of a similar glass [16]. Losses on the order of 0.01 dB/cm have been achieved for slightly larger sized rings using CVD-deposited silica on silicon films and patterning using RIE [17]. The use of RIE patterning together with such a material system would also simplify the coupler design process and enhance the ability to repeatedly fabricate nearly identical devices.

The output of a 150 mW, single spatial mode, TE-polarized, laser diode operating in the vicinity of 830 nm was coupled into the pump arm of the device described above as shown in Figure 2.7. The spectral response of the resonator was measured using the New Focus tunable source, and the results are shown in Figure 2.8. A long-pass filter, having a cut-off near 900 nm, and a narrow bandpass filter centered at the signal wavelength were placed between the output of the signal arm and the detector in order to remove the residual pump signal and spontaneous emission noise, respectively. The measured, off-resonance, signal power level at the detector during this measurement was 1.7 $\mu W$. The spectral response shown in Figure 2.8 corresponds to a free-spectral range (FSR) of 3.8 GHz, a full-width-half-maximum resonance bandwidth of 15 MHz, a finesse of 250 and a dip of 89%. Using these finesse and dip values, $K_s(\lambda_s)$ and the effective propagation loss inside the ring (including signal loss at the pump coupler) was computed to be 0.84% and 0.013 dB/cm, respectively.

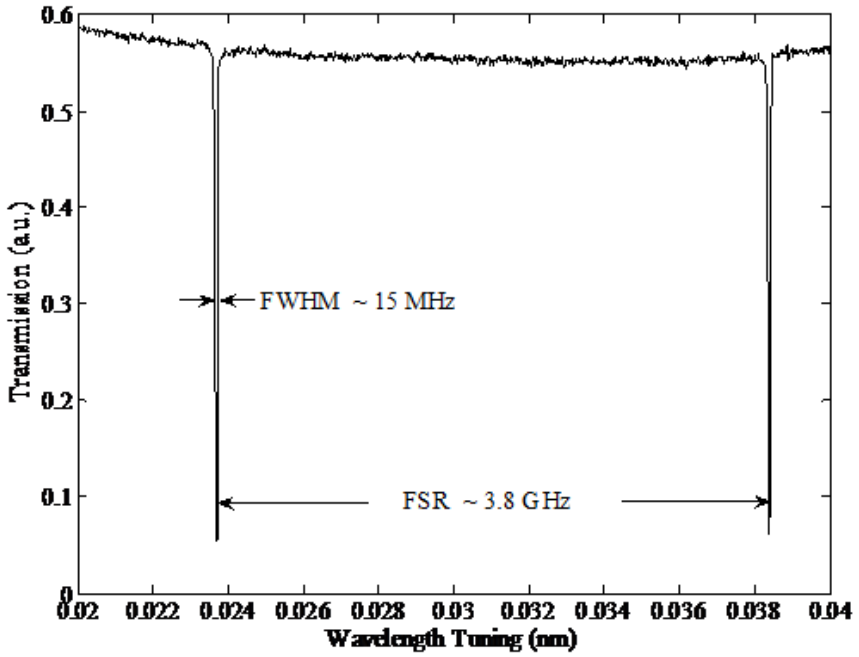


Figure 2.8: Spectral response of active ring resonator.

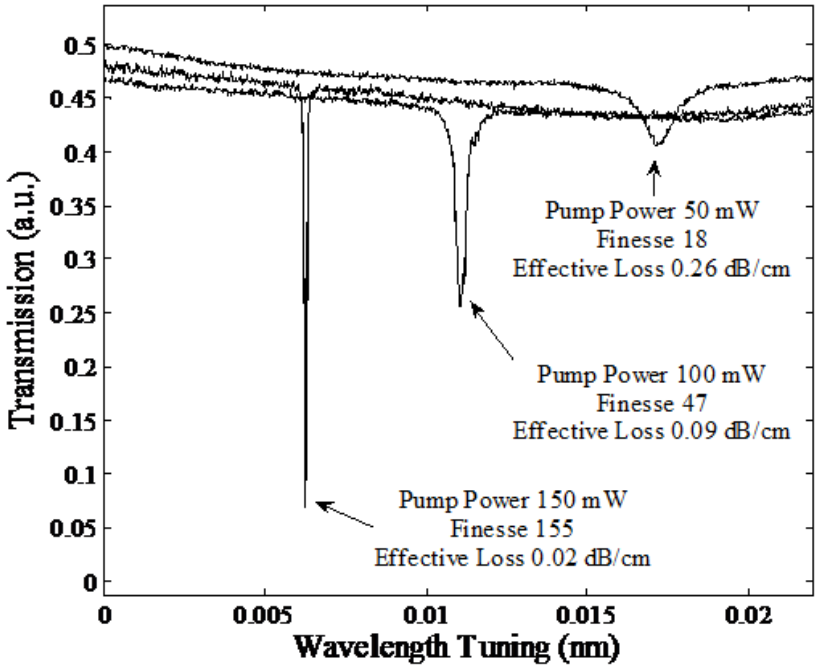


Figure 2.9: Spectral response of active ring resonator as a function of pump power at fixed signal power.

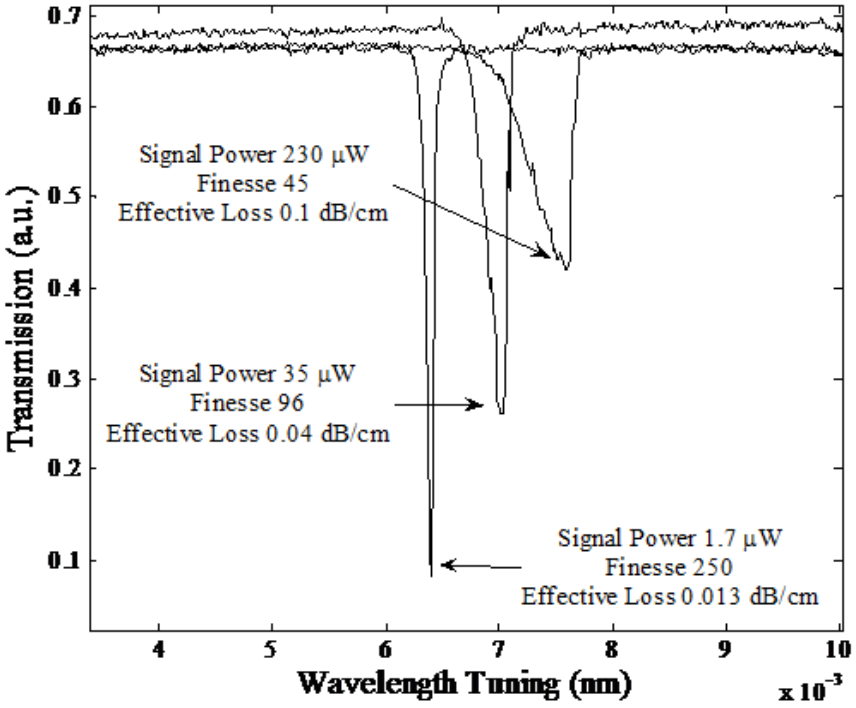


Figure 2.10: Spectral response of active ring resonator as a function of signal power at fixed pump power.

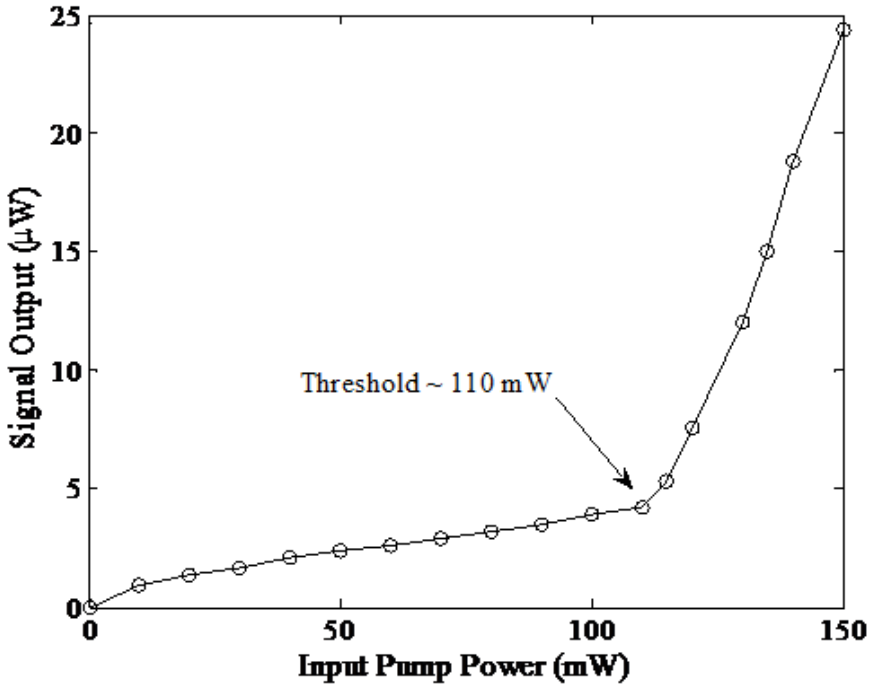


Figure 2.11: Lasing characteristic.

Spectral measurements were repeated at a variety of laser diode pump powers and the results are shown in Figure 2.9. As expected, the effective loss decreases and the finesse increases as the pump power is increased. At a fixed pump power, a decrease in finesse due to gain saturation was also observed as more signal power was coupled into the ring. These gain saturation results are shown in Figure 2.10 as a function of the output signal power measured off-resonance at the detector. Without any launched input signal, the pump power at the device input was increased. A plot of the output signal power, measured at the pump output port, versus input pump power is shown in Figure 2.11. The output signal power vs input pump power curve shows an abrupt slope change at 110 mW indicating the onset of lasing. The high pump power required to achieve lasing can be attributed to high losses in the passive ring resonator together with poor coupling from the diode pump laser into the straight-arm of the pump waveguide. Thus it was difficult to achieve lasing with our pump diodes and unwanted laser action was not observed. In general, however, the launched pump and/or signal powers may need to be carefully controlled in order to inhibit lasing.

The spectral analysis performed in Section 2.3 assumed a purely homogeneously-broadened transition and thus a population inversion that saturates uniformly across the gain transition. If the transition is inhomogenously-broadened, then to first order only the spontaneous emission originating from the homogeneously-broadened spectral packet lying closest to the launched signal's frequency will limit the frequency resolution. Consequently, the basic results Eqs. (2.36) and (2.38) will remain unchanged. When operated as a resonant optical gyro, lasing must be prevented. Because of spectral hole burning, however, the signal inside the resonator may only inhibit lasing at the cavity modes in the vicinity of the signal frequency. In order to inhibit the more distant spectral modes from lasing, it may be necessary to incorporate a course spectral filter into the cavity.

## 2.6 Discussion

Different platforms will have different performance requirements for navigation and/or guidance. The performance of angular rotation rate sensors are usually specified in terms of several parameters, including angle random walk (ARW), bias drift, scale factor linearity, maximum rotation rate and bandwidth. ARW specifies the rms variation of the measured angular rotation rate due to noise. Noise-induced errors can be reduced by increasing the integration time associated with the measurement, but the maximum angular acceleration of the platform will determine the maximum allowable integration time. If the integration time is larger than this maximum value, then the rate sensor will not be able to follow rapid changes of the rotation rate. For this reason, the ARW is typically specified in a normalized form that does not depend on the integration time. According to Eq. (2.18), the ARW of an active ring resonator gyro can be expressed in units of $deg/\sqrt{hr}$ as

$$ARW = \frac{\delta\Omega_{rms}}{\sqrt{BW}} \approx \left(\frac{\lambda_m c}{4AN_{eff}}\right)\left[\frac{1}{\sqrt{F_c F_a}\sqrt{\frac{P_{in}}{hf_m}}}\right] \text{deg}/\sqrt{hr} \tag{2.48}$$

where

$$BW = \frac{1}{\tau_{int}} \tag{2.49}$$

is the measurement bandwidth.

The bias error and scale factor linearity do not depend on noise, and hence these quantities are not fundamentally limited by nature. Any nonreciprocity in the device will induce a relative phase shift between the counter-propagatin beams that gives rise to an apparent rotation even when the platform is stationary. Such affects will lead to a bias error, i.e., a fixed offset between the true and the measured rotation rate even when the integration time is very large.

Imperfections in the device or its electronics may also lead to an output signal

that is not exactly proportional to the rotation rate. These deviations from linearity are referred to as scale factor errors.

Since phase can only be measured modulo $2\pi$, rotation rates that introduce phase differences between the counter-propagating beams that are the same modulo $2\pi$ can not be distinguished by an IFOG. Similarly for the RLG and IROG, the location of spectral dips that are equal, modulo the free spectral range of the resonator, can not be distinguished. These factors limit the maximum rotation rate that can be measured using an optical gyro. Furthermore it is easy to see that the maximum rotation rate is inversely proportional to the cavity length for a RLG and an IROG and inversely proportional to the fiber length for an IFOG.

It is common to place gyro performance into one of three broad categories - rate grade, tactical grade and inertial grade - as indicated in Table 2.2.

| | ARW $(deg/\sqrt{hr})$ | Bias Drift $(deg/hr)$ | Scale Factor Error (ppm) |
|---|---|---|---|
| Inertial grade | $<\sim 0.001$ | $<\sim 0.01$ | $<\sim 5$ |
| Tactical grade | $\sim$ 0.5-0.05 | $\sim$ 0.1-10 | $\sim$ 10-1000 |
| Rate grade | $>\sim 0.5$ | $\sim$ 10-1000 | $\sim$ 1000-10000 |

Table 2.2: Performance of different grade gyroscopes.

Honeywell is one of the largest manufactures of gyroscopes, the specifications of their commercially available gyroscopes can be found on the Honeywell website and in several publications [38]. A partial list of some of its products along with their associated specifications are given in Table 2.3.

| | ARW $(deg/\sqrt{hr})$ | Bias Drift $(deg/hr)$ | Scale Factor Error (ppm) |
|---|---|---|---|
| GG1320AN Laser Gyro | 0.0035 | 0.0035 | 5.0 |
| GG1230AN01 Laser Gyro | 0.01-0.04 | 0.01-0.04 | 50 |
| GG5300 MEMS gyro | 0.2 | 70 | 50000 |
| High Performance IFOG | 0.0007 | 0.006 | 30 |

Table 2.3: Specifications of select Honeywell gyroscopes.

The principle advantage of MEMS gyros are their small size and their low cost.

The low cost is due to the fact that MEMS can be mass produced using standard semiconductor processing techniques. MEMS devices, however, are mechanical. Although more than $100 million dollars has been spent for the R&D of MEMS gyros, it is not clear whether these devices can ever deliver more than rate grade performance.

Ring laser gyros were the first optical gyros capable of delivering inertial-grade performance. A massive engineering effort has gone into developing RLG that are cost effective, small in size and which can achieve inertial-grade performance. Like IROG, the primary source of noise for these devices is spontaneous emission noise from the gain medium. The ARW of these devices depends on the output power of the laser and the finesse of the lasing cavity. The mirrors in RLG, which determine the cavity finesse, already extremely low losses and are unlikely to be improved much beyond their current state. Thus the ARW of a RLG can only be improved by increasing the cavity length, and hence the size of the device. Space, however, is often very limited on a platform, and thus increasing the size of the device is often not practical. Current single-axis laser gyros weigh only about 1 lb, occupy volumes under 20 inches$^3$ and cost less than $10,000. Bidirectional lasing, however, is not possible in a solid state laser due to the gain competition between the counter-propagating beams. Thus all RLG have gas as their gain medium (i.e., HeNe). Gas lasers are generally less reliable and have shorter lifetimes than solid state lasers, and thus for some applications there is a desire to move away from RLG.

Of all the gyros, IFOG can offer the best performance in a very small package. Unlike RLG and IROG, the ARW performance of an IFOG is limited by shot noise at the detector and not by spontaneous emission noise of a gain medium. Thus the ARW can be decreased by increasing the length of the fiber coil. As with all gyros, parasitics such as polarization effects, optical nonlinearities, ... etc., can greatly degrade performance. High precision IFOG are extremely difficult to build and thus are very expensive, i.e., hundreds of thousands of dollars. Consequently, not many

high performance IFOG have been deployed.

A limited amount of work, including industrial R&D efforts undertaken by Honeywell and BAE Systems, has gone into developing passive IROG. Three advantages of IROG are their small size, the fact that they are solid state devices (no gases), and they have the potential to be manufactured at low cost using standard semiconductor batch processing techniques. The ARW of an IROG will depend on the finesse of the ring, which in turn depends on the propagation losses in the ring. As opposed to optical fibers, that typically have losses below several tenths of a dB/km, the best planar waveguides have losses of approximately 0.01 dB/cm. A 2-cm diameter ring with such a loss could achieve at best an ARW of $\sim 0.05$ deg/$\sqrt{hr}$, and thus would not be suitable for inertial grade applications. Furthermore an IROG is a rather complicated device, since it requires either a tunable laser source or a tunable path length ring in order to locate the resonant dip. In contrast, the counter-propagating outputs of a RLG merely need to be combined on a detector in order to measure the beat frequency and hence the rotation rate. If the losses of planar waveguides could be reduced by one or two orders of magnitude, then passive IROG might become an attractive option. This later observation was the motivation for investigating active IROG that contain a solid state gain medium inside the ring.

We have determined the minimum ARW achievable by an active, ring resonator gyroscope in the quantum limit in this chapter, and the reduction in the ARW is equal to the square root of the improvement in resonator finesse (i.e., $\sqrt{\frac{F_a}{F_c}}$). To date, losses of approximately 0.01 dB/cm can be achieved by passive waveguide rings fabricated using CVD-deposited silica on silicon together with reactive ion etching of the waveguide structure for ring radii on the order of 1 cm. This loss value corresponds to a cold cavity finesse value of approximately 125 and a dip value of 2% for $K_s(\lambda_s) \approx 0.025\%$. If we improve the finesse value to 12500 by incorporation of gain into the ring cavity, then the ARW error can be estimated to be $\sim 0.005\ deg/\sqrt{hr}$ by using Eq. (2.38) and

assuming that $P_{in} = 1$ mW, $n_r = 1.5$, $\lambda_a = 1.064$ $\mu$m. This ARW performance value is comparable to that of a good laser gyro. Other practical considerations, however, such as high required pump power, $P_p$ (approximately 500 times $P_{in}$ in our example), Kerr nonlinearities due to large circulating cavity power, $P_c$ (approximately $10^4$ times $P_{in}$), and the engineering of small bias drifts and small scale factor errors may make it difficult to achieve the fundamental performance limit estimated here. In principle, as technology advances, active IROG may become promising candidates for inertial- and/or tactical-grade navigation gyroscopes. Extensive engineering efforts will be required to solve the practical issues raised above.

# CHAPTER III

# An Infrared Integrated Optic Astronomical Beam Combiner for Stellar Interferometry

## 3.1 Introduction

The ultimate resolution of a single aperture telescope is limited by diffraction because of the wave nature of light. The angular size of the smallest resolvable image feature is directly proportional to the viewing wavelength and inversely proportional to the diameter of the telescope's aperture. It is well known that high-angular resolution astronomical imaging can be achieved interferometrically by combining the wavefronts from spatially separated single aperture telescopes. The resulting resolution depends not on the diameters of the individual apertures (which are limited by practical considerations) but rather on the separations between the telescopes, which can be made rather large. The Michelson stellar interferometer measures the complex amplitude correlation between two optical fields measured at spatially separated apertures. According to the van Cittert-Zernike theorem [39], this correlation is proportional to the Fourier transform of the object's intensity distribution at a spatial frequency equal to the projected separation of the apertures divided by the observing wavelength [40]. By changing the baseline of the apertures, the Fourier transform of the object's intensity distribution may be obtained at a large number of spatial

frequencies, thus allowing an image of the object to be reconstructed. In 1891 on the twelve-inch aperture of a telescope at the Lick observatory, Michelson used stellar interferometry to measure the diameter of the four moons of Jupiter [41]. Recently, stellar interferometry has been applied to other areas of astrophysics such as high resolution imaging of binary stars, direct imaging of rapid rotating stars, the observation and modeling of circumstellar dust shells and the search for exoplanets [42].

There is a longstanding quest to find planets orbiting other stars (i.e., exoplanets), especially Earth-like planets in habitable zones where the surface temperature is able to support liquid water over a range of surface pressures. Since 1995, more than 350 planets beyond our solar system have been discovered indirectly by Doppler spectroscopy, astrometry, transit methods, and microlensing effects [43]. Most of the exoplanets discovered so far are giants similar to Jupiter and Saturn, which are unfavorable for supporting life. Inteferometric imaging offers a direct method for observing exoplanets. The main difficulty in imaging an exoplanet is separating the faint light of the planet from the bright emission of its host star. At mid-infrared wavelengths (7 $\mu$m – 20 $\mu$m) a planet is over $10^6$ times fainter than its host star, with this ratio increasing to $10^{10}$ in the visible band. High resolution interferometric imaging requires that more than two apertures be combined.

One of the major advantages of integrated optic (IO) beam combiners, as opposed to purely optical fiber implementations, is the ability to combine multiple apertures on a single chip in a scalable manner. IO interferometers offer additional advantages over bulk implementations, including spatial filtering, enhanced stability, electrically-controlled, on-chip, phase modulation, and wavelength conversion [44]. IO beam combiners for astronomical imaging were first proposed by Kern et al. in 1996 [2]. Using silicate-based glass IO devices, laboratory and on-sky measurements of stellar interferograms were demonstrated by Berger et al. at astronomical H (1.5 $\mu$m – 1.8 $\mu$m) and K (2.0 $\mu$m – 2.4 $\mu$m) bands [45–49]. Star-to-planet brightness ratios make

operation in the infrared beyond 3 $\mu$m attractive, but classical silicate-based glasses are not transparent in this spectral band. On-sky interferometric measurements have been performed in the L band using a two-beam fluoride glass fiber coupler, but this fiber-based technology is not easily scalable to multiple apertures [50].

Some preliminary measurement results for an integrated optic beam combiner, made by annealed proton-exchanged (APE) waveguides in lithium niobate ($LiNbO_3$), have been previously reported [51]. Electro-optic (EO) modulation in Ti-diffused $LiNbO_3$ at 3.39 $\mu$m has also been demonstrated [52]. In this chapter, we describe the development of a prototype, single-mode, IO, astronomical beam combiner fabricated by titanium-indiffusion in x-cut $LiNbO_3$. The device operates in 3.2 $\mu$m – 3.8 $\mu$m region, which lies in the L band, and has on-chip, EO-controllable fringe scanning. Using a broadband thermal source in the laboratory, a white-light interferogram, along with on-chip EO fringe scanning, is demonstrated with an IO beam combiner operating in the L band for the first time. In the following section, a brief history, as well as the basic theory, of interferometric imaging is presented. In Section 3.3, the fabrication and the characterization of titanium-indiffused waveguides in $LiNbO_3$ are described. In Section 3.4 the design and characterization of the IO beam combiner is presented. In Section 3.5 laboratory measurements of a white-light interferogram produced by the IO beam combiner operating in the L band are described. In Section 3.6, our results are discussed.

## 3.2 Background

### 3.2.1 History of astronomical interferometers

An astronomical interferometer consists of an array of spatially separated telescopes and/or mirrors and the apparatus to combine the light collected from these elements. Astronomical interferometers are widely used in astronomy at optical,

infrared, submillimeter, and radio wavelengths. A Fourier-based technique, called aperture synthesis, can be used to perform high resolution imaging using astronomical interferometers. At optical wavelengths, astronomical interferometers have been used to form images with resolution higher than what can be obtained by conventional single aperture telescopes. Fizeau first introduced the idea of stellar interferometry in 1868. In 1874 Stéphan put the idea into practice by deducing the upper limit of the diameter of an observed star. Michelson independently re-invented the concept of stellar interferometry nearly two decades later. At the Lick observatory in 1891, he measured the diameter of four moons of Jupiter using an interferometer. Between 1920 and 1921, the red giant star Betelgeuse was the first star to have its diameter determined using stellar interferometry. The field of optical stellar interferometry remained fallow for nearly the next three decades. During this period, interest shifted to the field of radio astronomy where interferometric imaging techniques based on aperture synthesis (i.e., use of van Cittert-Zernike theorem) were developed. M. Ryle received the Nobel Prize for these developments in 1974. After three decades of domination at radio frequencies, interferometry was extended to measurements using separated telescopes at infrared wavelengths by Johnson et al. in 1974 [53] and by Labeyrie in 1975 [54] at the visible wavelengths. In late 1970's, the first fringe tracking interferometer was constructed, and its operation was made possible by the advances in computer processing power. These advancements resulted in the MK I, II, and III series of interferometers, which are capable of achieving high resolution even in the presence of atmospheric turbulence. Other astronomical telescope arrays, such as the Keck Interferometer and the Palomar Testbed Interferometer, were based on similar techniques. In the 1980s the aperture synthesis interferometric imaging technique, first used by radio astronomers, was extended to visible light and infrared astronomy by the Cavendish Astrophysics Group. The first very high resolution images of nearby stars were obtained using aperture masking interferometry on the William

Herschel Telescope. In 1995 this technique was demonstrated on an array of separate optical telescopes for the first time. Further improvements in resolution and even high resolution imaging of stellar surfaces have been achieved. In 1996, the closure phase method was combined with measured visibility amplitudes for the first time by the COAST interferometer. These methods have now been applied to several other astronomical telescope arrays, including the Navy Prototype Optical Interferometer, the Infrared Spatial Interferometer and the IOTA array.

Recently, the use of interferometers to search for extrasolar planets has been a topic of interest. Space-based interferometry is a promising method to search and to characterize earth-like planets at high contrast and high angular resolution. NASA's Terrestial Planet Finder (TPF) program [55] and ESA's Darwin mission [56] are ambitious efforts to realize this goal. The TPF program spans several different mission concepts, including internal coronagraphs (TPF-C), external occulters (TPF-O) and nulling interferometers (TPF-I) [57]. The last of these, the nulling interferometer, was proposed by Bracewell in 1978 [58]. A nulling interferometer is able to cancel the light coming directly from a bright star, thus making it possible to see relatively faint orbiting planets [58]. The TPF-I mission's goal is to build and deploy a mid-infrared, space-based, nulling interferometer based on Bracewell's basic idea. The space-based interferometer will be designed to find and measure the mid-infrared spectra of the atmospheres of Earth-like exoplanets around nearby stars. The TPF-I mission will search for evidence of key biomarkers, such as ozone, water, and carbon dioxide so that the possible presence of planetary life can be inferred [59, 60].

### 3.2.2 Principles of optical long baseline stellar interferometry

The resolution of a ground-based telescope is limited by the wave nature of light and the turbulence in the Earth's atmosphere. In the absence of atmospheric turbulence, the angular resolution $\vartheta$ of a perfect telescope is limited by the diffraction

pattern of a point source (Airy pattern) and is given by

$$\vartheta = 1.22\frac{\lambda}{D} \tag{3.1}$$

where $\lambda$ is the wavelength of light and $D$ is the diameter of the telescope. Each point on the source produces an Airy pattern and these patterns overlap, thus degrading the fine detail of the structure. Therefore, shorter wavelengths and/or larger telescope apertures are required for high resolution astronomical imaging. Alternately high resolution can be achieved by using optical long baseline stellar interferometry. The principle of operation of an optical long baseline stellar interferometer can be illustrated by considering Figure 3.1. The stellar interferometer shown in this figure consists of two widely separated small diameter telescopes, a delay line unit, and a beam combining unit. We consider a two-dimensional, monochromatic, spatially incoherent source that lies in the $\eta$-$\xi$ plane. The source is viewed by two small apertures in the $X$-$Y$ plane a large distance, $L$, away as shown in Figure 3.2. The apertures in the $X$-$Y$ plane are located at points $\mathbf{P}_1 = (x_1, y_1)$ and $\mathbf{P}_2 = (x_2, y_2)$, and the corresponding complex-value field amplitudes at these points are denoted as $A(\mathbf{P}_1)$ and $A(\mathbf{P}_2)$, respectively. The spatial distribution of the source intensity is given by $I(\eta, \xi)$. Since each point on the source can be considered to radiate as a spherical wave, the field amplitude at a point $(x_i, y_i)$ in the $X$-$Y$ plane produced by the source at point $(\eta, \xi)$ in the $\eta$-$\xi$ plane is given by

$$\frac{\sqrt{I(\eta, \xi)}\exp(jk_0R_i)}{R_i} \tag{3.2}$$

where $k_0 = \frac{2\pi}{\lambda}$, $\lambda$ is the source wavelength, and

$$R_i = \sqrt{(\eta - x_i)^2 + (\xi - y_i)^2 + L^2}. \tag{3.3}$$

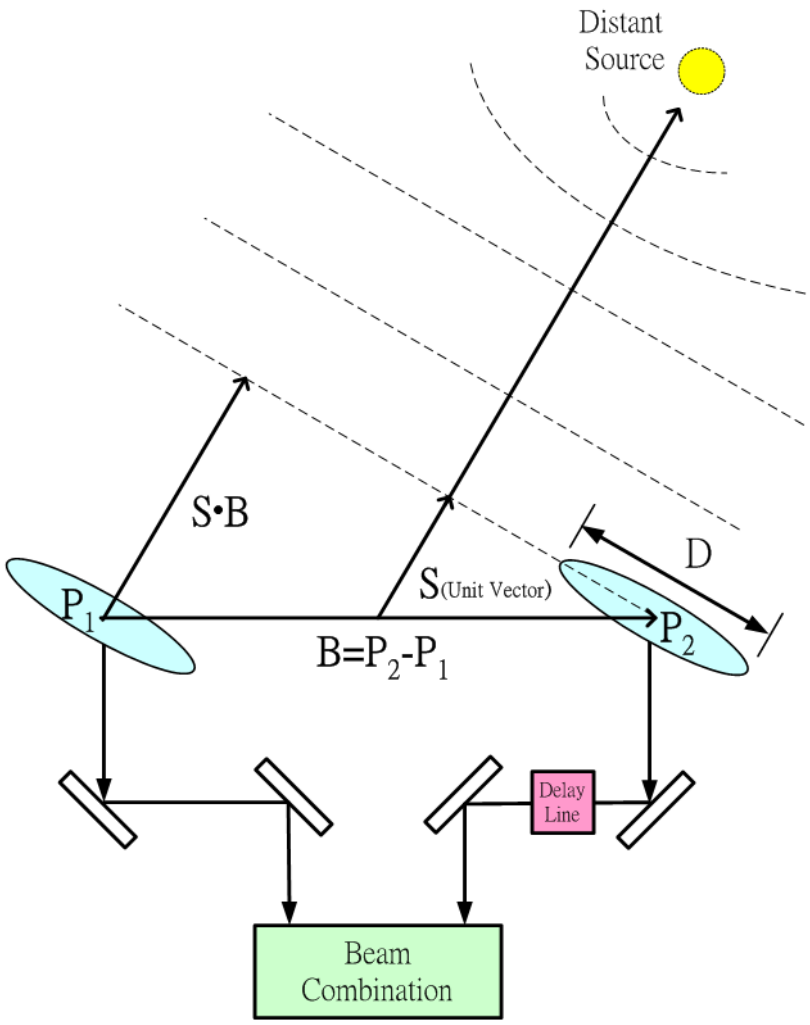


Figure 3.1: Illustration of the principle of operation of an optical long baseline stellar interferometer.

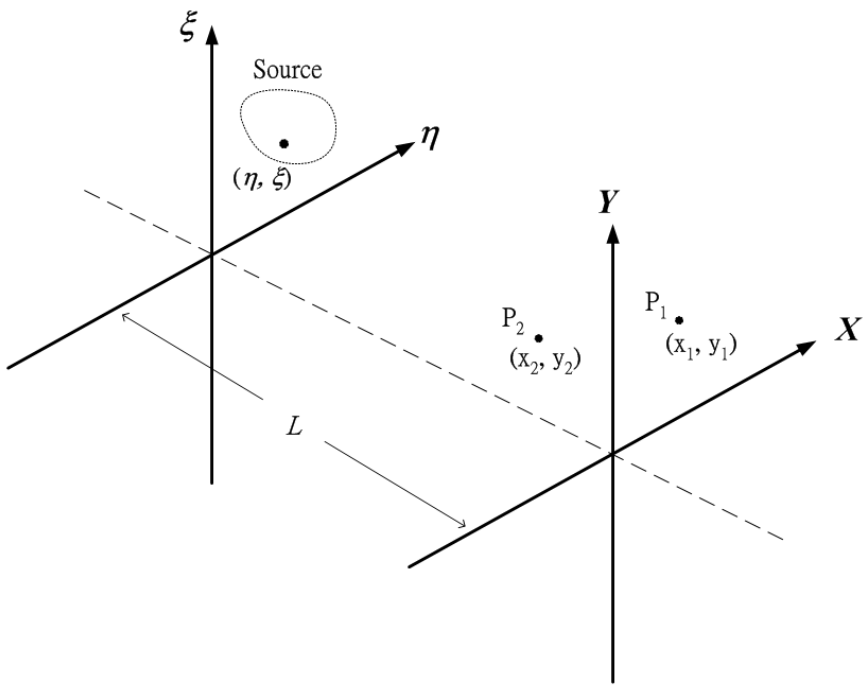


Figure 3.2: Geometry of the two-dimensional, monochromatic, spatially incoherent source distribution and the observing apertures, $\mathbf{P}_1$ and $\mathbf{P}_2$.

The complex visibility function, $V(\mathbf{P}_1, \mathbf{P}_2)$, is defined as

$$V(\mathbf{P}_1, \mathbf{P}_2) =< A(\mathbf{P}_1)A^*(\mathbf{P}_2) >= \int_{-\infty}^{+\infty}\int_{-\infty}^{+\infty} I(\eta, \xi)\frac{\exp[jk_0(R_1 - R_2)]}{R_1 R_2}\, d\eta\, d\xi \qquad (3.4)$$

where $< >$ denotes a time average. When $L$ is quite large compared to the physical size of the object and the region of observation in the $X$-$Y$ plane, then $R_i$ can be approximated by

$$R_i \approx L + \frac{(\eta - x_i)^2 + (\xi - y_i)^2}{2L}. \qquad (3.5)$$

Combining Eqs. (3.4) and (3.5) yields

$$V(\mathbf{P}_1, \mathbf{P}_2) = < A(\mathbf{P}_1)A^*(\mathbf{P}_2) > \\ = \frac{\exp[j\Psi(\mathbf{P}_1, \mathbf{P}_2)]}{L^2} \int_{-\infty}^{+\infty}\int_{-\infty}^{+\infty} I(\eta, \xi) \exp[-j(\eta u + \xi v)]\, d\eta\, d\xi \tag{3.6}$$

where

$$\Psi(\mathbf{P}_1, \mathbf{P}_2) = k_0 \frac{(x_1^2 + y_1^2) - (x_2^2 + y_2^2)}{2L} \approx 0 \tag{3.7}$$

$$u = k_0 \frac{x_2 - x_1}{L} \tag{3.8}$$

$$v = k_0 \frac{y_2 - y_1}{L} \tag{3.9}$$

Note according to Eq. (3.7), we can neglect the term $\exp[j\Psi(\mathbf{P}_1, \mathbf{P}_2)]$ appearing in Eq. (3.6). Thus for a monochromatic, spatially incoherent source, Eq. (3.6) indicates that the complex visibility function is proportional to the Fourier transform of the spatial intensity distribution of the source object. This result is known as the van Cittert-Zernike theorem [39].

The system shown in Figure 3.1 can be used to measure the complex visibility function $V(\mathbf{P}_1, \mathbf{P}_2)$. The fields at the two apertures are combined (i.e., added) with a relative phase delay of $\phi$ introduced (by the delay line shown in Figure 3.1) between the two fields. [1] The time-averaged intensity $I_{x-y}(\mathbf{P}_1, \mathbf{P}_2)$ of the combined fields is given by

$$I_{x-y}(\mathbf{P}_1, \mathbf{P}_2) = < |A(\mathbf{P}_1) + \exp(-j\phi)A(\mathbf{P}_2)|^2 > \\ = < |A(\mathbf{P}_1)|^2 > + < |A(\mathbf{P}_2)|^2 > + 2\mathrm{Re}[< A(\mathbf{P}_1)A^*(\mathbf{P}_2) > \exp(j\phi)] \tag{3.10}$$

[1] Note that if the interferometer is to be operated over a broad wavelength band, then the introduced phase delay, $\phi$, must be wavelength independent. In addition, the beam combining operation described by Eq. (3.10) must be achromatic.

Combining Eqs. (3.6) and (3.10) yields

$$\begin{aligned} I_{x-y}(\mathbf{P}_1,\mathbf{P}_2) =& < |A(\mathbf{P}_1) + \exp(-j\phi)A(\mathbf{P}_2)|^2 > \\ =& \frac{2}{L^2}\int_{-\infty}^{+\infty}\int_{-\infty}^{+\infty} I(\eta,\xi)\,d\eta\,d\xi \\ &+ \frac{2}{L^2}\int_{-\infty}^{+\infty}\int_{-\infty}^{+\infty} I(\eta,\xi)\cos[(\eta u+\xi v)-\Psi(\mathbf{P}_1,\mathbf{P}_2)-\phi]\,d\eta\,d\xi \\ =& c_0 + c_1(\mathbf{P}_1,\mathbf{P}_2)\cos(\phi) + c_2(\mathbf{P}_1,\mathbf{P}_2)\sin(\phi) \end{aligned} \tag{3.11}$$

where

$$c_0 = \frac{2}{L^2}\int_{-\infty}^{+\infty}\int_{-\infty}^{+\infty} I(\eta,\xi)\,d\eta\,d\xi \tag{3.12}$$

$$c_1(\mathbf{P}_1,\mathbf{P}_2) = \frac{2}{L^2}\int_{-\infty}^{+\infty}\int_{-\infty}^{+\infty} I(\eta,\xi)\cos[(\eta u+\xi v)-\Psi(\mathbf{P}_1,\mathbf{P}_2)]\,d\eta\,d\xi \tag{3.13}$$

$$c_2(\mathbf{P}_1,\mathbf{P}_2) = \frac{2}{L^2}\int_{-\infty}^{+\infty}\int_{-\infty}^{+\infty} I(\eta,\xi)\sin[(\eta u+\xi v)-\Psi(\mathbf{P}_1,\mathbf{P}_2)]\,d\eta\,d\xi \tag{3.14}$$

By introducing the quantities $r$ and $\theta$ defined by

$$r(\mathbf{P}_1,\mathbf{P}_2) = \sqrt{c_1^2(\mathbf{P}_1,\mathbf{P}_2) + c_2^2(\mathbf{P}_1,\mathbf{P}_2)} \tag{3.15}$$

$$\theta(\mathbf{P}_1,\mathbf{P}_2) = \tan^{-1}\frac{c_2(\mathbf{P}_1,\mathbf{P}_2)}{c_1(\mathbf{P}_1,\mathbf{P}_2)}, \tag{3.16}$$

Eq. (3.11) becomes

$$I_{x-y}(\mathbf{P}_1,\mathbf{P}_2) = c_0 + r\cos(\phi-\theta). \tag{3.17}$$

Thus $I_{x-y}(\mathbf{P}_1,\mathbf{P}_2)$ will vary sinusoidally as the phase delay $\phi$ is varied. It is easily

verified that the fringe visibility is given by

$$\frac{\max_\phi I_{x-y} - \min_\phi I_{x-y}}{\max_\phi I_{x-y} + \min_\phi I_{x-y}} = \frac{r}{c_0} \tag{3.18}$$

and $\theta$ is equal to the value of $\phi$ for which $I_{x-y}$ is maximum. From Eqs. (3.6) and (3.12)-(3.14), we see that

$$\begin{aligned} V(\mathbf{P}_1, \mathbf{P}_2) =& c_1(\mathbf{P}_1, \mathbf{P}_2) - j c_2(\mathbf{P}_1, \mathbf{P}_2) \\ =& r(\mathbf{P}_1, \mathbf{P}_2) \exp[-j\theta(\mathbf{P}_1, \mathbf{P}_2)] \end{aligned} \tag{3.19}$$

Thus the complex visibility function for a given pair of telescope apertures at points $\mathbf{P}_1$ and $\mathbf{P}_2$ can be determined by measuring $r(\mathbf{P}_1, \mathbf{P}_2)$ and $\theta(\mathbf{P}_1, \mathbf{P}_2)$ interferometrically as the phase delay $\phi$ is varied. By changing the location of telescope apertures in the $X$-$Y$ plane and making repeated fringe visibility measurements, data for the complex visibility function is obtained for a wide range of spatial frequencies $u$ and $v$. Using this data, the inverse Fourier transform can be performed to obtain the intensity distribution of the source object using Eq. (3.6). It is convenient to re-write Eq. (3.6) in terms of angular coordinates, $\eta'$ and $\xi'$, and normalized spatial frequencies, $u'$ and $v'$, defined by

$$(\eta', \xi') = (\eta/L, \xi/L) \tag{3.20}$$

$$(u', v') = k_0(x_2 - x_1, y_2 - y_1). \tag{3.21}$$

In terms of these new quantities, Eq. (3.6) can be expressed as

$$V(u', v') \propto \int_{-\infty}^{+\infty} \int_{-\infty}^{+\infty} I(\eta', \xi') \exp[-j(\eta' u' + \xi' v')] \, d\eta' \, d\xi' \tag{3.22}$$

Taking the inverse Fourier transform of Eq. (3.22) yields

$$I(\eta', \xi') \propto \int_{-\infty}^{+\infty} \int_{-\infty}^{+\infty} V(u', v') \exp[j(\eta' u' + \xi' v')] \, du' \, dv' \tag{3.23}$$

In general, the visibility measurements can only be taken over a limited region of the $u'$-$v'$ plane. In fact if the region is limited to

$$\sqrt{(u')^2 + (v')^2} \leq k_0 D_s \tag{3.24}$$

where $D_s$ corresponds to the maximum separation between the apertures in the $X$-$Y$ plane, then it follows from the properties of Fourier transforms and Eq. (3.23) that

$$\underbrace{\int\int V(u', v') \exp[j(\eta' u' + \xi' v')] \, du' \, dv'}_{\sqrt{(u')^2+(v')^2} \leq k_0 D_s} \propto I(\eta', \xi') * \left[ J_1(\sqrt{(\eta')^2 + (\xi')^2} \frac{k_0 D_s}{2}) \right] \tag{3.25}$$

where $J_1(\,)$ is the Bessel function of order 1. Thus the reconstructed angular distribution of the source intensity is the true source intensity distribution convolved with an Airy pattern that has a peak-to-null width of

$$\frac{1.22\lambda}{D_s}. \tag{3.26}$$

Therefore according to Eq. (3.1) and (3.26), a stellar interferometer with a maximum baseline separation of $D_s$ achieves the same angular resolution as a single aperture telescope of diameter $D_s$.

For ground-based telescopes, the phase, $\theta$, of the complex visibility function can not be well-measured because of phase changes induced by atmospheric fluctuations at the two telescope apertures. If three or more observations are made at different tele-

scope apertures simultaneously, the relative phases of the complex visibility function can be obtained by a technique called phase closure, in which the atmospherically-induced phase fluctuations cancel out [61]. Although the phase closure technique applies to any number of apertures greater than three, a large number can always be broken down into independent groups of three ($n = 1, 2, 3$). The complex visibility function is measured simultaneously for each pair in the group. We assume that the amplitude and phase signals from each aperture contain a slowly changing atmospheric phase error of unknown values $\varphi_{i0}$. The apparent complex visibility function, $V^a$, can be calculated and is given by

$$\begin{aligned} V^a(\mathbf{P}_i, \mathbf{P}_j) = &< A(\mathbf{P}_i) \exp(j\varphi_{i0}) A^*(\mathbf{P}_2) \exp(-j\varphi_{j0}) > \\ =&V(\mathbf{P}_i, \mathbf{P}_j) \exp[j(\varphi_{i0} - \varphi_{j0})] \end{aligned} \tag{3.27}$$

since $\varphi_{i0}$ and $\varphi_{j0}$ are independent of time during the measurement period. As a result, the product of the pair-wise complex visibility functions around a closed loop (i.e., (1,2), (2,3), (3,1)) is independent of the atmospheric phases and is given by

$$\begin{aligned} V^a(\mathbf{P}_1, \mathbf{P}_2) V^a(\mathbf{P}_2, \mathbf{P}_3) V^a(\mathbf{P}_3, \mathbf{P}_1) =&V(\mathbf{P}_1, \mathbf{P}_2) V(\mathbf{P}_2, \mathbf{P}_3) V(\mathbf{P}_3, \mathbf{P}_1) \\ =&r_{12} r_{23} r_{31} \exp(-j\theta_c) \end{aligned} \tag{3.28}$$

where $r_{nm} \exp(-j\theta_{nm})$ is the complex visibility function associated with the aperture pair $n$ and $m$ and $\theta_c = \theta_{12} + \theta_{23} + \theta_{31}$ is called the closure phase. If the phase closure value, $\theta_c$, is measured for different positions of the three apertures and some of these pairwise positions are redundant, then the individual pairwise phases $\theta_{nm}$ can be estimated. This technique allows the optical image of the source object to be reconstructed by aperture synthesis even in the presence of atmospheric turbulence.

IO beam combiners are well suited for the aperture synthesis of star images because these IO devices are capable of combining multiple apertures on a single chip in

a scalable manner. In addition to stellar interferometry, IO beam combiners can play a useful role for exoplanet searches that rely on nulling interferometry. The requirements related to the wavelength insensitivity of beam combining are much more stringent for nulling interferometers than they are for stellar interferometers. The design of an IO beam combiner with broadband achromatic beam combining features will be presented in Chapter IV. In the following sections of this chapter, we will focus on the design, fabrication, and the characterization of astronomical IO beam combiners operating in the L band for stellar interferometry.

## 3.3 Fabrication and characterization of titanium-indiffused waveguides in $LiNbO_3$

In order to obtain accurate visibility measurements the waveguides in the beam combiner must be single mode at the operating wavelengths. The beam combiner was fabricated in $LiNbO_3$ because this substrate has excellent transparency from visible wavelengths to approximately 4 $\mu$m, and it may be easily EO phase modulated [52]. There are two widely used methods for fabricating waveguides in $LiNbO_3$: annealed proton-exchanged (APE) and titanium in-diffusion (Ti:$LiNbO_3$). The later method produces low-index contrast waveguides, and thus the radius of curvature of the waveguide bends must be kept large in order to avoid significant bending losses. On the other hand, APE waveguides only support the mode polarized along the z-axis of the substrate, while both TE- and TM-modes can be supported by Ti:$LiNbO_3$ waveguides. Furthermore, APE waveguides show strong, broad OH absorption peaks around 3500 $cm^{-1}$ ( 2.8 $\mu$m), which have the potential to significantly increase the propagation losses in 3 $\mu$m – 4 $\mu$m band [62]. Therefore the Ti-indiffusion method was chosen to fabricate the astronomical beam combiners reported here.

### 3.3.1 Waveguide fabrication

The fabrication of titanium-indiffused waveguides is straightforward. Although there are slight variations, the typical steps to fabricate channel waveguides by lift-off patterning are shown in Figure 3.3. The polished $LiNbO_3$ crystal is cleaned and spun with photoresist. The desired waveguide pattern of the design mask is transferred onto photoresit by tranditional photolithographic process. After developing photoresist, a clear window corresponding to the waveguide pattern is left in the photoresist. Titanium is E-beam deposited over the entire crystal and the crystal is then placed in a photoresist solvent which removes the photoresist along with the unwanted titanium film.

The crystal is then placed in a covered ceramic tray inside a diffusion furnace for diffusion at temperatures ranging from $980^oC$ to $1050^oC$ for duration of few hours to tens of hours. The lower temperature leads to a long diffusion time while the upper limit is set by the Curie temperature ( $1125^oC$ ) of the crystal. The furnace is cooled down to room temperature after diffusion.

### 3.3.2 Waveguide characterization

Both planar and channel waveguides were obtained by diffusing an E-beam deposited, 1600Å-thick Ti layer into congruent x-cut $LiNbO_3$ for 35 hours at $1050^oC$ in a covered ceramic tray [52]. For the channel waveguides, the width, $W$, of the pre-diffused Ti strips was chosen to be 18 $\mu$m. In the y-z plane of the x-cut $LiNbO_3$ wafer, the channel waveguides were oriented parallel to the y-axis. A prism coupling technique was used to measure the effective indices of the TE planar waveguide modes at $\lambda = 0.633$ $\mu$m. In this method, a laser beam strikes the base of a high-index prism and is normally totally reflected at the prism base onto a photodetector. At certain discrete values of the incident angle, $\Theta$, photons can tunnel across the air gap between the prism base and the fabricated planar waveguide and excite the

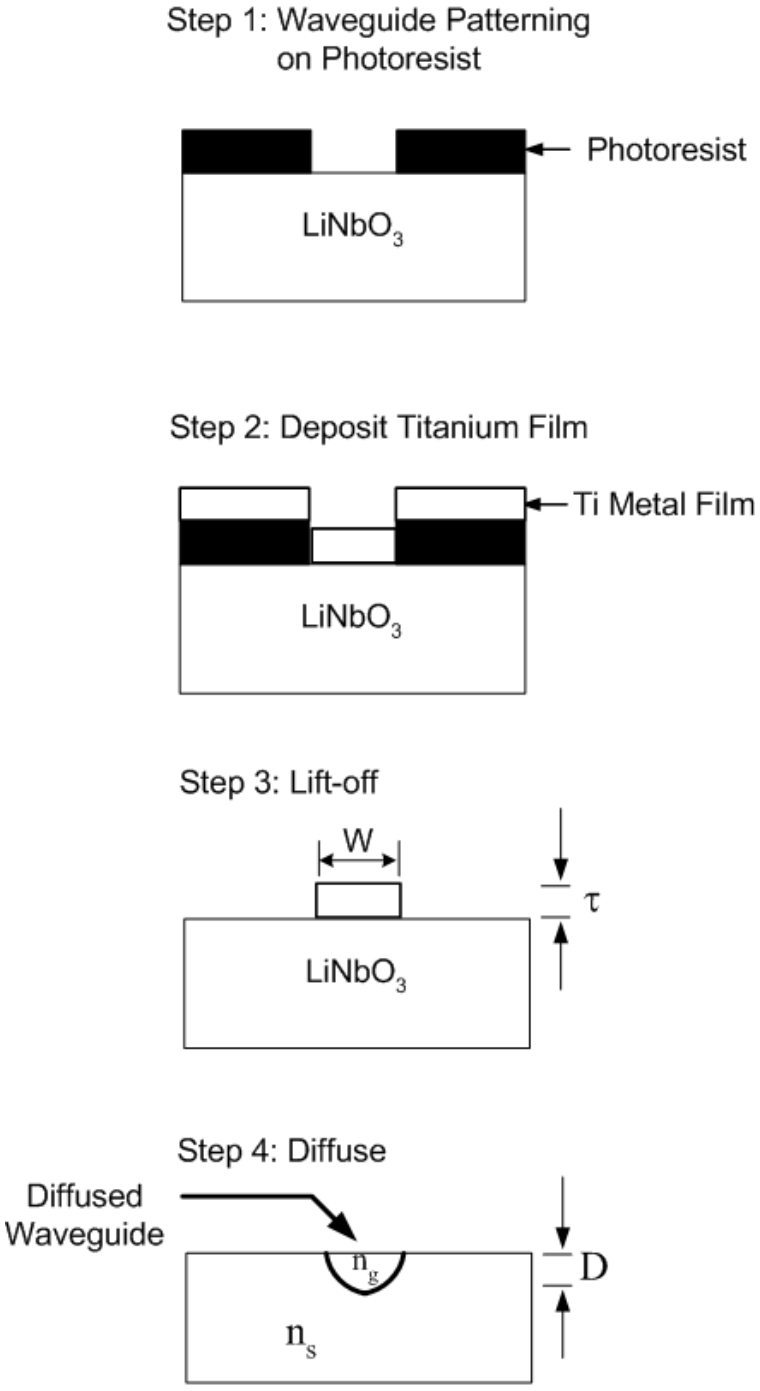


Figure 3.3: Procedure for fabricating strip Ti:$LiNbO_3$ waveguides.

guided optical propagation modes of the planar waveguide, thus causing a sharp drop in the intensity of light reaching the photodetector. To a rough approximation, the angular location of the modes determines the effective refractive index of the mode, while the angular difference between the modes determines the thickness of the planar waveguide. From the measured mode effective indices, a 1-D refractive index profile was constructed using the inverse WKB method devised by Chiang [63]. The resulting refractive index profile along with a corresponding Gaussian fit is shown in Figure 3.4(b). From this data, the surface refractive index difference $\Delta$n and 1/e diffusion depth $D_x$ were deduced to be 0.0136 and 8.0 $\mu$m, respectively. The effective indices were measured with a commercial (Metricon 2010) prism coupling instrument to a manufacturer's estimated accuracy of $\pm 0.0005$. The results are shown in Figure 3.4(a) along with calculated effective indices assuming the Gaussian profile given in Figure 3.4(b).

In order to estimate the channel waveguide modes and thus determine whether single-mode operation was possible, it was assumed that the 2-D refractive index profile $n(x, z)$ of the x-cut, Ti-indiffused channel waveguides could be approximated as follows [64]

$$n(x,z) = n_s + \Delta n \cdot \frac{1}{2}\left[\mathrm{erf}\left(\frac{W/2+z}{D_z}\right) + \mathrm{erf}\left(\frac{W/2-z}{D_z}\right)\right]\exp(-\frac{x^2}{D_x^2}) \qquad (3.29)$$

In Eq. (3.29), $n_s$ is the substrate index and $W$ is the pre-diffusion width of the E-beam deposited Ti strips. Furthermore for simplicity, the lateral and longitudinal diffusion depths $D_z$ and $D_x$, respectively, were assumed to be equal. Using Eq. (3.29) and scanning strip width, $W$, the range of the single TE mode operation for channel waveguide at $\lambda = 3.39$ $\mu$m were determined to be $W = 8$ $\mu$m – 21 $\mu$m by the beam propagation method. The $\Delta$n and $D_x$ values used in this calculation were 0.0136 and 8.0 $\mu$m, respectively, as given by our planar measurements (at $\lambda = 0.63$ $\mu$m) described

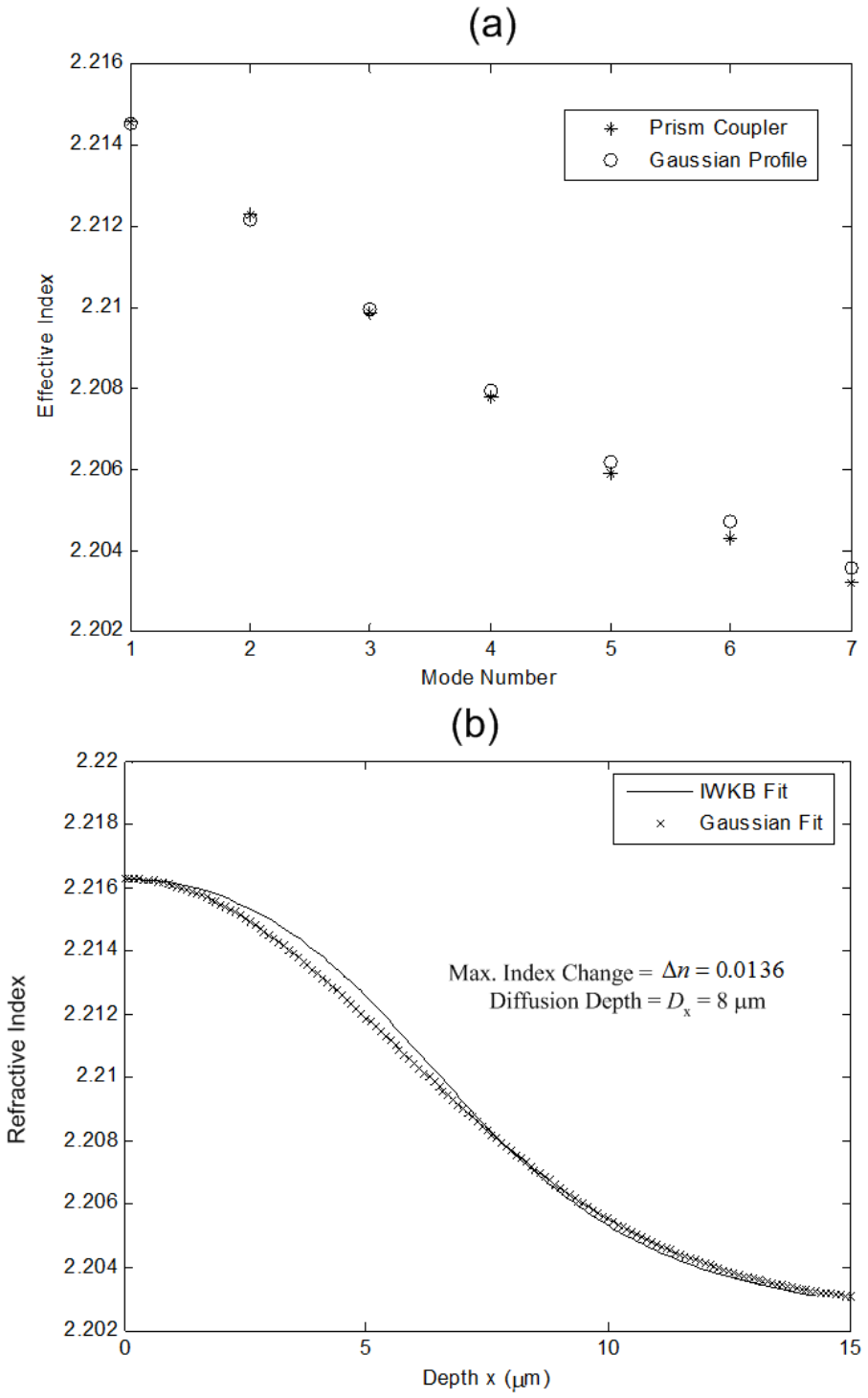


Figure 3.4: (a) Comparison of the measured effective indices and calculated effective indices for a Gaussian profile (b) Extraordinary index profile of planar waveguide.

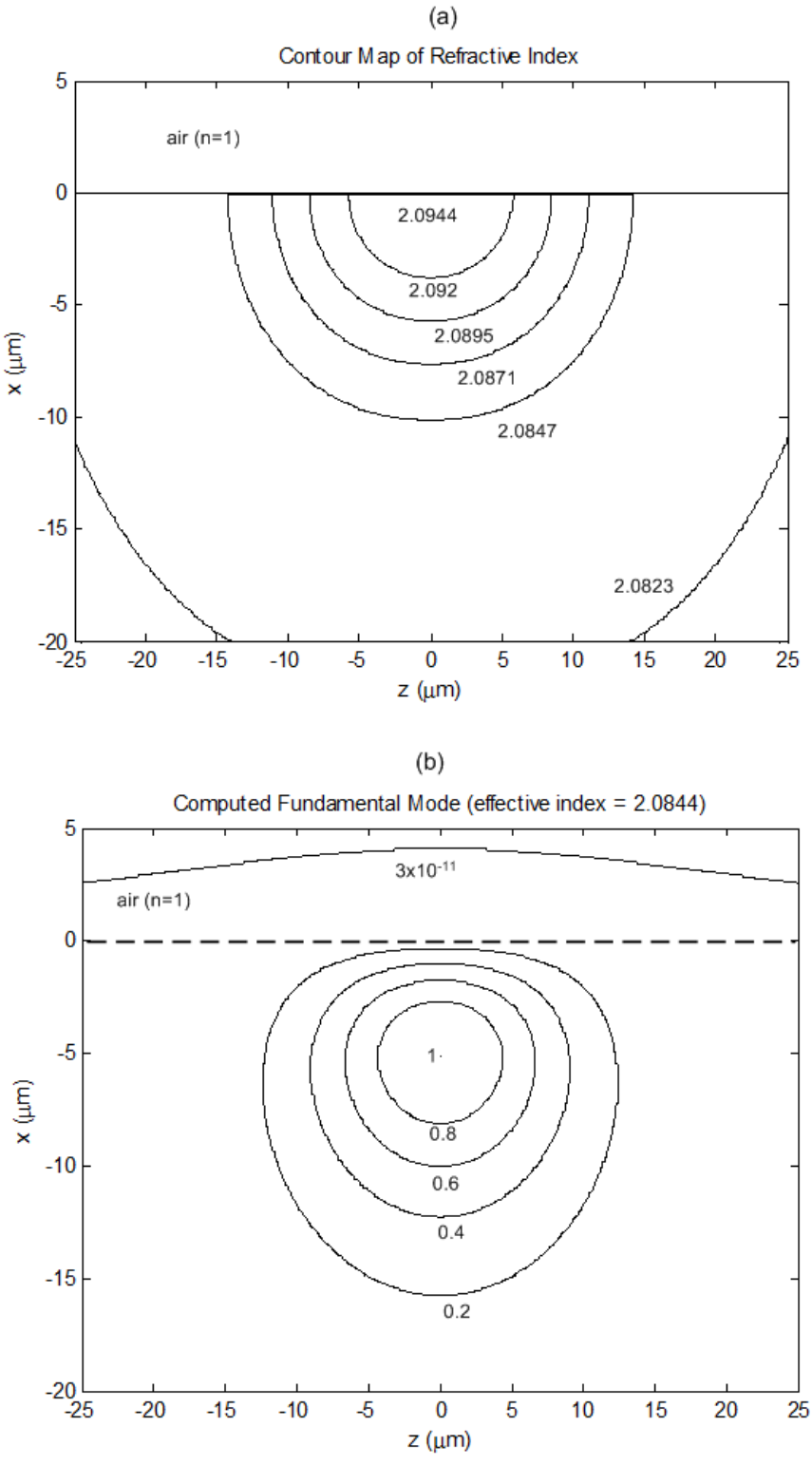


Figure 3.5: (a) Contour map of Refractive index (b) Computed TE-mode profile.

above. The substrate refractive index $n_s$ was taken to be 2.0823 at $\lambda = 3.39$ $\mu$m for the TE mode [65], though the results are relatively independent of the exact value used. With choice of $W = 18$ $\mu$m, the beam propagation results indicated that the channel waveguides should only support a single TE and a single TM mode at $\lambda = 3.39$ $\mu$m. Furthermore, the TM mode was very close to cut-off. The assumed refractive index profile given by Eq. (3.29) and the corresponding calculated TE mode profile are shown in the Figure 3.5(a) and 3.5(b), respectively. In these figures, the air-$LiNbO_3$ boundary is located at x = 0 $\mu$m. Since we do not know the explicit wavelength dependence of $\Delta$n much beyond 1.5 $\mu$m, our prediction that the waveguides will not be multi-moded at 3.39 $\mu$m relies on the expectation that $\Delta$n does not increase with wavelength. Such an assumption is consistent with data presented for the visible and near IR bands out to approximately 1.5 $\mu$m [64].

For the fundamental TE-polarized mode at $\lambda = 3.39$ $\mu$m, the calculated effective index, $n_{eff}$ (2.0844), lies 0.0021 above the substrate refractive index. A similar calculation shows that TM-polarized mode is near cut-off, and thus is expected to experience very high bending losses. The EO modulation results shown in Figure 3.12 indicate that the waveguide is single-moded in the L band, since the output response is quasi-periodic. Different spatial modes are orthogonal and thus do not beat against one another. Consequently if there were two (or more) discrete modes, each one will separately produce a quasi-periodic intensity variation as the optical path length in one arm is varied. The period of this variation (corresponding to each spatial mode) will depend on the wavelength and the effective index of the mode. Since the two modes have different effective indices, two (or more) intensity variations with different periods will be superimposed. Such a superposition does not yield a quasi-periodic variation.

## 3.4 Design, fabrication, and characterization of the device

The overall size of the fabricated three-beam combiner chip, as illustrated in Figure 3.6(a) is 60 mm (long) x 20 mm (wide) by 1 mm (thick). The device itself, excluding the electrical contact pads, occupies only 1.25 mm of the total chip width. A two-beam combiner, containing components similar to those contained in the three-beam device, is shown in Figure 3.6(b). This later device was characterized in our laboratory. The beam combiners contain three optical functions: spatial filtering based on single-mode waveguides with sufficient length, interferometric beam combining based on 3 dB symmetric directional couplers, and electrically-controlled phase modulation based on thin film metal electrodes. For the three-beam combiner, the photometric signal levels can be determined using linear combinations of the interferometric outputs ($I_{12+}$, $I_{12-}$,$I_{13+}$, $I_{13-}$, $I_{23+}$, and $I_{23-}$) using a scheme similar to that reported in [66].

### 3.4.1 Characterization of bending losses

The relatively small increase of refractive index obtained by Ti-indiffusion leads to weak confinement of optical modes, and thus greatly increases the losses in the bending regions. Therefore, waveguide bends of large radius of curvature must be used to minimize bending losses and keep the device size reasonable.

In order to characterize the bending losses, a set of S-shaped waveguide bends consisting of two back-to-back semi-circular arcs of constant radius of curvature R were fabricated as shown in Figure 3.7. The losses, including pure bending losses and those arising from abrupt curvature changes due to waveguide-to-waveguide transitions, were measured by comparing the throughput of these S-shaped bends to straight waveguide sections. The results are shown in Figure 3.8, along with an exponential fit, for values of $R$ between 6 and 22 cm. For circular arcs of radius $R$, the pure

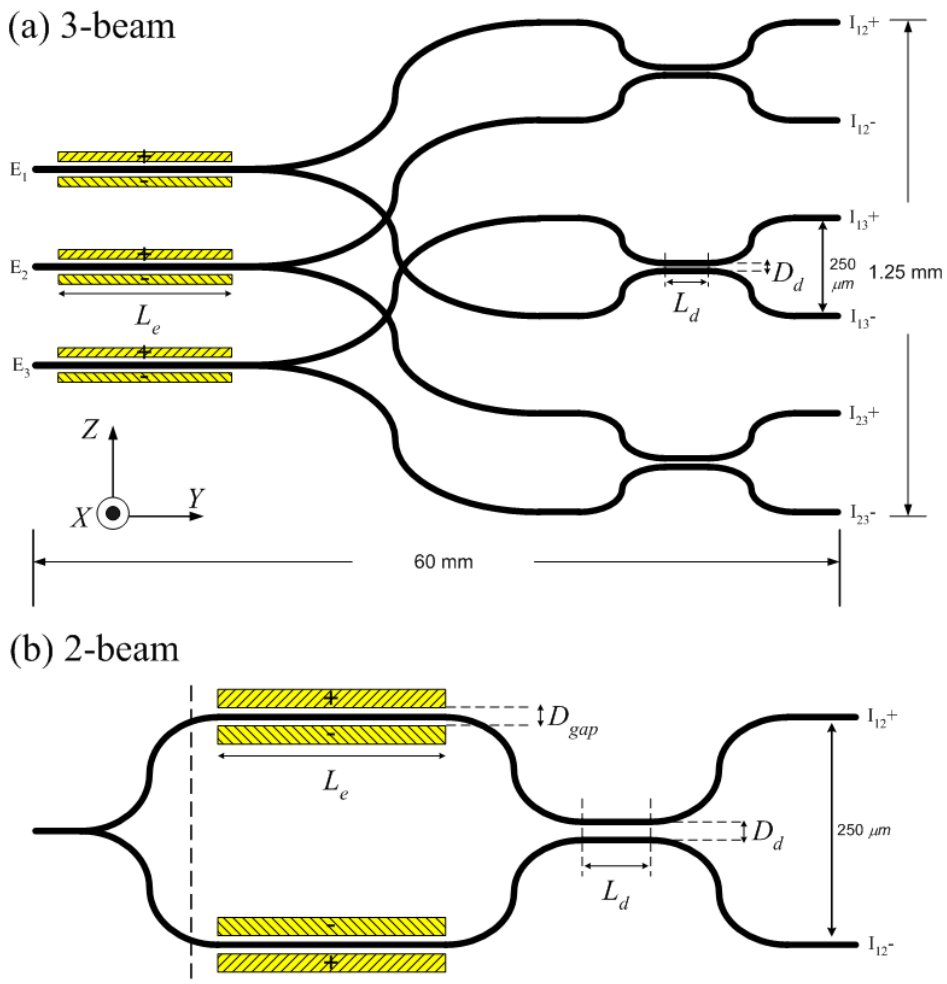


Figure 3.6: Layout of (a) fabricated three-beam combiner (b) two-beam combiner for device characterization (figures not drawn to scale).

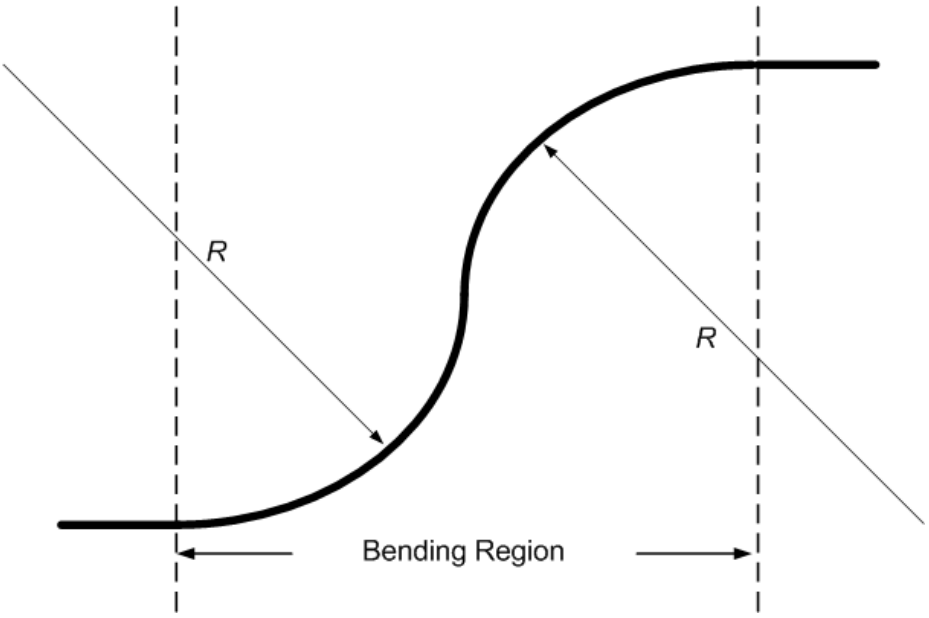


Figure 3.7: Two semi-circular arcs with radius of curvature $R$.

bending loss coefficient can be modeled as

$$\alpha(R) = C_1 \exp(-C_2 R) \text{dB/cm} \tag{3.30}$$

where parameters $C_1$ and $C_2$ are independent of $R$, but are functions of the waveguide parameters [67].

Although not excellent, the quality of the exponential fit indicates that the losses are dominated by pure bending as opposed to transition losses. According to the fit shown in Figure 3.8, the values of $C_1$ and $C_2$ at $\lambda = 3.39$ $\mu$m are 21.5 dB/cm and 0.16 cm$^{-1}$ for TE-mode and 18.2 dB/cm and 0.1 cm$^{-1}$ for TM-mode, respectively. Thus, the TM-mode experiences much higher losses. In order to minimize the TE-mode losses, the radius of curvature of the S-bends for the couplers was chosen to be as large as possible, i.e. 22 cm, while still allowing the 3-beam combiner to be fabricated using a 3 inch diameter $LiNbO_3$ wafer. The corresponding bending losses were 0.64 dB/cm and 2 dB/cm for the TE-mode and TM-mode, respectively.

By launching optical power, $P_1$, into a single input port of the two-beam combiner

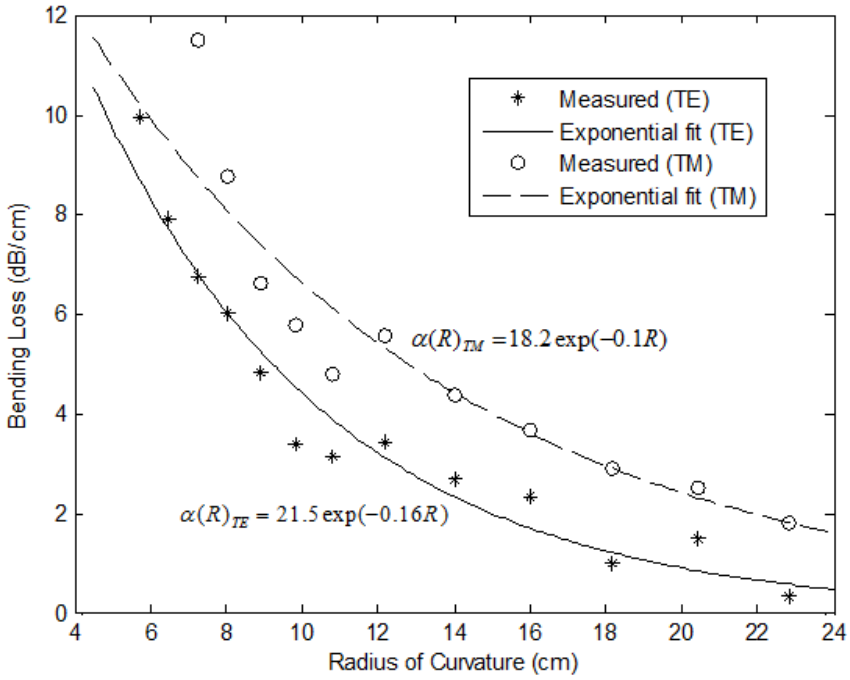


Figure 3.8: Bending loss measurements and exponential fit.

(without Y-splitter), the insertion loss of the device (i.e., $-10\log(P_{12+}+P_{12-})/P_1$) for the TE-mode was found to be 4.7 dB larger than that of a straight waveguide of the same length. We separately measured the excess loss of the two-beam integrated Y-splitter together with its associated waveguide bend and found it to be approximately 2 dB. Generally, Ti-indiffused $LiNbO_3$ waveguides exhibit low propagation loss ($< 0.1$ dB/cm). Thus the large losses reported here come primarily from the bending losses that are due to the weak confinement of the guided mode at $\lambda = 3.39$ $\mu$m. The use of larger $LiNbO_3$ wafers and/or thicker Ti-indiffused strips would allow us to increase the radii of curvature of the S-bends and/or to increase the mode confinement, greatly reducing insertion losses.

A waveguide intersected by another waveguide will perturb the electric field distribution of the modes, producing both excess loss and cross-talk [68]. Excess losses and cross-talk generally becomes more severe as the angle of crossing decreases. On the other hand, decreasing the crossing angle enables one to use bends with a larger radius

of curvature and/or to build smaller devices. Thus some compromise between performance and size must be reached. For the 3-beam combiner shown in Figure 3.6(a), the crossing angles were approximately $4^o$. A series of X-shaped waveguide crossings with different crossing angles were fabricated in order to estimate the cross-talk that the 3-beam combiner would experience. The cross-talk (i.e., output power from cross port/sum of output powers from the two output ports) for these X-shaped waveguide crossings was measured to be below 20 dB. The excess loss was not measured directly, but it is expected to be relatively small given the small value of the cross-talk.

### 3.4.2 Directional coupler design

For phase-matched operation of the directional coupler, the power transfer efficiency $\eta$ is given by the expression [69]

$$\eta = \sin^2(\kappa L_d + \varphi) \tag{3.31}$$

where $\kappa$ is the coupling coefficient and $L_d$ is the interaction length of the straight section. The phase term $\varphi$ corresponds to the coupling in the S-bend regions where $\kappa$ is not a constant. A set of directional couplers with center-to-center spacing $D_d = 26$ $\mu$m, S-bend radius of curvature $R = 6$ cm, and coupling lengths $L_d$ ranging from 3 to 9 mm were fabricated. The power transfer efficiencies of these couplers were measured, and the results are plotted in Figure 3.9 along with a fit to Eq. (3.31). From this fit, the value of $\kappa$ was found to be 0.48 mm$^{-1}$ for both the TE and TM fundamental modes.

For the final design with $R = 22$ cm, power splitting ratios were measured for three different values of $L_d$ (3.34, 3.44, and 3.54 mm). By fitting these three data points to Eq. (3.31) with same $\kappa$ experimentally determined in Figure 3.9, the $\varphi$ value corresponding to $R = 22$ cm was found to be 0.95. Thus it follows from Eq. (3.31)

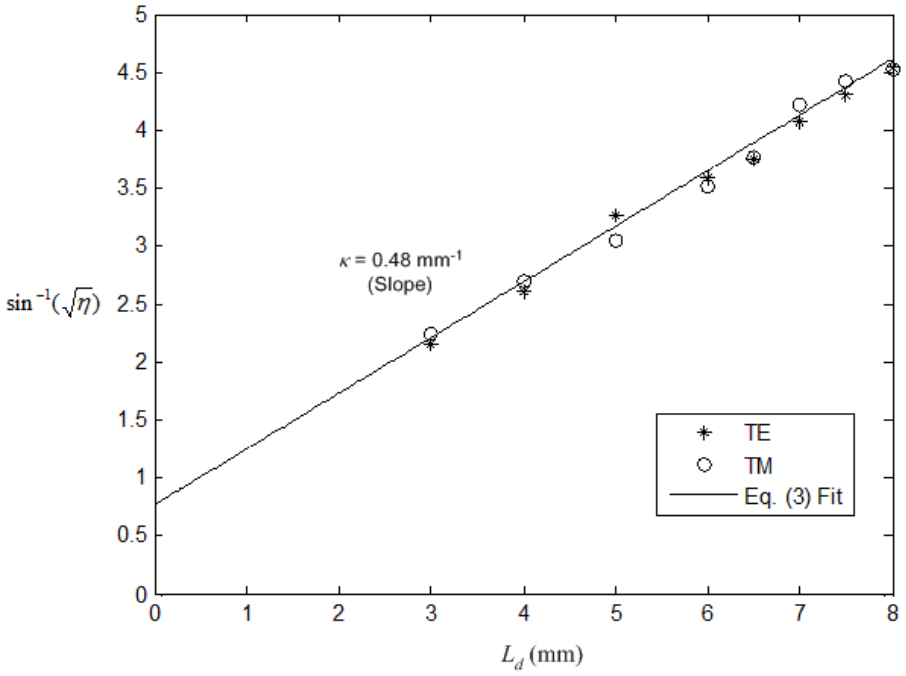


Figure 3.9: Experimentally determined coupling characteristics.

that an interaction length of approximately $L_d = 2900$ $\mu$m will correspond to the required 3 dB coupler. Using the HeNe laser operating at 3.39 $\mu$m, the measured power splitting ratio $\eta$ for TE-mode (TM-mode) of the directional coupler with $L_d = 2900$ $\mu$m and $R = 22$ cm was measured to be 48% (54%), corresponding to a fringe visibility of 99.9% (99.7%).

#### 3.4.2.1 Wavelength-dependent response

Long baseline, stellar interferometry measures fringe visibilities and phase closure. Deep nulling, as well as high contrast broadband fringe formation, requires that the beam combiner and fringe scanner operate achromatically. A lossless directional coupler is a four-port device. For monochromatic operation at wavelength $\lambda$, the squared-magnitudes of the complex-valued electric field amplitudes, $A_{out}$ and $B_{out}$,

measured at the two output ports can be written as [70]

$$
\begin{aligned}
|A_{out}|^2 = |A_{in}|^2[1 - C(\lambda)] \quad &+ \quad |B_{in}|^2 C(\lambda) - 2|A_{in}| \cdot |B_{in}| \sqrt{C(\lambda)[1 - C(\lambda)]} \\
&\cdot \sin(\angle A_{in} - \angle B_{in} + \phi_{int}(\lambda) + \theta_{ext}(\lambda)) \\
|B_{out}|^2 = |A_{in}|^2[1 - C(\lambda)] \quad &+ \quad |B_{in}|^2 C(\lambda) + 2|A_{in}| \cdot |B_{in}| \sqrt{C(\lambda)[1 - C(\lambda)]} \\
&\cdot \sin(\angle A_{in} - \angle B_{in} + \phi_{int}(\lambda) + \theta_{ext}(\lambda)) \qquad (3.32)
\end{aligned}
$$

where $A_{in}$ and $B_{in}$ are the complex-valued electric fields with amplitudes $|A_{in}|$, $|B_{in}|$ and phases $\angle A_{in}$, $\angle B_{in}$ measured at the two input ports, $C(\lambda)$ is the directional coupler's wavelength-dependent power cross-over ratio (i.e., $|B_{out}|^2/|A_{in}|^2$ when $B_{in} = 0$), $\phi_{int}(\lambda)$ is the wavelength-dependent phase introduced by the directional coupler, and $\theta_{ext}(\lambda)$ is an externally-induced phase shift between the two input beams. For the EO scanning reported here, the last of these quantities is given by

$$\theta_{ext}(\lambda) = \frac{2\pi}{\lambda} \Delta n_{eo}(\lambda) L_e \qquad (3.33)$$

where $\Delta n_{eo}(\lambda)$ is the wavelength-dependent EO-induced refractive index change and $L_e$ is the physical path length of the EO waveguide section. For broadband sources, Eq. (3.32) must be integrated across the source spectrum to derive the final fringe intensity. The directional coupler will be achromatic if and only if $C$ and $\phi_{int}$ are not wavelength-dependent. It is also clear from Eq. (3.33) that the path-length difference introduced by EO scanning is wavelength-dependent.

Symmetrical directional couplers are not achromatic devices. Several techniques, including the use of asymmetrical couplers, have been proposed and demonstrated to realize "wavelength-flattened" operation [71]. It is interesting to note, however, that most proposals to realize wavelength-flattened device operation consider only the directional coupler's power transfer characteristic (i.e., $C(\lambda)$ and ignore the wavelength-

dependent phase shift $\phi_{int}$. The phase shift determines the fringe position, and obtaining a wavelength-independent fringe position may be as important as realizing a wavelength-flattened intensity response. This is especially true for nulling applications. It is easily demonstrated that the phase response of a symmetrical directional coupler is wavelength-independent [70], while this is not the case for previously proposed wavelength-flattened, asymmetrical, directional couplers. The development of IO directional couplers and fringe scanners with enhanced achromaticity warrants further investigation.

### 3.4.3 Phase modulator

The push-pull configuration of electrodes was fabricated on the beam combiners using traditional photolithographic processing. 60 $\mu$m wide, 500 nm thick gold strips were evaporated next to the waveguides with an edge-to-edge electrode spacing $D_{gap}$ of 24 $\mu$m as shown in Figure 3.6(b). The electrode lengths $L_e$ on both the two-beam and three-beam combiners were chosen to be 1 cm. The direction of the applied electric field lies primarily along the optical axis (z-axis) of $LiNbO_3$, and thus the largest EO coefficient $r_{33}$ was utilized for the TE-mode. The EO-induced phase shift is given by Eq. (3.34)

$$\Delta\varphi = 2 \cdot \Gamma_{eff} \cdot \pi \cdot n^3 \cdot r \frac{V}{D_{gap}} \frac{L_e}{\lambda} \tag{3.34}$$

where $n$ is the refractive index of the $LiNbO_3$ substrate, $r$ is the EO coefficient ($r_{33}$ for the TE-mode and $r_{13}$ for the TM-mode) and $\Gamma_{eff}$ is factor between 0 and 1 that accounts for the spatial overlap between the applied electric field and the mode. A HeNe laser operating at 3.39 $\mu$m was launched into the Y-splitter of the two-beam combiner shown in Figure 3.6(b), while a triangular-shaped voltage waveform was applied to the electrodes and the power coming from one output arm of the directional coupler was measured. The results are shown in Figure 3.10 and correspond to a $V_\pi$ for the on-chip phase modulator of approximately 29 V/cm. This value is consistent

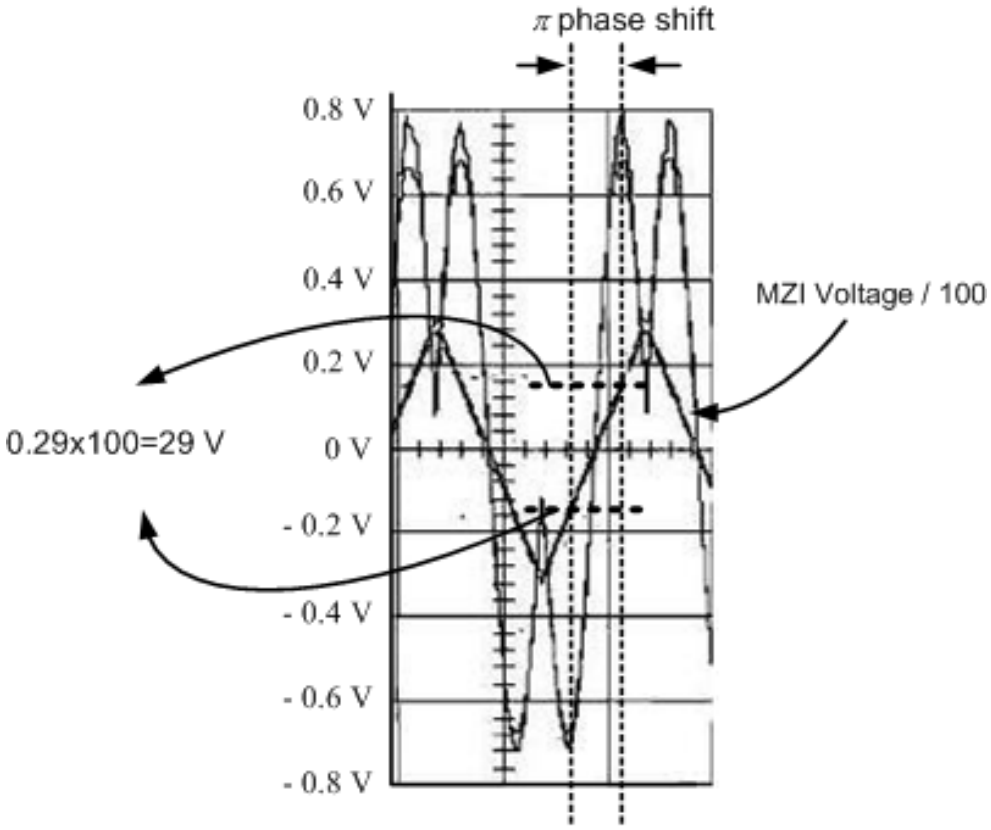


Figure 3.10: The oscilloscope traces of applied MZI voltage and output signal power.

with earlier reports [52], and corresponds to a $\Gamma_{eff}$ of approximately 0.5. Similarly, the measured $V_\pi$ (not shown) and the corresponding $\Gamma_{eff}$ for the TM-mode were found to be 165 V/cm and 0.25, respectively. It is worth noting that $\Gamma_{eff}$ is wavelength dependent. However, we are unable to characterize it due to lack of tunable IR source within the L band.

## 3.5 Laboratory white-light fringe measurement

The experimental set-up used to generate white-light fringes for the two-beam combiner in the laboratory is shown in Figure 3.11. HeNe lasers at 633 nm and 3.39 $\mu$m were used to facilitate alignment so that maximum power from the white light source could be coupled into the on-chip Y-splitter. Using UV fused silica aspheric lenses with focal length 15 mm, an 8 W thermal source (Boston Electronics IR-

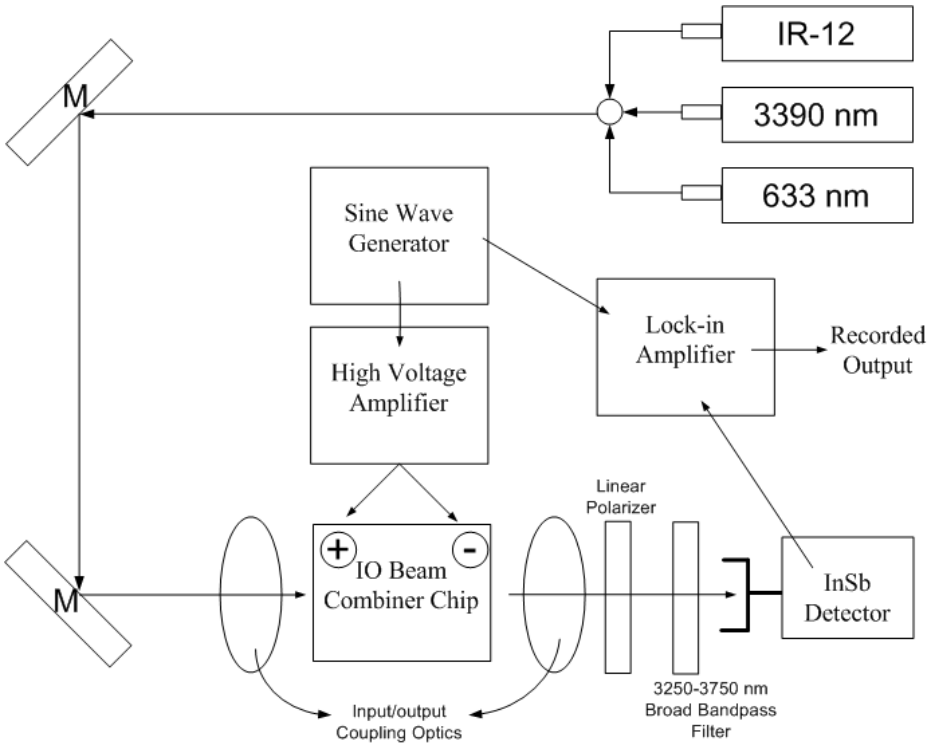


Figure 3.11: Experimental set-up for measurement of white-light interferograms.

12) operating at a blackbody temperature of 1170 K was coupled into the on-chip Y-splitter. The output of the directional coupler was imagined onto a liquid-nitrogen-cooled IR InSb detector after passing through a linear polarizer (TE) and a bandpass filter centered at 3.5 $\mu$m with a nearly 500 nm wide rectangular-shaped pass band. Due to the small amount of power that could be coupled into the waveguide from the broadband IR source, the signal at the InSb detector was buried in thermal noise and background light, and thus a lock-in amplifier was used to make the measurement. A DC voltage, which could be scanned from -175 V to +175 V, was applied to the electrodes. A small 1 KHz sinusoidal dither was added to this DC voltage, and a lock-in amplifier was used to synchronously measure the detector output. The value of the DC bias determined the position along the fringe.

The lock-in measurement technique did not permit us to measure the absolute value of the fringe visibility when using the broadband thermal source, but the derivative of the fringe. The measured derivative of the interferogram (TE-mode) is shown

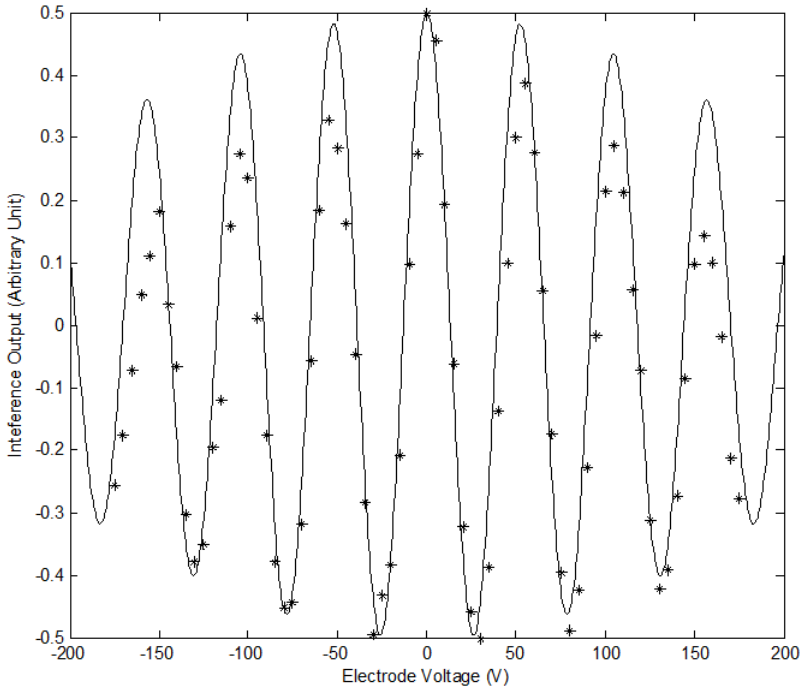


Figure 3.12: Derivative of white-light fringe and that of theoretical fringe with 500 nm bandwidth.

in Figure 3.12. Also shown in Figure 3.12 is the theoretically predicted derivative of the fringe given by Eq. (3.35) below

$$I_0 = \frac{1}{\Delta\lambda} \int_{\lambda_0 - \frac{\Delta\lambda}{2}}^{\lambda_0 + \frac{\Delta\lambda}{2}} \frac{1}{2} \cos\left(\frac{2\pi \Delta n L_e}{\lambda}\right) d\lambda$$
$$\approx \frac{1}{2} \cos \Delta\varphi_0 \cdot \frac{\sin(\Delta\varphi_0 \cdot \frac{\Delta\lambda}{2\lambda_0})}{\Delta\varphi_0 \cdot \frac{\Delta\lambda}{2\lambda_0}} \tag{3.35}$$

where $\lambda_0 = 3.5$ $\mu$m, $\Delta\lambda = 500$ nm, and $\Delta\varphi_0 = 2\pi\Delta n L_e/\lambda_0 = (\pi V)/V_\pi(\lambda_0)$ is the EO induced phase shift at $\lambda_0$. In deriving Eq. (3.35) the wavelength-dependent behavior of the directional coupler has been ignored, i.e., $C(\lambda)$ in Eq. (3.32) has been assumed to be equal to 0.5 independent of wavelength. In Figure 3.12 the $V_\pi$ for TE-mode was chosen to be 26.2 V, which is close to the value previously reported in Section 3.4.3, and gives the best fit to the experimental data. Based on the power splitting ratio reported in Section 3.4.2, the fringe visibility at 3.39 $\mu$m is approximately 99.9%. At the present time, we cannot fully explain the deviation of measured data from the theoretical fit at the larger electrode voltages. The wavelength dependence of the coupler as well as the wavelength dispersion of the EO-induced refractive index change would not result in the asymmetry of the fringes shown in Figure 3.12.

## 3.6 Discussion

Integrated-optic, astronomical, two-beam and three-beam, interferometric combiners have been designed and fabricated for operation in the L band, and the broadband on-chip electro-optic fringe scanning in titanium-indiffused, x-cut lithium niobate waveguides has been demonstrated for the first time. White-light fringes (TE-polarization) were produced in the laboratory using the two-beam combiner integrated with an on-chip Y-splitter. Using an applied electrode voltage of 350 V, it was possible to scan through approximately six fringes.

The devices exhibited relatively high waveguide losses in the bending regions due to the low-index contrast of the waveguides. Loss reduction is a key aspect of future development. Further optimization of the device layout, the use of larger wafers and/or thicker indiffused titanium strips is expected to reduce the losses to reasonable values. It should also be possible, using on-chip, polarization splitters to design devices that utilize both the TE and TM polarized light, thus capturing 3 dB more signal power. As discussed in Section 3.4.2.1, the response of directional couplers and EO-induced fringe scanners is generally not achromatic. Techniques need to be developed to suppress the wavelength-dependent operation of these devices, especially for applications that require deep nulls [72]. This three-beam combiner (shown in Figure 3.6) is equivalent to the most complex IO combiner that has been used for on-sky measurements. Its on-sky measurement potential, however, surpasses previous IO combiners because it operates in the L band and has on-chip fringe scanning capability. In the following chapter, the theoretical design of a broadband, achromatic, and polarization insensitive beam combiner is presented.

# CHAPTER IV

# Theoretical Design of Broadband Achromatic Astronomical Beam Combiner for the Mid-infrared Wavelength Region

## 4.1 Introduction

The direct imaging and characterization of Earth-like planets, especially those capable of supporting life, is one of the outstanding goals of modern astrophysics and science in general. Currently, stellar interferometry is one of the most promising approaches for achieving this goal. We have shown in Chapter III that IO devices are well suited to perform the beam combining function for stellar interferometry. In the infrared wavelength region, a host star is normally a million times brighter than the planet orbiting it, which is a major problem when trying to image the planet directly. Nulling interferometry offers the possibility to overcome this problem by attenuating the stellar light, thus enhancing the visibility of the planet. Generally, achromatic phase shifting and broadband achromatic beam combining functions are required for deep nulling, with nulling depths of $10^{-6}$ or better over the infrared spectrum. Although we can image the planet by nulling at a single wavelength, there are key reasons to use a broad wavelength band. First, there are several key biomarkers in the infrared spectrum from 6 $\mu$m to 18 $\mu$m. Second, the total integration time needed

to detect a planet increases as the spectral bandwidth is reduced.

In this chapter, we propose and present a theoretical design of an achromatic, broadband, polarization-insensitive, mode-evolution beam combiner suited for space-based nulling interferometry. The design is based on a system of three coupled waveguides. In Section 4.2, nulling interferometers and achromatic phase shifters are described, and different types of IO beam combiners are compared and discussed.

In Section 4.3, the theory of normal modes of a three coupled waveguide system is presented. A design of an achromatic, polarization-insensitive, mode evolution beam combiner is proposed in Section 4.4. In Section 4.6 and the Appendices A - E, the derivation of the coupled mode equations that describe the mode coupling between the local normal modes is given, and a condition for adiabatic operation is presented. In Section 4.7, a numerical design example of the proposed achromatic beam combiner, based on candidate technologies for waveguide fabrication in mid-infrared wavelength region, is presented and the device performance is numerically evaluated. In Section 4.8, the fabrication of a practical mid-infrared achromatic IO beam combiner is discussed.

## 4.2 Principle of operation for nulling interferometry

A nulling interferometer, based on a configuration proposed by Bracewell [58], consists of two collecting apertures separated by baseline length $B$ as shown in Figure 4.1. The difference in the optical path lengths for paths 1 and 2 is chosen such that the light from an on-axis source is canceled at the beam combiner. Suppose that the Bracewell telescope is oriented with its baseline in the $XY$-plane at an angle $\theta$ from the $X$-axis, pointing at a star along the $Z$-axis as shown in Figure 4.2. Each point in the star's neighborhood can be identified either by its angular coordinates $\phi$ and $\varphi$ as shown in the figure or by the Cartesian coordinates $x$ and $y$ of its image in the beam combining plane of the telescope. The image location is related to the

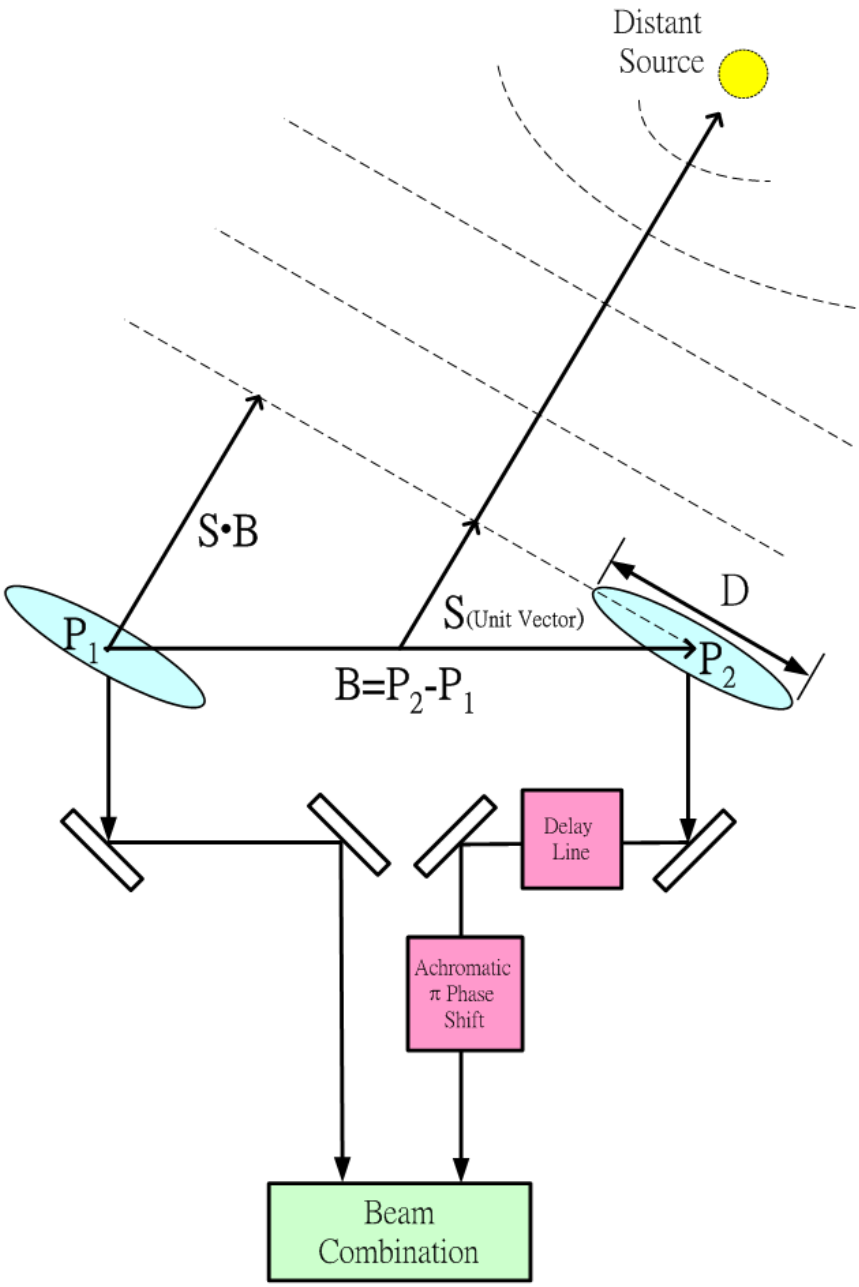


Figure 4.1: Nulling interferometer of single Bracewell configuration.

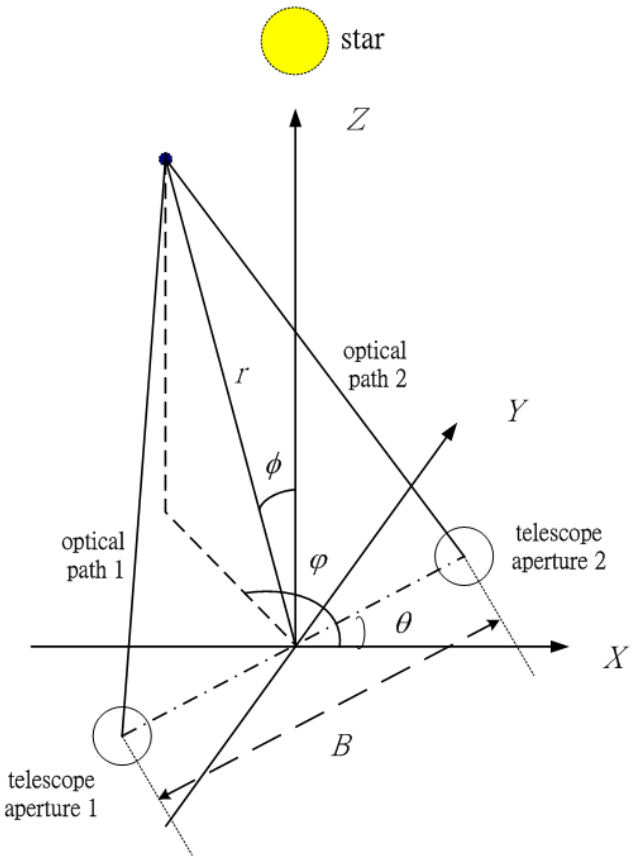


Figure 4.2: The Bracewell telescope with its baseline lying in the $XY$-plane and oriented at an angle $\theta$ from the $X$-axis, targeting a star along the $Z$-axis.

angular coordinates by the equation

$$(x, y) = M_s f_p \tan\phi(\cos\varphi, \sin\varphi) \tag{4.1}$$

where $f_p$ is the focal length of the primary mirror and $M_s$ is the magnification of the secondary mirror of the telescope apertures 1 and 2. For the light coming from the direction ($\phi$, $\varphi$) in the sky at wavelength $\lambda$, the phase difference between optical paths 1 and 2 is given by [58]

$$\begin{aligned}\Delta\Phi &= \frac{2\pi}{\lambda}\sqrt{\frac{B^2}{4} + Br\sin\phi\cos(\varphi-\theta) + r^2} - \sqrt{\frac{B^2}{4} - Br\sin\phi\cos(\varphi-\theta) + r^2} \\ &\approx \frac{2\pi B}{\lambda}\sin\phi\cos(\varphi-\theta), \text{ for } r \gg B.\end{aligned} \tag{4.2}$$

By introducing an achromatic $\pi$ phase-shift as shown in Figure 4.1, the two beams interfere destructively at the beam combining optics when $\Delta\Phi = 0$, and constructively when $\Delta\Phi = \pi$. The resulting intensity can be expressed as [58]

$$I(\Delta\Phi) = I(0)\sin^2(\frac{1}{2}\Delta\Phi) = I(0)\sin^2[\pi(B/\lambda)\sin\phi\cos(\varphi-\theta)] \tag{4.3}$$

A binary plot of $I/I(0)$ in the beam combining plane is shown in Figure 4.3 for $\theta$ = $45^o$. Each point in this plane corresponds to a point ($\phi$, $\varphi$) in the sky according to Eq. (4.1). The field of view is centered at $(x, y) = (\phi, \varphi) = (0, 0)$, which is the location of the target star. Any planet or other source of radiation located in the bright fringes of Figure 4.3 will produce a bright Airy pattern in the beam combining plane of that location. However, planets located in the dark fringes disappear from the image due to destructive interference. If the telescope is rotated around $Z$-axis while pointing at the fixed target star, $\theta$ will change continuously and the pattern of Figure 4.3 will rotate around its center. However, the image of a planet within the field of view will remain fixed while the fringes rotate. The planet's image thus

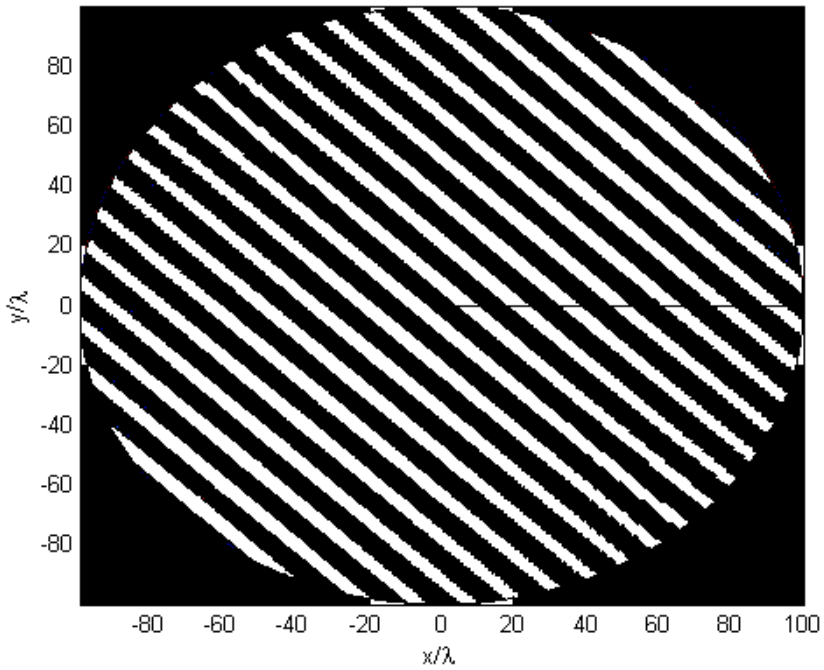


Figure 4.3: Binary plot of $I/I(0)$ in the beam combining plane for $B = 5$ m, $\theta = 45^o$, $\lambda = 10$ $\mu$m as a function of coordinates $x$ and $y$ where $M_s = 20$ and $f_p = 25$ cm is assumed.

waxes and wanes as the bright and dark fringes cross it one after the other. This is Bracewell's basic idea of searching for exoplanets orbiting other stars by using nulling interferometry.

### 4.2.1 Achromatic phase shifter

One of the the key components for achieving a deep broadband infrared null is the achromatic phase shifters. We do not address achromatic phase shift as part of this thesis. Currently, there are four promising techniques to achieve the required broadband deep null for exoplanet detection [73, 74]. The first approach uses multiple dispersive elements to achieve a quasi-achromatic phase shift across the passband. For a single wavelength $\lambda_0$, the nulling condition can be met by introducing a path delay difference between the two arms that results in a phase shift of $\pi$. For a

broadband spectrum, the phase shift, $\phi(\lambda)$, will not be achromatic and can be modeled as $\phi(\lambda) = \pi(\lambda_0/\lambda)$. By introducing an air delay in one optical path and some dielectric delay in the other path, the wavelength dependence of $\phi(\lambda)$ can be minimized. For example, a combination of ZnSe and ZnS plates will allow nulling depths of $10^{-8}$ over a 30% bandwidth centered at 10 $\mu$m [73].

The second approach for achieving an achromatic phase shift is called the through-focus field flip, which introduces an achromatic $\pi$ phase shift by exploiting diffraction [75]. When the beam passes through a focus, it acquires an achromatic phase change. This technique was first proposed by Jean Gay, et. al. [76]. The method is by nature broadband. Polarization sensitivity, however, is a known problem with this method. The angle of incidence varies across the pupil and creates a pupil-dependent change in the s-p polarization phase delay. Field flipping, an inversion of one pupil relative to the other, is a third approach that can be used to realize an achromatic phase shift. Due to the geometric nature of the field flip, this periscope architecture is also intrinsically achromatic.

The last approach is to use a deformable mirror to correct the intensity and phase as a function of wavelength from 8 $\mu$m to 12 $\mu$m. A novel compensator, the Adaptive Nuller, proposed by Peters et al. [74] uses a deformable mirror, with a continuous face sheet, to apply a high order independent adjustment to the amplitude and phase prior to injecting the combined light into a single-mode fiber. A schematic of the Adaptive Nuller, adapted from [74], is shown in Figure 4.4. This compensator has been used to produce rejection ratios of 82000:1 over a bandwidth of 3.2 $\mu$m centered at 10 $\mu$m.

### 4.2.2 Selection of integrated optic beam combiner

The other key component for achieving a broadband deep null is the broadband achromatic beam combiner. Generally, there are two basic types of planar, integrated

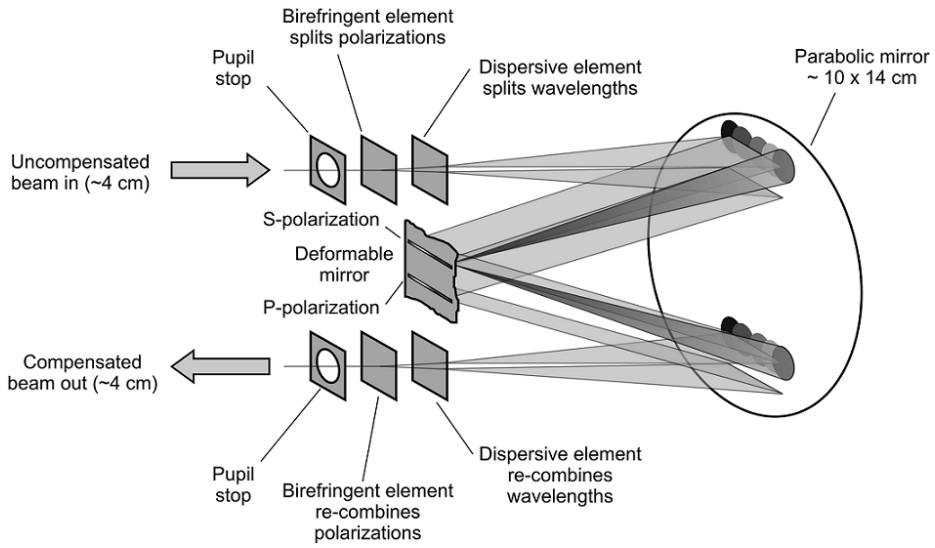


Figure 4.4: Schematic of the Adaptive Nuller [74]. Light in one arm of a nulling interferometer is balanced by splitting the polarizations and dispersing the wavelength, then adjusting the phases in each part of the spectrum with a deformable mirror prior to recombining the polarizations and wavelengths.

optic beam combiners: reversed-Y combiners and directional couplers as shown in Figure 4.5. The operation of a reversed-Y combiner is achromatic by symmetry. However, when used as a nulling interferometer, the reversed-Y combiner suffers an inevitable 3 dB loss of signal. On the other hand, directional coupler type beam combiners can capture the entire signal, and hence are theoretically lossless if we record both interferometric outputs and subtract them. Unfortunately, the operation of the directional coupler shown in Figure 4.5 is chromatic, and this wavelength dependence prevents the device from achieving deep broadband nulls. Various approaches have been suggested to mitigate this effect and achieve a wavelength flattened response by using asymmetric 2 by 2 directional couplers, where the coupling coefficients and waveguide widths are varied along the device length. This approach, however, does not yield an ultra-broadband achromatic response nor does it preserve the initial phase difference of the input beams at the interference outputs. Consider the beam combining function of a uniform directional coupler with a 3 dB coupling length of 300

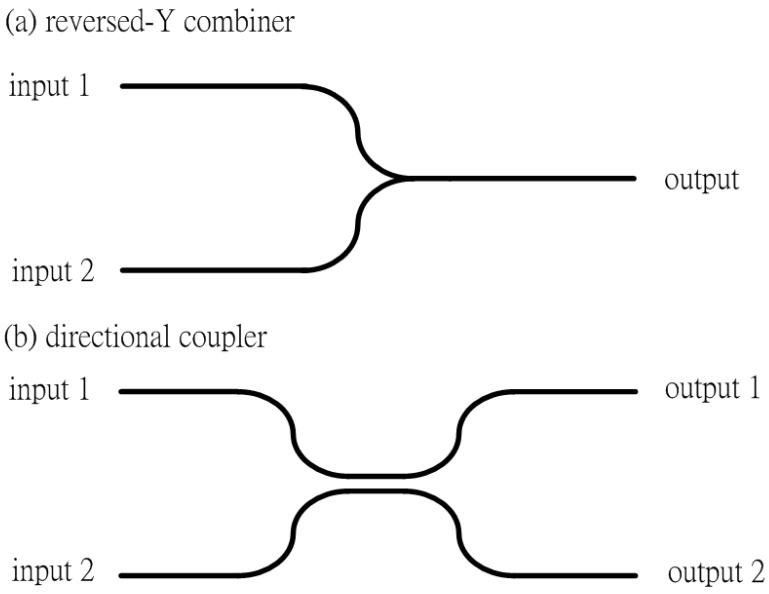


Figure 4.5: Schematic of (a) reversed-Y combiner (b) directional coupler.

$\mu$m and a 3 dB asymmetric directional coupler design (the magnitude of the rotation vector, $|\Omega(z)|$, is chosen at point A as described in the work of Paloczi et al. [77]). The wavelength dependence of the cross coupled power (i.e., the ratio of the power at output 2 to that at output 1 when the signal is launched into input 1) and the phase difference between the two outputs (when identical signals are launched into the two inputs) is shown in Figure 4.6. Although the phase response is achromatic for uniform coupler, its power splitting is highly chromatic. The asymmetric coupler has a flattened cross coupling power response, but its phase response is chromatic. Both chromaticity issues can seriously ruin the deep nulling condition required for exoplanets search. We will design a fully achromatic, polarization-insensitive, IO beam combiner based upon a three waveguide design.

## 4.3 Normal modes of three coupled waveguides

Before we go into the details of the design of the proposed fully-achromatic, broadband, mode-evolution beam combiner, we first develop representations for the normal

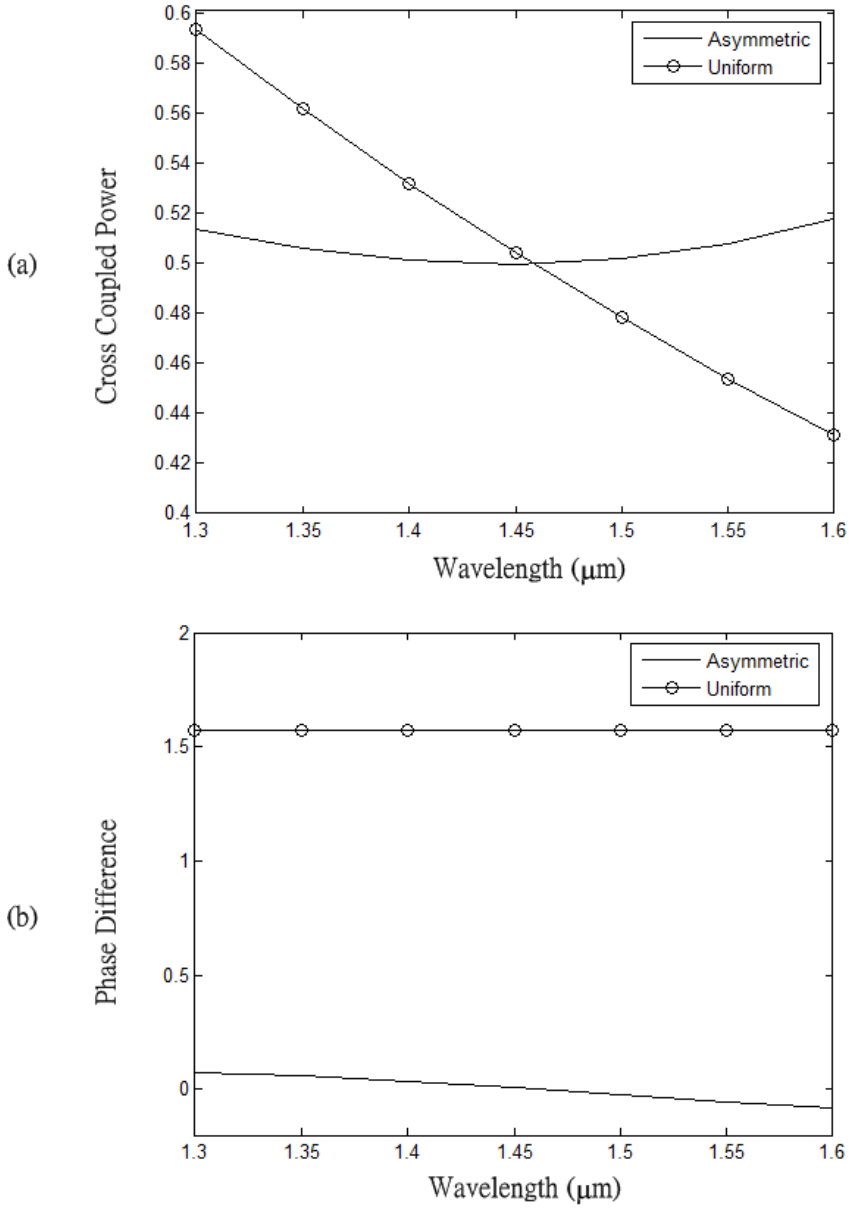


Figure 4.6: (a) Cross coupled power response and (b) phase difference response of the uniform directional coupler with a 3 dB coupling length of 300 $\mu$m and the asymmetric coupler.

modes of a symmetric three coupled waveguide system as shown in the Figure 4.7 [78]. The waveguides shown in Figure 4.7 are assumed to be uniform, i.e., do not change along the direction of propagation $z$. We also assume [1] that the total scalar (TE or TM) field,$E(x, y, z)$, of the combined three waveguide structure can be approximately written as the weighted sum of the normalized waveguide modes, $\Phi_1(x, y)$, $\Phi_2(x, y)$, $\Phi_3(x, y)$, associated with each individual waveguide expressed in the single $x$, $y$,$z$ coordinate system shown in Figure 4.7. Thus,

$$E(x, y, z) = \Psi(x, y) \exp(j\beta z) = \sum_{l=1}^{3} a_l(z)\Phi_l(x, y) \tag{4.4}$$

$$\int_{-\infty}^{+\infty}\int_{-\infty}^{+\infty} \Phi_l^2(x, y)\, dxdy = 1, \quad \text{and } l\text{=}1,\ 2,\ 3. \tag{4.5}$$

where $\Psi(x, y)$ is a real-valued quantity which describes the spatial profile of the mode and $\beta$ is the associated propagation constant. Coupled-mode equations describing this system are as following [78]:

$$\begin{aligned}
\frac{da_1}{dz} &= j\beta_1 a_1 + j\kappa_{12} a_2 + j\kappa_{13} a_3 \\
\frac{da_2}{dz} &= j\kappa_{12} a_1 + j\beta_2 a_2 + j\kappa_{23} a_3 \\
\frac{da_3}{dz} &= j\kappa_{13} a_1 + j\kappa_{23} a_2 + j\beta_3 a_3
\end{aligned} \tag{4.6}$$

where $\beta_1$ and $\beta_3$ are mode propagation constants for outer waveguides and $\beta_2$ is that of center waveguide, $\kappa_{ij}$ is the coupling coefficient between waveguides $i$ and $j$, and $a_1$, $a_2$, and $a_3$ are the complex-valued mode amplitudes associated with the individual waveguide modes in waveguides 1, 2 and 3, respectively. We further assume that the outer waveguides are identical and equidistant from the center waveguide, and thus $\kappa_{12} = \kappa_{23}$ and $\beta_1 = \beta_3$. It is easily verified that $a_1(z) = -a_3(z) = \exp(j\beta_0 z)$, $a_2(z) = 0$

[1] This assumption is valid when the waveguides are weakly coupled.

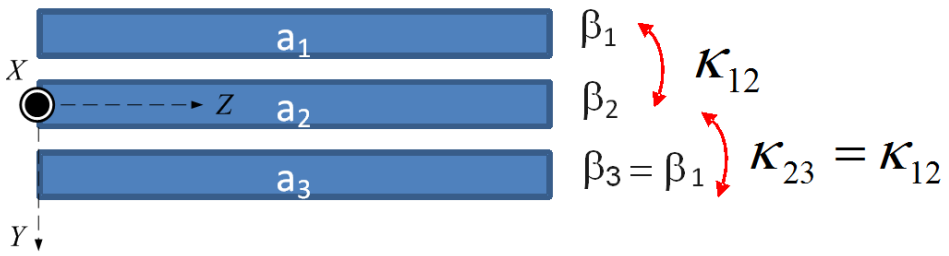


Figure 4.7: Three coupled channel waveguides. Waveguides 1 and 3 are identical and equidistant from waveguide 2.

with $\beta = \beta_1 - \kappa_{13}$ is a solution of Eq. (4.6) and hence a (antisymmetric) mode. The total field of this antisymmetric (as viewed about the x-z plane) mode of the original three waveguide structure can be written as

$$E_0(x, y, z) = \Psi_0(x, y) \exp(j\beta_0 z) \tag{4.7}$$

where

$$\Psi_0(x, y) = \left[\frac{1}{\sqrt{2}}\Phi_1(x, y) - \frac{1}{\sqrt{2}}\Phi_3(x, y)\right] \tag{4.8}$$

$$\beta_0 = \beta_1 - \kappa_{13} \tag{4.9}$$

Eq. (4.8) can be re-written as

$$\Psi_0(x, y) = \begin{pmatrix} \Phi_1(x, y) & \Phi_2(x, y) & \Phi_3(x, y) \end{pmatrix} A_0 \tag{4.10}$$

where

$$A_0 = \begin{pmatrix} 1/\sqrt{2} \\ 0 \\ -1/\sqrt{2} \end{pmatrix} \tag{4.11}$$

It will be convenient to refer to $A_0$ as the antisymmetric mode of the three waveguide structure. Similarly, if we consider the (symmetric modes) case $a_1(z) = a_3(z)$, Eq. (4.6) reduces to

$$\begin{aligned} \frac{da}{dz} &= j\beta_a a + jKb \\ \frac{db}{dz} &= jKa + j\beta_b b \end{aligned} \tag{4.12}$$

where

$$\begin{aligned} a(z) &= a_2(z) \\ b(z) &= \sqrt{2}a_1(z) \end{aligned} \tag{4.13}$$

and

$$\begin{aligned} \beta_a &= \beta_2 \\ \beta_b &= \beta_1 + \kappa_{13} \\ K &= \sqrt{2}\kappa_{12}. \end{aligned} \tag{4.14}$$

In Appendix A, the two nonzero solutions of Eqs. (4.12) are shown to be

$$\begin{aligned} a_+(z) &= d\exp(j\beta_+ z) \\ b_+(z) &= e\exp(j\beta_+ z) \end{aligned} \tag{4.15}$$

and

$$\begin{aligned} a_-(z) &= -e\exp(j\beta_- z) \\ b_-(z) &= d\exp(j\beta_- z) \end{aligned} \tag{4.16}$$

respectively, where

$$e^2 + d^2 = 1 \tag{4.17}$$

$$\bar{\beta} = \frac{1}{2}(\beta_1 + \beta_2 + \kappa_{13}) \tag{4.18}$$

$$\Delta\beta = \beta_2 - \beta_1 - \kappa_{13} \tag{4.19}$$

$$X = \frac{\Delta\beta}{2K} \tag{4.20}$$

$$d = \sqrt{\frac{1}{2}(1 + \frac{X}{\sqrt{1+X^2}})} \tag{4.21}$$

$$e = \sqrt{\frac{1}{2}(1 - \frac{X}{\sqrt{1+X^2}})} \tag{4.22}$$

$$\beta_\pm = \bar{\beta} \pm K\sqrt{1+X^2}. \tag{4.23}$$

The solutions given by Eqs. (4.15) and (4.16) correspond to the following pair of symmetric (with respect to the x-z plane) modes of the original three waveguide structure

$$E_+(x,y,z) = \Psi_+(x,y)\exp(j\beta_+ z) \tag{4.24}$$

where

$$\Psi_+(x,y) = \left[\frac{e}{\sqrt{2}}\Phi_1(x,y) + \frac{e}{\sqrt{2}}\Phi_3(x,y)\right] + d\Phi_2(x,y) \tag{4.25}$$

and

$$E_-(x,y,z) = \Psi_-(x,y)\exp(j\beta_- z) \tag{4.26}$$

where

$$\Psi_-(x,y) = \left[\frac{d}{\sqrt{2}}\Phi_1(x,y) + \frac{d}{\sqrt{2}}\Phi_3(x,y)\right] - e\Phi_2(x,y) \tag{4.27}$$

It is shown in Appendix A, that $\Psi_+(x,y)$ is the lowest order (i.e., $\beta_+ > \beta_0,\ \beta_-$) of the three modes. As with the antisymmetric mode given by Eqs. (4.10) and (4.11), it will be convenient to represent the $\Psi_+(x,y)$ and $\Psi_-(x,y)$ symmetric modes by

$$A_+ = \begin{pmatrix} e/\sqrt{2} \\ d \\ e/\sqrt{2} \end{pmatrix} \tag{4.28}$$

and

$$A_- = \begin{pmatrix} d/\sqrt{2} \\ -e \\ d/\sqrt{2} \end{pmatrix} \tag{4.29}$$

respectively. Thus

$$\Psi_+(x,y;z) = \begin{pmatrix} \Phi_1(x,y) & \Phi_2(x,y) & \Phi_3(x,y) \end{pmatrix} A_+ \tag{4.30}$$

$$\Psi_-(x,y;z) = \begin{pmatrix} \Phi_1(x,y) & \Phi_2(x,y) & \Phi_3(x,y) \end{pmatrix} A_-. \tag{4.31}$$

The total field for both symmetric modes and antisymmetric mode can be written as

$$E(x,y,z) = a(z)\Phi_2(x,y) + b(z)\left[\frac{1}{\sqrt{2}}\Phi_1(x,y) \pm \frac{1}{\sqrt{2}}\Phi_3(x,y)\right], \tag{4.32}$$

where the $+$ sign corresponds to symmetric modes and the $-$ sign corresponds to antisymmetric mode. The Eqs. (4.32) can be considered to describe an equivalent

two waveguide system where the two outer waveguides are considered as a single waveguide unit with mode $\frac{1}{\sqrt{2}}\Phi_1(x,y) \pm \frac{1}{\sqrt{2}}\Phi_3(x,y)$. The coupling coefficient, $K$, and the propagation constants, $\beta_a$ and $\beta_b$, of this equivalent two waveguide system are related to the coupling coefficients, $\kappa_{12}$ and $\kappa_{13}$, and the propagation constants, $\beta_1$ and $\beta_2$, of the original three waveguide system through Eqs. (4.14). For the + and − normal modes given by Eqs. (4.28) and (4.29), the relative power distribution between the center and outer waveguides (i.e., the ratio of $d^2$ to $e^2$) depends only on the waveguide parameter $X$ as indicated by Eqs. (4.21), (4.22), (4.28), and (4.29). Using Eqs. (4.8), (4.20) - (4.22), (4.25) and (4.27), the normal modes for $X = 0$, $X = -\infty$ and $X = +\infty$, are computed below and plotted in Figure 4.8. The values of the corresponding propagation constants give below also assume that the waveguides are sufficiently far apart so that $\kappa_{13} \approx 0$ and thus when $\beta_1 \neq \beta_2$, $\kappa_{13} < |\beta_1 - \beta_2|$.

Case (a): $X = -\infty$

$$A_0 = \begin{pmatrix} 1/\sqrt{2} \\ 0 \\ -1/\sqrt{2} \end{pmatrix}, \text{ propagation constant} = \beta_0 = \beta_1 - \kappa_{13} \text{ (antisymmetric mode)}$$

$$A_+ = \begin{pmatrix} 1/\sqrt{2} \\ 0 \\ 1/\sqrt{2} \end{pmatrix}, \text{ propagation constant} = \beta_+ = \beta_1 + \kappa_{13} \text{ (lowest order mode)}$$

$$A_- = \begin{pmatrix} 0 \\ -1 \\ 0 \end{pmatrix}, \text{ propagation constant} = \beta_- = \beta_2 \text{ (the third mode)} \tag{4.33}$$

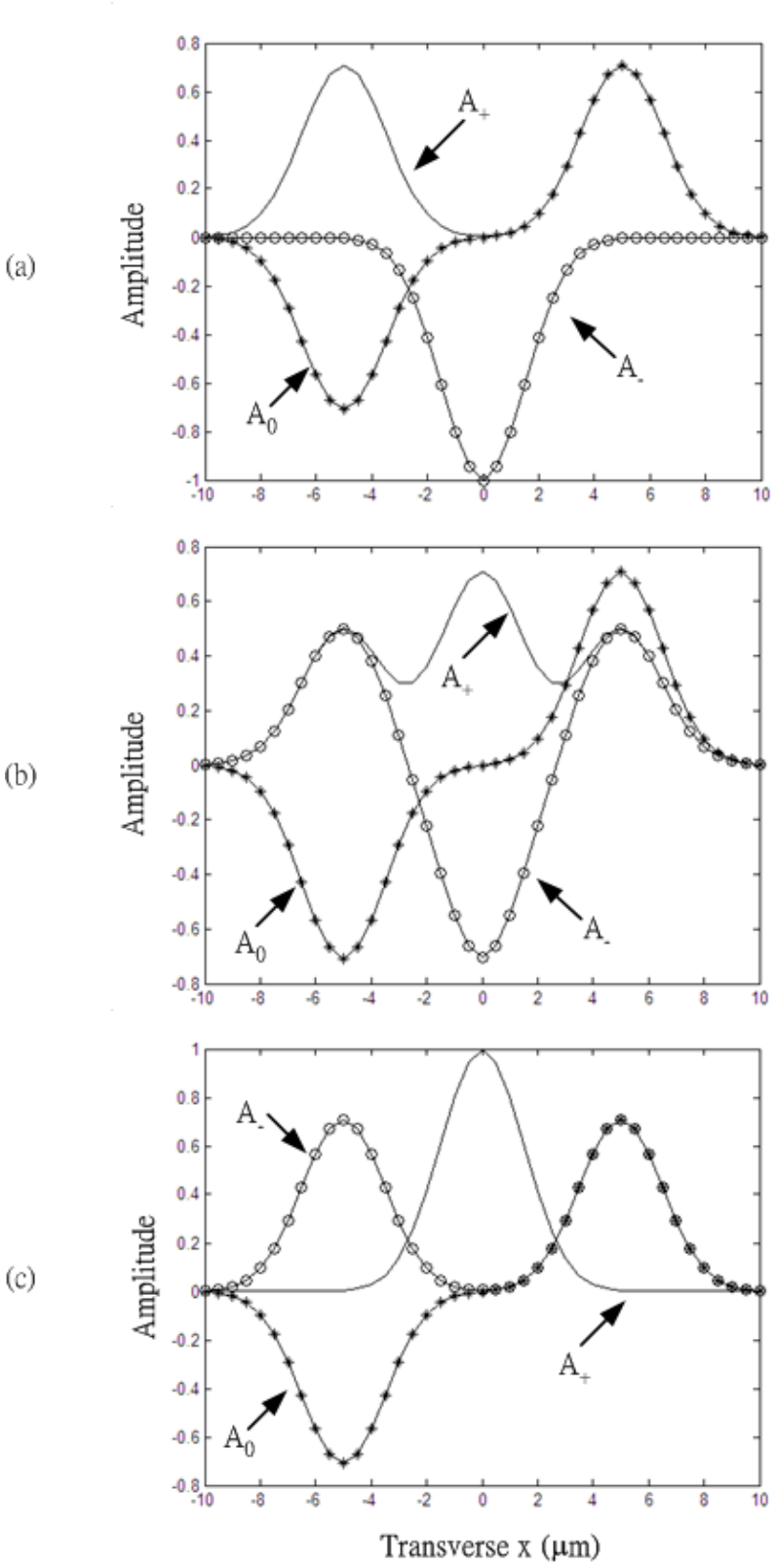


Figure 4.8: Mode profiles of the normal modes of a three waveguides system: (a) $X = -\infty$ (b) $X = 0$ (c) $X = +\infty$.

Case (b): $X = 0$

$$A_0 = \begin{pmatrix} 1/\sqrt{2} \\ 0 \\ -1/\sqrt{2} \end{pmatrix}, \text{ propagation constant} = \beta_0 = \beta_1 - \kappa_{13} \text{ (antisymmetric mode)}$$

$$A_+ = \begin{pmatrix} 1/2 \\ 1/\sqrt{2} \\ 1/2 \end{pmatrix}, \text{ propagation constant} = \beta_+ = \beta_1 + \kappa_{13} + K \text{ (lowest order mode)}$$

$$A_- = \begin{pmatrix} 1/2 \\ -1/\sqrt{2} \\ 1/2 \end{pmatrix}, \text{ propagation constant} = \beta_- = \beta_1 + \kappa_{13} - K \text{ (the third mode)}$$

(4.34)

Case (c): $X = +\infty$

$$A_0 = \begin{pmatrix} 1/\sqrt{2} \\ 0 \\ -1/\sqrt{2} \end{pmatrix}, \text{ propagation constant} = \beta_0 = \beta_1 - \kappa_{13} \text{ (antisymmetric mode)}$$

$$A_+ = \begin{pmatrix} 0 \\ 1 \\ 0 \end{pmatrix}, \text{ propagation constant} = \beta_+ = \beta_2 \text{ (lowest order mode)}$$

$$A_- = \begin{pmatrix} 1/\sqrt{2} \\ 0 \\ 1/\sqrt{2} \end{pmatrix}, \text{ propagation constant} = \beta_- = \beta_1 + \kappa_{13} \text{ (the third mode)} \quad (4.35)$$

In contrast to the normal modes of a structure that does not vary along the direction of propagation, the amplitudes of the local normal modes in a longitudinally varying waveguide structure are not constant as a function of position along the waveguide.

These longitudinally-varying local normal modes will be designated by $\Psi_0(x,y;z)$, $\Psi_+(x,y;z)$ and $\Psi_-(x,y;z)$ and expressed as

$$\begin{aligned} E_l(x,y;z) &= \Psi_l(x,y;z)\exp(j\beta_l(z)z) \\ &= a_1^{(l)}(z)\Phi_1(x,y;z) + a_2^{(l)}(z)\Phi_2(x,y;z) + a_3^{(l)}(z)\Phi_3(x,y;z) \end{aligned} \tag{4.36}$$

where $l = +,-,0$ and $\Phi_n(x,y;z)$, $n = 1,2,3$ are the local normal modes of the $n$ individual waveguides. Thus we define $A_l(z)$ as

$$A_l(z) = \exp(-j\beta_l(z)z)\begin{pmatrix} a_1^{(l)} \\ a_2^{(l)} \\ a_3^{(l)} \end{pmatrix}, \quad l = +,-,0 \tag{4.37}$$

and write

$$\Psi_l(x,y;z) = \begin{pmatrix} \Phi_1(x,y;z) & \Phi_2(x,y;z) & \Phi_3(x,y;z) \end{pmatrix} A_l(z), \quad l = +,-,0 \tag{4.38}$$

in analogy to Eqs. (4.10), (4.30) and (4.31). In general, the mode profile of a single local normal mode will evolve as it propagates along a longitudinally-varying waveguide structure. If we consider the three local normal modes of the combined longitudinally-varying three-waveguide structure, it is easily verified that $A_0(z)$, associated with the antisymmetric mode, remains constant along the whole structure. The other two symmetric local normal modes are identified by their mode order, i.e., by the relative magnitudes of their propagation constants, $\beta_+(z)$ and $\beta_-(z)$, respectively. The lowest order mode will be identified by the subscript +, and the third mode is identified by the subscript $-$ ($\beta_+ > \beta_-$). Generally, power transfer occurs between the local normal modes of a longitudinally-varying structure. As will be shown shortly, the degree of power transfer between the local normal modes is a function of the overlap parameter

between their spatial mode profiles, $\Psi_i(x,y;z)$ and $\Psi_j(x,y;z)$ where $i,j \in \{-,0,+\}$. This overlap parameter is given by

$$< \Psi_i|\frac{\partial}{\partial z}|\Psi_j > \equiv \int_{-\infty}^{+\infty}\int_{-\infty}^{+\infty} \Psi_i^*(x,y;z)\frac{\partial}{\partial z}\Psi_j(x,y;z)\,dxdy \tag{4.39}$$

It will also be shown later that, when $< \Psi_i|\frac{\partial}{\partial z}|\Psi_j >= 0$, as occurs for a structure that does not change along the propagation direction $z$, there is no power exchange. Similarly if the structure varies slowly enough in z, then $\frac{\partial}{\partial z}\Psi_j(x,y;z)$ will be small and $< \Psi_i|\frac{\partial}{\partial z}|\Psi_j >$ will be approximately zero. Thus there will be little power exchange between the local normal modes. It will be demonstrated in Section 4.6 that it is also possible to design waveguide structures that are neither invariant along z nor vary slowly along z for which $< \Psi_i|\frac{\partial}{\partial z}|\Psi_j > \approx 0$. When there is very little power transfer between the local normal modes, the mode propagation is said to be *adiabatic*.

## 4.4 Proposed design

Based on the functional forms of the local normal modes of a three coupled waveguide system obtained in Section 4.3, we propose the symmetric three coupled waveguide structure shown in Figure 4.9 to achieve broadband achromatic beam combining. The waveguide parameters are given in Table 4.1. We will assume for the moment that the device operation is adiabatic, and thus there is no power exchange between the local normal modes. The requirements needed to achieve adiabatic operation will be studied in Section 4.6. If we let the complex amplitudes of monochromatic input beams entering the outer waveguides port 1 and port 3 be $|a_1|\exp(j\phi_1)$ and $|a_3|\exp(j\phi_3)$, respectively, then the excited input field at $z = 0$ can be expressed as the linear combination of the local normal modes $A_+(0)$ and $A_0(0)$ of the coupled

structure at $z = 0$ as indicated below

$$|a_1|\exp(j\phi_1)\begin{pmatrix}1\\0\\0\end{pmatrix} = |a_1|\exp(j\phi_1)[\frac{1}{2}\begin{pmatrix}1\\0\\-1\end{pmatrix} + \frac{1}{2}\begin{pmatrix}1\\0\\1\end{pmatrix}]$$
$$= |a_1|\exp(j\phi_1)[\frac{1}{\sqrt{2}}A_0(0) + \frac{1}{\sqrt{2}}A_+(0)] \tag{4.40}$$

$$|a_3|\exp(j\phi_3)\begin{pmatrix}0\\0\\1\end{pmatrix} = |a_3|\exp(j\phi_3)[\frac{-1}{2}\begin{pmatrix}1\\0\\-1\end{pmatrix} + \frac{1}{2}\begin{pmatrix}1\\0\\1\end{pmatrix}]$$
$$= |a_3|\exp(j\phi_3)[\frac{-1}{\sqrt{2}}A_0(0) + \frac{1}{\sqrt{2}}A_+(0)] \tag{4.41}$$

$$\begin{pmatrix}|a_1|\exp(j\phi_1)\\0\\|a_3|\exp(j\phi_3)\end{pmatrix} = [\frac{1}{\sqrt{2}}|a_1|\exp(j\phi_1) - \frac{1}{\sqrt{2}}|a_3|\exp(j\phi_3)]A_0(0)$$
$$+ [\frac{1}{\sqrt{2}}|a_1|\exp(j\phi_1) + \frac{1}{\sqrt{2}}|a_3|\exp(j\phi_3)]A_+(0) \tag{4.42}$$

At the output of the device we wish to recover the input phase difference $\phi_1 - \phi_3$ and the full power, i.e., $|a_1|^2 + |a_3|^2$, of the incoming beams. The width of the center waveguide is kept fixed while the widths of the outer waveguides are equal to one another at all points along $z$ but are varied along $z$ to achieve the desired dephasing term $\Delta\beta = \beta_2 - \beta_1$. The coupling term, $\kappa_{12}$, and the dephasing term, $\Delta\beta = \beta_2 - \beta_1$, of the waveguide structure are chosen as indicated in Table 4.1.

Since the waveguide transition is assumed to be adiabatic, the power in each local normal mode will remain constant as the mode propagates along the length of the

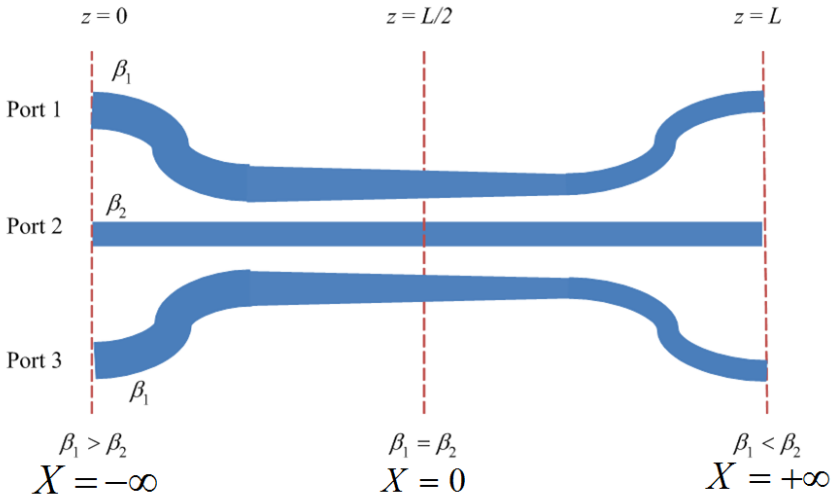


Figure 4.9: Schematic plot of proposed achromatic beam combiner.

| | $z = 0$ | $z = L/2$ | $z = L$ |
|---|---|---|---|
| Parameter $X$ | $-\infty$ | 0 | $+\infty$ |
| Dephasing $\Delta\beta$ | $< 0$ | 0 | $> 0$ |
| Coupling Coefficient $\kappa_{12}$ | 0 | $\kappa_{max}$ | 0 |
| Coupling Coefficient $\kappa_{13}$ | 0 | 0 | 0 |

Table 4.1: Device parameters are varied adiabatically along the structure from $z = 0$ to $z = L$.

structure, although the shape of each local normal mode will gradually evolve due to the adiabatic change of the waveguide parameters. According to Eqs. (4.33) and (4.35), the antisymmetric mode $A_0(0)$ and the lowest order symmetric mode $A_+(0)$ at $z = 0$ will evolve into the following forms,

$$A_0(L) = \begin{pmatrix} \frac{1}{\sqrt{2}} \\ 0 \\ \frac{-1}{\sqrt{2}} \end{pmatrix} \exp(-j \int_0^L \beta_0(z)\, dz) \tag{4.43}$$

$$A_+(L) = \begin{pmatrix} 0 \\ 1 \\ 0 \end{pmatrix} \exp(-j \int_0^L \beta_+(z)\, dz) \tag{4.44}$$

respectively, at the output $z = L$. Thus the total output at $z = L$ becomes

$$\begin{aligned} &(|a_1| \exp(j\phi_1) - |a_3| \exp(j\phi_3)) \exp(-j \int_0^L \beta_0(z)\, dz) \frac{1}{2} \begin{pmatrix} 1 \\ 0 \\ -1 \end{pmatrix} \\ &+ \\ &(|a_1| \exp(j\phi_1) + |a_3| \exp(j\phi_3)) \exp(-j \int_0^L \beta_+(z)\, dz) \frac{1}{\sqrt{2}} \begin{pmatrix} 0 \\ 1 \\ 0 \end{pmatrix} \end{aligned} \tag{4.45}$$

Therefore, the intensities at output port 1, 2, and 3 at $z = L$ are

$$\frac{1}{4} |\, |a_1| \exp(j\phi_1) - |a_3| \exp(j\phi_3)\, |^2 = \frac{1}{4}(|a_1|^2 + |a_3|^2) - \frac{1}{2}|a_1||a_3| \cos(\phi_1 - \phi_3)$$

$$: \text{ at output ports 1 and 3} \tag{4.46}$$

$$\frac{1}{2} |\, |a_1| \exp(j\phi_1) + |a_3| \exp(j\phi_3)\, |^2 = \frac{1}{2}(|a_1|^2 + |a_3|^2) + |a_1||a_3| \cos(\phi_1 - \phi_3)$$

$$: \text{ at output port 2} \tag{4.47}$$

From these expressions we see that the total power in all three waveguides combined is $|a_1|^2 + |a_3|^2$, and thus there is no loss in power. Furthermore, the input phase difference, $\phi_1 - \phi_3$, is preserved in the output interference term, $|a_1||a_3|\cos(\phi_1 - \phi_3)$, which is wavelength and polarization independent, guaranteeing fully achromatic and polarization-insensitive operation.

## 4.5 Chromatic operation of directional couplers

In order to understand why two waveguide directional couplers are not achromatic, consider the device shown in Figure 4.5(b). For simplicity, we will assume that the waveguides are weakly coupled and uniform along z [1]. The two local normal modes, as shown in Appendix A, of the combined structure can be written as

$$E_+(x,y,z) = \Psi_+(x,y)\exp(j\beta_+ z) \tag{4.48}$$

$$E_-(x,y,z) = \Psi_-(x,y)\exp(j\beta_- z) \tag{4.49}$$

where

$$\Psi_+(x,y) = \frac{1}{\sqrt{2}}\Phi_1(x,y) + \frac{1}{\sqrt{2}}\Phi_2(x,y) \tag{4.50}$$

$$\Psi_-(x,y) = \frac{1}{\sqrt{2}}\Phi_1(x,y) - \frac{1}{\sqrt{2}}\Phi_2(x,y) \tag{4.51}$$

As with the local normal modes of a three waveguide system, $\Psi_+(x,y)$ and $\Psi_-(x,y)$ can be conveniently represented by

$$A_+ = \begin{pmatrix} \frac{1}{\sqrt{2}} \\ \frac{1}{\sqrt{2}} \end{pmatrix} \tag{4.52}$$

[1] The conclusions given below can also be extended to the case where the waveguides are non-uniform along the direction of propagation.

and

$$A_- = \begin{pmatrix} \frac{1}{\sqrt{2}} \\ -\frac{1}{\sqrt{2}} \end{pmatrix} \tag{4.53}$$

respectively. If we let the complex amplitudes of monochromatic input beams entering the input waveguides 1 and 2 be $|a_1|\exp(j\phi_1)$ and $|a_2|\exp(j\phi_2)$, respectively, then the excited input field at $z = 0$ can be expressed as the linear combination of the local normal modes $A_+(0)$ and $A_-(0)$ of the coupled structure at $z = 0$ as indicated below

$$\begin{aligned} \begin{pmatrix} |a_1|\exp(j\phi_1) \\ |a_2|\exp(j\phi_2) \end{pmatrix} &= \left[\frac{1}{\sqrt{2}}|a_1|\exp(j\phi_1) + \frac{1}{\sqrt{2}}|a_2|\exp(j\phi_2)\right] A_+(0) \\ &+ \left[\frac{1}{\sqrt{2}}|a_1|\exp(j\phi_1) - \frac{1}{\sqrt{2}}|a_2|\exp(j\phi_2)\right] A_-(0) \end{aligned} \tag{4.54}$$

The operation of the coupler as a beam combiner can be described by propagating each local normal modes $A_+$ and $A_-$ separately to the end of the device and combining them at the output. Since the device is uniform along the propagation direction $z$ there will be no coupling between the local normal modes. The total output at $z = L$ becomes

$$\begin{aligned} &\left[\frac{1}{\sqrt{2}}|a_1|\exp(j\phi_1) + \frac{1}{\sqrt{2}}|a_2|\exp(j\phi_2)\right] \exp(j\beta_+ L) \begin{pmatrix} \frac{1}{\sqrt{2}} \\ \frac{1}{\sqrt{2}} \end{pmatrix} \\ &\qquad + \\ &\left[\frac{1}{\sqrt{2}}|a_1|\exp(j\phi_1) - \frac{1}{\sqrt{2}}|a_2|\exp(j\phi_2)\right] \exp(j\beta_- L) \begin{pmatrix} \frac{1}{\sqrt{2}} \\ -\frac{1}{\sqrt{2}} \end{pmatrix} \end{aligned} \tag{4.55}$$

Therefore, the intensities at outputs 1 ($I_{o1}$) and 2 ($I_{o2}$) at $z = L$ are

$$\begin{aligned} I_{o1} =& \frac{1}{2}|a_1|^2[1+\cos(\Delta\beta L)] \\ &+ \frac{1}{2}|a_2|^2[1-\cos(\Delta\beta L)] \\ &- |a_1||a_2|\cos(\Delta\phi)\cos(\Delta\beta L) \\ &+ |a_1||a_2|\cos(\Delta\phi - \Delta\beta L) \end{aligned} \tag{4.56}$$

$$\begin{aligned} I_{o2} =& \frac{1}{2}|a_2|^2[1+\cos(\Delta\beta L)] \\ &+ \frac{1}{2}|a_1|^2[1-\cos(\Delta\beta L)] \\ &- |a_1||a_2|\cos(\Delta\phi)\cos(\Delta\beta L) \\ &+ |a_1||a_2|\cos(\Delta\phi + \Delta\beta L) \end{aligned} \tag{4.57}$$

where $\Delta\beta = \beta_+ - \beta_-$ and $\Delta\phi = \phi_1 - \phi_2$, respectively. We can see that the output intensities depend on the difference of propagation constants, $\Delta\beta$, of the local normal modes. If $\Delta\beta L = \pi/2$ independent of wavelength, then Eqs. (4.56) and (4.57) reduce to

$$I_{o1} = \frac{1}{2}[|a_1|^2 + |a_2|^2 + |a_1||a_2|\sin(\Delta\phi)] \tag{4.58}$$

and

$$I_{o2} = \frac{1}{2}[|a_1|^2 + |a_2|^2 - |a_1||a_2|\sin(\Delta\phi)] \tag{4.59}$$

respectively. Thus if $\Delta\beta$ is not wavelength dependent, then the input phase difference, $\Delta\phi$, appears in the output interference terms, $\pm|a_1||a_2|\sin(\Delta\phi)$, unperturbed and without any wavelength dependence. The difference, $\Delta\beta$, of the local normal mode propagation constants, however, is wavelength dependent, and hence device operation will not be achromatic according to Eqs. (4.56) and (4.57). Note that the operation of

the two beam combiner described in this section relies on the interference of the two local normal modes and this interference is inherently wavelength dependent since $\Delta\beta$ is wavelength dependent. In contrast the three beam combiner described in Section 4.4 does not rely on the interference between the local normal modes. In fact the $A_0$ and $A_+$ modes are spatially separated at $z = L$. The $A_0$ mode at $z = L$ is confined to the two outer waveguides and the $A_+$ mode at $z = L$ is confined to the central waveguide. Thus the three beam combiner yields achromatic operation provided there is no coupling between the local normal modes. Furthermore if the inner waveguide of the three beam combiner is uniform along the direction of propagation, and if the two outer waveguides are identical and symmetrically offset from the center waveguide, then the device achieves an achromatic null when the beams launched into waveguide 1 and 3 are of equal amplitude and 180 degrees out of phase. This achromatic null will exist even if there is coupling between the $A_+$ and $A_-$ local normal modes.

## 4.6 Coupling of local normal modes

The definition of a slow or adiabatic waveguide transition is a transition between two waveguide structures that occurs gradually with propagation distance so that negligible power transfer occurs between the normal modes as they propagate from one structure to the other. Lack of mode conversion facilitates device design and can lead to wavelength insensitive operation as seen in Section 4.4. Conventionally, the suppression of mode conversion has been achieved by slowly varying the waveguide structure along the direction of propagation. It was recently suggested, however, that slow longitudinal variation, though sufficient, is not necessary to achieve adiabatic operation. More generally, the suppression of mode conversion is rooted in the small magnitude of the nonadiabatic term itself [3]. Thus conventional notions of adiabaticity based on the slow interaction can be abandoned, and a new and different type of adiabaticity based on a controlled interaction can be exploited. In the following

sections, the coupling equations governing the power transfer between local normal modes and the expression for the nonadiabatic term will be derived.

### 4.6.1 Quasi-vector wave equation

In order to calculate the spatial variation of electric field $\mathbf{E}(x, y, z)$ and magnetic field $\mathbf{H}(x, y, z)$ of an optical waveguide, we will derive the vector wave equation starting with time-harmonic form of Maxwell's equations. The time dependence of the field is of the form $\exp(-j\omega t)$. The dielectric constant $\epsilon(x, y, z)$ of a waveguide is related to its refractive index $n(x, y, z)$ by $\epsilon = \epsilon_0 n^2$, where $\epsilon_0$ is the free space electric permittivity, and the magnetic permeability is assumed to be its free space value ($\mu = \mu_0$) everywhere. Under these conditions and assuming that the regions are free of charges and current, Maxwell's equations are written as

$$\nabla \times \mathbf{E} = j\omega\mu\mathbf{H} \tag{4.60}$$

$$\nabla \times \mathbf{H} = -j\omega\epsilon\mathbf{E}. \tag{4.61}$$

Taking the curl of Eq. (4.60) and substituting Eq. (4.61), we obtain

$$\nabla \times \nabla \times \mathbf{E} = j\omega\mu\nabla \times \mathbf{H} = \omega^2\mu\epsilon\mathbf{E}. \tag{4.62}$$

Using the vector identity $\nabla \times \nabla \times \mathbf{E} = \nabla(\nabla \cdot \mathbf{E}) - \nabla^2\mathbf{E}$, we obtain

$$\begin{aligned} &\Rightarrow \quad \nabla(\nabla \cdot \mathbf{E}) - \nabla^2\mathbf{E} = \omega^2\mu\epsilon\mathbf{E} = k_0^2 n^2\mathbf{E} \\ &\Rightarrow \quad \nabla^2\mathbf{E} + k_0^2 n^2\mathbf{E} - \nabla(\nabla \cdot \mathbf{E}) = 0, \end{aligned} \tag{4.63}$$

where $k_0 = \omega/c = 2\pi/\lambda_0$ is the free space wavenumber, $c = 1/\sqrt{\mu\epsilon_0}$ and $\lambda_0$ are the speed and the wavelength of light in free space respectively. From $\nabla \cdot \mathbf{D} = \rho$ and the condition that the regions are free of charges ($\rho = 0$), we can express $\nabla \cdot \mathbf{E} =$

$-2(\nabla \ln n) \cdot \mathbf{E}$ and substitute this into Eq. (4.63) to obtain the vector wave equation

$$(\nabla^2 + k_0^2 n^2)\mathbf{E} + 2\nabla((\nabla \ln n) \cdot \mathbf{E}) = 0. \tag{4.64}$$

Now let's consider quasi-TE mode (i.e., $E_y \gg E_x$ and $E_y \gg E_z$) or quasi-TM mode (i.e., $E_x \gg E_y$ and $E_x \gg E_z$) in Cartesian coordinate and write the scalar (either y-component TE or x-component TM) electric field of the waveguide as

$$E_i(x, y; z) = \Phi_i(x, y; z) \exp(j\beta_0^{(i)} z), \quad i = x \text{ or } y \tag{4.65}$$

where $\Phi_i(x, y; z)$ is the slowly varying field profile along the propagation direction $z$ and $\beta_0 = n_0 k_0$ is the nominal propagation constant and $n_0$ is the nominal effective index of the optical mode. If we substitute Eq. (4.65) into Eq. (4.64), apply the paraxial approximation (i.e., $|\frac{\partial^2 \Phi_i(x,y;z)}{\partial z^2}| \ll \beta_0 |\frac{\partial \Phi_i(x,y;z)}{\partial z}|$), and replace the vector operator $\nabla^2$ by the scalar Laplacian $\nabla^2$, we obtain

$$\begin{aligned} -j\frac{\partial}{\partial z}\Phi_x = {} & \frac{1}{2n_0 k_0}\left(\frac{\partial \Phi_x}{\partial x^2} + \frac{\partial \Phi_x}{\partial y^2}\right) + \frac{k_0(n^2(x, y; z) - n_0^2)}{2n_0}\Phi_x \\ & + \frac{1}{n_0 k_0}\left(\frac{\partial^2 \ln n(x, y; z)}{\partial x^2} + \frac{\partial \ln n(x, y; z)}{\partial x}\frac{\partial}{\partial x}\right)\Phi_x \text{ for TM;} \end{aligned} \tag{4.66}$$

$$\begin{aligned} -j\frac{\partial}{\partial z}\Phi_y = {} & \frac{1}{2n_0 k_0}\left(\frac{\partial \Phi_y}{\partial x^2} + \frac{\partial \Phi_y}{\partial y^2}\right) + \frac{k_0(n^2(x, y; z) - n_0^2)}{2n_0}\Phi_y \\ & + \frac{1}{n_0 k_0}\left(\frac{\partial^2 \ln n(x, y; z)}{\partial y^2} + \frac{\partial \ln n(x, y; z)}{\partial y}\frac{\partial}{\partial y}\right)\Phi_y \text{ for TE;} \end{aligned} \tag{4.67}$$

Next if we substitute $\Phi_x = E_x \exp(-j\beta_0^{(x)} z)$ or $\Phi_y = E_y \exp(-j\beta_0^{(y)} z)$ back into Eq. (4.66) or (4.67), we obtain the following equation

$$-j\frac{\partial}{\partial z}E_i(x, y; z) = B_i(z) \cdot E_i(x, y; z), \tag{4.68}$$

where $i = y$ for the quasi-TE mode and $i = x$ for the quasi-TM mode. The propagation operator $B_i(z)$ is given by

$$B_x(z) = \frac{1}{2n_0k_0}\left(\frac{\partial}{\partial x^2} + \frac{\partial}{\partial y^2}\right) + \frac{k_0(n^2(x,y;z) + n_0^2)}{2n_0} + \frac{1}{n_0k_0}\left(\frac{\partial^2 \ln n(x,y;z)}{\partial x^2} + \frac{\partial \ln n(x,y;z)}{\partial x}\frac{\partial}{\partial x}\right) \text{ for TM;} \tag{4.69}$$

$$B_y(z) = \frac{1}{2n_0k_0}\left(\frac{\partial}{\partial x^2} + \frac{\partial}{\partial y^2}\right) + \frac{k_0(n^2(x,y;z) + n_0^2)}{2n_0} + \frac{1}{n_0k_0}\left(\frac{\partial^2 \ln n(x,y;z)}{\partial y^2} + \frac{\partial \ln n(x,y;z)}{\partial y}\frac{\partial}{\partial y}\right) \text{ for TE.} \tag{4.70}$$

In an attempt to simplify the analysis, we will neglect the vector nature of the electric field and use scalar wave equation as an approximation to vector wave equation. The propagation operator $B_i(z)$ of Eq. (4.68) can be approximated by neglecting the last two terms involving $\ln n(x,y;z)$ in Eqs. (4.69) and (4.70). The resulting propagation operator $B_i(z)$ can be expressed as

$$B_x(z) \approx \frac{1}{2n_0k_0}\left(\frac{\partial}{\partial x^2} + \frac{\partial}{\partial y^2}\right) + \frac{k_0(n^2(x,y;z) + n_0^2)}{2n_0} \text{ for TM;} \tag{4.71}$$

$$B_y(z) \approx \frac{1}{2n_0k_0}\left(\frac{\partial}{\partial x^2} + \frac{\partial}{\partial y^2}\right) + \frac{k_0(n^2(x,y;z) + n_0^2)}{2n_0} \text{ for TE.} \tag{4.72}$$

As shown in Appendix B, the operator $B_i(z)$ is Hermitian. For the sake of simplicity in exposition, we will restrict the remaining discussion to the TE-mode and will designate the operator $B_y(z)$ simply as $B(z)$. The analysis for the TM-mode is similar. The three local normal modes $\Psi_0(x,y;z)$, $\Psi_+(x,y;z)$ and $\Psi_-(x,y;z)$ of the waveguide structure shown in Figure 4.9 are eigenfunctions of Eq. (4.68), i.e.,

$$B(z)\Psi_l(x,y;z) = \beta_l(z)\Psi_l(x,y;z), \quad l = +,-,0. \tag{4.73}$$

### 4.6.2 Coupling equation of local normal modes

In the following analysis, the derivation of the coupling equation of the local normal modes will be carried out. Consider a system of three coupled waveguides with corresponding local normal modes $\Psi_0(x,y;z)$, $\Psi_+(x,y;z)$ and $\Psi_-(x,y;z)$, which are assumed to be real-valued (without loss of generality) since the operator $B_i(z)$ appearing in Eq. (4.73) is Hermitian. The local normal modes will be normalized such that

$$\begin{aligned} < \Psi_0(x,y;z)|\Psi_0(x,y;z) > &=< \Psi_+(x,y;z)|\Psi_+(x,y;z) > \\ &=< \Psi_-(x,y;z)|\Psi_-(x,y;z) > \\ &= 1, \end{aligned} \tag{4.74}$$

and the inner product $< f(x,y;z)|g(x,y;z) >$ written in bra-ket notation is defined as

$$< f(x,y;z)|g(x,y;z) >= \int_{-\infty}^{+\infty}\int_{-\infty}^{+\infty} f^*(x,y;z)g(x,y;z)\,dxdy. \tag{4.75}$$

It follows from Eq. (4.74) and the fact that $\Psi_0(x,y;z)$, $\Psi_+(x,y;z)$ and $\Psi_-(x,y;z)$ are real-valued that

$$< \Psi_l(x,y;z)|\frac{\partial}{\partial z}|\Psi_l(x,y;z) >= 0, \quad l = 0,+,-. \tag{4.76}$$

Since the operator $B(z)$ is Hermitian it also follows that the local normal modes are orthogonal, that is

$$< \Psi_l(x,y;z)|\Psi_k(x,y;z) >= 0, \quad l \neq k, \quad \{l,k\} = 0,+,-. \tag{4.77}$$

and therefore

$$< \Psi_l(x,y;z)|\frac{\partial}{\partial z}|\Psi_k(x,y;z) > = - < \Psi_k(x,y;z)|\frac{\partial}{\partial z}|\Psi_l(x,y;z) >, \qquad (4.78)$$
$$l \neq k, \;\; \{l,k\} = 0,+,-$$

Radiation modes will be neglected, and thus the total electric field, $E(x,y,z)$, in the coupled waveguides can be written as the following linear combination of the local normal modes

$$E(x,y,z) = a_0(z)\Psi_0(x,y;z) + a_+(z)\Psi_+(x,y;z) + a_-(z)\Psi_-(x,y;z). \qquad (4.79)$$

Substituting the above equation into the paraxial wave equation (4.68)

$$-j\frac{\partial}{\partial z}E(x,y,z) = B(z)E(x,y,z) \qquad (4.80)$$

yields

$$\begin{aligned}
&- j\frac{\partial a_0(z)}{\partial z}\Psi_0(x,y;z) - ja_0(z)\frac{\partial \Psi_0(z)}{\partial z} \\
&- j\frac{\partial a_+(z)}{\partial z}\Psi_+(x,y;z) - ja_+(z)\frac{\partial \Psi_+(z)}{\partial z} \\
&- j\frac{\partial a_-(z)}{\partial z}\Psi_-(x,y;z) - ja_-(z)\frac{\partial \Psi_-(z)}{\partial z} \\
&= a_0(z)B(z)\Psi_0(x,y;z) + a_+(z)B(z)\Psi_+(x,y;z) + a_-(z)B(z)\Psi_-(x,y;z) \\
&= a_0(z)\beta_0(z)\Psi_0(x,y;z) + a_+(z)\beta_+(z)\Psi_+(x,y;z) + a_-(z)\beta_-(z)\Psi_-(x,y;z) \qquad (4.81)
\end{aligned}$$

where $\beta_0(z)$, $\beta_+(z)$ and $\beta_-(z)$ are the local propagation constants associated with the local normal modes $\Psi_0(x,y;z)$, $\Psi_+(x,y;z)$ and $\Psi_-(x,y;z)$. Thus

$$B(z)\Psi_0(x,y;z) = \beta_0(z)\Psi_0(x,y;z) \tag{4.82}$$

$$B(z)\Psi_+(x,y;z) = \beta_+(z)\Psi_+(x,y;z) \tag{4.83}$$

$$B(z)\Psi_-(x,y;z) = \beta_-(z)\Psi_-(x,y;z). \tag{4.84}$$

Multiplying both sides of Eq. (4.81) by $\Psi_+(x,y;z)$, integrating over $x,y$ and using Eqs. (4.74), (4.76) and (4.77), yields

$$\begin{aligned} -j\frac{\partial a_+(z)}{\partial z} - ja_0(z) < \Psi_+(x,y;z)|\frac{\partial}{\partial z}|\Psi_0(x,y;z) > \\ - ja_-(z) < \Psi_+(x,y;z)|\frac{\partial}{\partial z}|\Psi_-(x,y;z) >= a_+(z)\beta_+(z). \end{aligned} \tag{4.85}$$

Similarly by multiplying both sides of Eq. (4.81) by $\Psi_0(x,y;z)$ or $\Psi_-(x,y;z)$ and integrating over $x,y$ yields

$$\begin{aligned} -j\frac{\partial a_0(z)}{\partial z} - ja_+(z) < \Psi_0(x,y;z)|\frac{\partial}{\partial z}|\Psi_+(x,y;z) > \\ - ja_-(z) < \Psi_0(x,y;z)|\frac{\partial}{\partial z}|\Psi_-(x,y;z) >= a_0(z)\beta_0(z). \end{aligned} \tag{4.86}$$

$$\begin{aligned} -j\frac{\partial a_-(z)}{\partial z} - ja_0(z) < \Psi_-(x,y;z)|\frac{\partial}{\partial z}|\Psi_+(x,y;z) > \\ - ja_+(z) < \Psi_-(x,y;z)|\frac{\partial}{\partial z}|\Psi_+(x,y;z) >= a_-(z)\beta_-(z). \end{aligned} \tag{4.87}$$

Equations (4.85), (4.86) and (4.87) can be written in matrix form as follows

$$-j\frac{\partial}{\partial z}\begin{pmatrix} a_0(z) \\ a_+(z) \\ a_-(z) \end{pmatrix} = \begin{pmatrix} \beta_0(z) & +j\xi_{0+}(z) & +j\xi_{0-}(z) \\ -j\xi_{0+}(z) & \beta_+(z) & +j\xi_{+-}(z) \\ -j\xi_{0-}(z) & -j\xi_{+-}(z) & \beta_-(z) \end{pmatrix} \cdot \begin{pmatrix} a_0(z) \\ a_+(z) \\ a_-(z) \end{pmatrix} \tag{4.88}$$

where

$$\xi_{lk}(z) \equiv < \Psi_l(x,y;z)|\frac{\partial}{\partial z}|\Psi_k(x,y;z) >, \quad l \neq k, \quad \{l,k\} = 0,+,-. \tag{4.89}$$

When there is no coupling (i.e., power exchange) between the local normal modes $\Psi_0(x,y;z)$, $\Psi_+(x,y;z)$ and $\Psi_-(x,y;z)$, the modes are said to evolve adiabatically. From Equation (4.88), it is clear that mode evolution will occur adiabatically when $\xi_{lk}(z) = 0, \quad l \neq k \quad \{l,k\} = 0,+,-$ for all $z$. It follows from Eq. (4.89) that mode evolution will be adiabatic when the waveguide structure is uniform or changes slowly along the propagation direction $z$ since for these cases

$$\frac{\partial}{\partial z}\Psi_l(x,y;z) = 0 \text{ or } \approx 0, \quad l = 0,+,-. \tag{4.90}$$

Equation (4.90), however, need not be satisfied for adiabatic operation, and the more general condition is given by $\xi_{lk}(z) = 0, \quad l \neq k \quad \{l,k\} = 0,+,-$. In future discussions, $\xi_{lk}(z)$ will be referred to as the nonadiabatic terms. According to the results in Section 4.3, the three local normal modes of the three waveguide structure can be written as

$$\begin{aligned}
\Psi_+(x,y;z) &= a_1^{(+)}(z)\Phi_1(x,y;z) + a_2^{(+)}(z)\Phi_2(x,y;z) + a_1^{(+)}(z)\Phi_3(x,y;z) \\
\Psi_-(x,y;z) &= a_1^{(-)}(z)\Phi_1(x,y;z) + a_2^{(-)}(z)\Phi_2(x,y;z) + a_1^{(-)}(z)\Phi_3(x,y;z) \\
\Psi_0(x,y;z) &= a_1^{(0)}(z)\Phi_1(x,y;z) - a_1^{(0)}(z)\Phi_3(x,y;z)
\end{aligned} \tag{4.91}$$

where $\Phi_l(x,y;z), \quad l = 1,2,3$ are the local normal modes of each of the three individual waveguides. Without loss of generality, the $\Phi_l(x,y;z), \quad l = 1,2,3$ will be assumed to be real-valued and normalized such that

$$< \Phi_l(x,y;z)|\Phi_l(x,y;z) >= 1, \quad l = 1,2,3. \tag{4.92}$$

It follows from Eq. (4.92) that

$$< \Phi_l(x,y;z)|\frac{\partial}{\partial z}|\Phi_l(x,y;z) >= 0, \quad l = 1,2,3. \tag{4.93}$$

Since the two outer waveguides are identical and symmetrically placed relative to the central waveguide, it also follows that

$$\begin{aligned} < \Phi_1(x,y;z)|\frac{\partial}{\partial z}|\Phi_1(x,y;z) > &=< \Phi_3(x,y;z)|\frac{\partial}{\partial z}|\Phi_3(x,y;z) > \\ < \Phi_1(x,y;z)|\frac{\partial}{\partial z}|\Phi_3(x,y;z) > &=< \Phi_3(x,y;z)|\frac{\partial}{\partial z}|\Phi_1(x,y;z) > \\ < \Phi_2(x,y;z)|\Phi_1(x,y;z) > &=< \Phi_2(x,y;z)|\Phi_3(x,y;z) > \end{aligned} \tag{4.94}$$

Combining Eqs. (4.91)- (4.94), it may be easily verified that

$$\begin{aligned} \xi_{0+}(z) &=< \Phi_0(x,y;z)|\frac{\partial}{\partial z}|\Phi_+(x,y;z) >= 0 \\ \xi_{0-}(z) &=< \Phi_0(x,y;z)|\frac{\partial}{\partial z}|\Phi_-(x,y;z) >= 0. \end{aligned} \tag{4.95}$$

Consequently,

$$-j\frac{\partial}{\partial z}\begin{pmatrix} a_0(z) \\ a_+(z) \\ a_-(z) \end{pmatrix} = \begin{pmatrix} \beta_0(z) & 0 & 0 \\ 0 & \beta_+(z) & +j\xi_{+-}(z) \\ 0 & -j\xi_{+-}(z) & \beta_-(z) \end{pmatrix} \cdot \begin{pmatrix} a_0(z) \\ a_+(z) \\ a_-(z) \end{pmatrix}. \tag{4.96}$$

Thus for adiabatic operation we need only consider the coupling between the symmetric local normal modes $\Psi_+(x,y;z)$ and $\Psi_-(x,y;z)$.

### 4.6.3 Waveguide structure and nonadiabatic term

Because the derivation of the nonadiabatic term, $\xi_{+-}(z)$, is similar for both quasi-TE and -TM modes, we now will only consider the quasi-TE mode and denote the

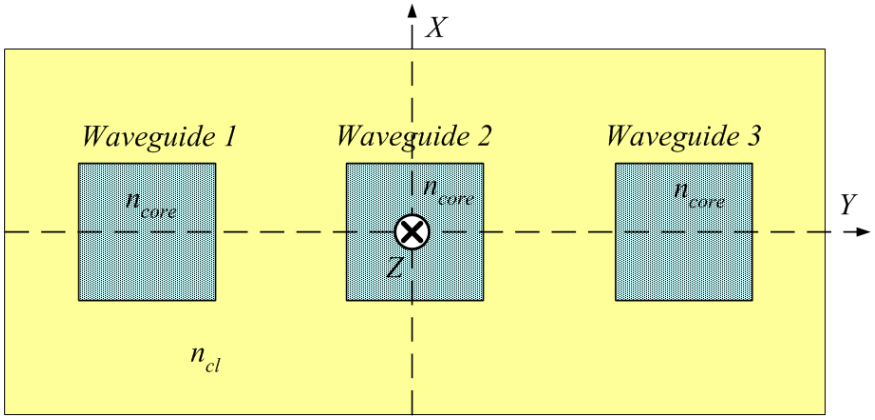


Figure 4.10: Cross-section view of the coupled two-waveguide system along with refractive index values.

corresponding operator $B(z)$ as $B_{1+2+3}(z)$, $B_{1+3}(z)$, and $B_2(z)$ for the coupled three-waveguide system, the coupled waveguide system consisting of the individual waveguides 1 and 3 alone, and the individual waveguide 2 alone, respectively, with the following distribution of dielectric constants:

$$\begin{aligned} n^2_{1+2+3}(x,y;z) =& n^2_{cl} + \Delta n^2_1(x,y;z) + \Delta n^2_2(x,y;z) \\ & + \Delta n^2_3(x,y;z) : \text{coupled three-waveguide} \end{aligned} \tag{4.97}$$

$$n^2_{1+3}(x,y;z) = n^2_{cl} + \Delta n^2_1(x,y;z) + \Delta n^2_3(x,y;z) : \text{waveguides 1 and 3} \tag{4.98}$$

$$n^2_2(x,y;z) = n^2_{cl} + \Delta n^2_2(x,y;z) : \text{waveguide 2 alone} \tag{4.99}$$

$$\Delta n^2_i(x,y;z) = n^2_{core} - n^2_{cl} : \text{inside cores } i, \text{ or 0 otherwise,} \tag{4.100}$$

where $n_{core}$ and $n_{cl}$ are the refractive indices of the waveguide cores and cladding regions, respectively. The waveguides and refractive index profiles are shown in Figure 4.10. The local normal modes of the coupled system and the constituent waveguide

modes are defined as the eigenmodes of the corresponding $B(z)$ operator.

$$B_{1+2+3}(z) \cdot \Psi_q(x,y;z) = \beta_q(z) \cdot \Psi_q(x,y;z) \tag{4.101}$$

$$B_{1+3}(z) \cdot \Psi_1(x,y;z) = \beta_{1+3}(z) \cdot \Psi_1(x,y;z) \tag{4.102}$$

$$B_2(z) \cdot \Psi_2(x,y;z) = \beta_2(z) \cdot \Psi_2(x,y;z). \tag{4.103}$$

where the index $q = \{+,-\}$ is used to distinguish the lowest $(+)$ and the other $(-)$ symmetric local normal modes of the coupled three waveguides system ($\beta_+ > \beta_-$). $\Psi_1(x,y;z)$ is the lowest order local normal mode associated with the coupled waveguide system consisting of waveguides 1 and 3 alone. $\Psi_2(x,y;z)$ is the fundamental mode associated with waveguide 2 alone. Since the $B$ operators are Hermitian as shown in Appendix B, the eigenfunctions of $B_{1+2+3}(z)$ at each fixed z (i.e. the local normal modes) are orthogonal and the corresponding eigenvalues are real-valued. Without loss of generality, the local normal modes are normalized as follows:

$$\begin{pmatrix} <\Psi_+(x,y;z)|\Psi_+(x,y;z)> & <\Psi_+(x,y;z)|\Psi_-(x,y;z)> \\ <\Psi_-(x,y;z)|\Psi_+(x,y;z)> & <\Psi_-(x,y;z)|\Psi_-(x,y;z)> \end{pmatrix} = \begin{pmatrix} 1 & 0 \\ 0 & 1 \end{pmatrix} \tag{4.104}$$

It is easily verified that $\Psi_1(x,y;z)$ and $\Psi_2(x,y;z)$ are given by

$$\Psi_1(x,y;z) = \frac{1}{\sqrt{2}}[\Phi_1(x,y;z) + \Phi_3(x,y;z)] \tag{4.105}$$

$$\Psi_2(x,y;z) = \Phi_2(x,y;z) \tag{4.106}$$

where $\Phi_1(x,y;z)$, $\Phi_2(x,y;z)$ and $\Phi_3(x,y;z)$ are the fundamental waveguide modes of the individual three waveguides. For this to be true, we are assuming weak coupling between waveguides 1 and 3. $S(z)$ is the overlap integral between $\Psi_1(x,y;z)$ and

$\Psi_2(x,y;z)$, i.e., $S(z) \equiv < \Psi_1(x,y;z)|\Psi_2(x,y;z) >$, and thus

$$\begin{aligned}
&\begin{pmatrix} < \Psi_1(x,y;z)|\Psi_1(x,y;z) > & < \Psi_1(x,y;z)|\Psi_2(x,y;z) > \\ < \Psi_2(x,y;z)|\Psi_1(x,y;z) > & < \Psi_2(x,y;z)|\Psi_2(x,y;z) > \end{pmatrix} \\
&= \begin{pmatrix} 1 & S(z) \\ S(z) & 1 \end{pmatrix}
\end{aligned} \tag{4.107}$$

When the fundamental modes of the individual waveguides are known and the coupling between the individual waveguides is not very strong, the local normal modes of the coupled system can be approximated as a linear combination of the individual waveguide modes and thus according to Eqs. (4.25) and (4.27)

$$\begin{pmatrix} \Psi_+(x,y;z) \\ \Psi_-(x,y;z) \end{pmatrix}^t = \begin{pmatrix} \Psi_1(x,y;z) \\ \Psi_2(x,y;z) \end{pmatrix}^t \cdot \begin{pmatrix} c_{1+}(z) & c_{1-}(z) \\ c_{2+}(z) & c_{2-}(z) \end{pmatrix} \tag{4.108}$$

Substituting Eq. (4.108) into the definition of the local normal modes of the coupled system, i.e., Eq. (4.101) and Eq. (4.107), we obtain the following eigenvalue equation for the coefficients $c_{iq}(z)$ as shown in Appendix C:

$$\begin{aligned}
\begin{pmatrix} B_{11}(z) & B_{12}(z) \\ B_{21}(z) & B_{22}(z) \end{pmatrix} \cdot \begin{pmatrix} c_{1+}(z) & c_{1-}(z) \\ c_{2+}(z) & c_{2-}(z) \end{pmatrix} &= \begin{pmatrix} 1 & S(z) \\ S(z) & 1 \end{pmatrix} \\
\cdot \begin{pmatrix} c_{1+}(z) & c_{1-}(z) \\ c_{2+}(z) & c_{2-}(z) \end{pmatrix} \cdot \begin{pmatrix} \beta_+(z) & 0 \\ 0 & \beta_-(z) \end{pmatrix}
\end{aligned} \tag{4.109}$$

where the matrix representation of the $B(z)$ operator of the coupled system and the

coupling coefficients between constituent waveguides are, respectively, defined as

$$\begin{pmatrix} B_{11}(z) & B_{12}(z) \\ B_{21}(z) & B_{22}(z) \end{pmatrix} = \begin{pmatrix} 1 & S(z) \\ S(z) & 1 \end{pmatrix} \cdot \begin{pmatrix} \beta_1(z) & 0 \\ 0 & \beta_2(z) \end{pmatrix} + \begin{pmatrix} \kappa_{11}(z) & \kappa_{12}(z) \\ \kappa_{21}(z) & \kappa_{22}(z) \end{pmatrix} \tag{4.110}$$

$$\kappa_{ij}(z) = \frac{k_0}{2n_0} \frac{< \Psi_i | \Delta N(3-j) | \Psi_j >}{< \Psi_j | \Psi_j >} \tag{4.111}$$

where

$$\Delta N(1) = \Delta n_1^2(x, y; z) + \Delta n_3^2(x, y; z) \tag{4.112}$$

$$\Delta N(2) = \Delta n_2^2(x, y; z) \tag{4.113}$$

By taking the inner product of Eq. (4.108) with $\Psi_q(z)(q = +, -)$ and making use of the normalization condition Eq. (4.104) and Eq. (4.107), the following additional constraint on $c_{iq}(z)$ is obtained

$$\begin{pmatrix} c_{1+}(z) & c_{1-}(z) \\ c_{2+}(z) & c_{2-}(z) \end{pmatrix}^t \begin{pmatrix} 1 & S(z) \\ S(z) & 1 \end{pmatrix} \begin{pmatrix} c_{1+}(z) & c_{1-}(z) \\ c_{2+}(z) & c_{2-}(z) \end{pmatrix} = \begin{pmatrix} 1 & 0 \\ 0 & 1 \end{pmatrix} \tag{4.114}$$

The solution of the simultaneous equations (4.109) and (4.114) can be obtained using the method developed by Haus et al. [79] and further expanded upon by Ishikawa [3] as shown in Appendix D. Weak coupling will be assumed, so that $|S(z)| \ll 1$. It will also be assumed that $\left|\frac{\kappa_{12}-\kappa_{21}}{\kappa_{12}}\right| \ll 1$ and $\left|\frac{\beta_1-\beta_2}{\beta_2}\right| \ll 1$. If we introduce new parameters

$\theta(z)$ and $\phi(z)$ as

$$\tan\theta(z) = \frac{\kappa'_{12}(z)}{\delta'_{12}(z)} \tag{4.115}$$

$$\tan\phi(z) = \frac{S(z)}{\sqrt{1-S(z)^2}} \tag{4.116}$$

where

$$\delta'_{12}(z) = \frac{\beta_1 + \kappa_{11} - (\beta_2 + \kappa_{22})}{2\sqrt{1-S^2}} \tag{4.117}$$

$$\kappa'_{12}(z) = \frac{\kappa_{12} + \kappa_{21}}{2(1-S^2)} - \frac{S}{1-S^2}\frac{\kappa_{11} + \kappa_{22}}{2}, \tag{4.118}$$

the solution of Eqs. (4.109) and (4.114) can be expressed as

$$\begin{pmatrix} c_{1+}(z) & c_{1-}(z) \\ c_{2+}(z) & c_{2-}(z) \end{pmatrix} = \frac{1}{\cos\phi(z)} \begin{pmatrix} \cos\frac{\theta(z)+\phi(z)}{2} & -\sin\frac{\theta(z)+\phi(z)}{2} \\ \sin\frac{\theta(z)-\phi(z)}{2} & \cos\frac{\theta(z)-\phi(z)}{2} \end{pmatrix} \tag{4.119}$$

$$\beta_\pm(z) = \bar{\beta}(z) \pm \sqrt{\delta'_{12}(z)^2 + \kappa'_{12}(z)^2} \tag{4.120}$$

where

$$\bar{\beta}(z) = \frac{\beta_1 + \kappa_{11} + \beta_2 + \kappa_{22}}{2(1-S^2)} - \frac{S}{2(1-S^2)}(\kappa_{12} + \kappa_{21} + S\beta_1 + S\beta_2). \tag{4.121}$$

Using Eqs. (4.108) and (4.119), the nonadiabatic term, $\xi_{+-}(z) = < \Psi_+ | \frac{\partial}{\partial z} | \Psi_- >$, can be expressed as follows according to Appendix E:

$$\begin{aligned} \xi_{+-}(z) = &-\frac{1}{2}\frac{\partial\theta(z)}{\partial z} - \frac{\cos\theta(z)}{2\cos\phi(z)}\frac{\partial\phi(z)}{\partial z} \\ &- \frac{1}{\cos\phi(z)} < \Psi_2(x,y;z) | \frac{\partial}{\partial z} | \Psi_1(x,y;z) > . \end{aligned} \tag{4.122}$$

The nonadiabatic term is now expressed as a derivative of local waveguide parameters, which allows us to minimize the nonadiabatic term and design a nearly adiabatic

device. If the center waveguide is chosen to be uniform along its length, then

$$\frac{\partial}{\partial z}\Psi_2(x,y;z) = 0 \tag{4.123}$$

and thus (since $< \Psi_2|\frac{\partial}{\partial z}|\Psi_1 >= - < \Psi_1|\frac{\partial}{\partial z}|\Psi_2 >$) the last term in Eq. (4.122) vanishes.

## 4.7 Numercial simulation of achromatic beam combiner

In practice, the fully adiabatic transition cannot be achieved. Therefore, there will be some power exchange between the local normal modes $\Psi_+(x,y;z)$ and $\Psi_-(x,y;z)$ as they propagate down the structure. This power coupling, however, can be minimized by careful waveguide design. The design process will be illustrated in this section by considering a germanium/silicon raised strip three coupled waveguide system. Equation (4.122) will be used to estimate the magnitude of the nonadiabatic term at each $z$ for the design example. The power that couples from local normal mode $\Psi_+(x,y;z)$ to $\Psi_-(x,y;z)$, as the local normal mode propagates from the beginning (i.e., $z = 0$) to the end (i.e., $z = L$) of the device, will be determined by solving Eq. (4.96) numerically.

### 4.7.1 Candidates of waveguide fabrication in mid-infrared region

Both chalcogenide elements [80, 81] and group IV elements, especially silicon and germanium [82], have been studied as candidate materials for mid-IR waveguides. There are several promising substrate materials and fabrication methods for realizing mid-infrared waveguide circuits. The most promising candidates include:

1. chalcogenide rib waveguides on chalcogenide substrates

2. chalcogenide rib waveguides on silicon substrates

3. silicon or germanium rib waveguide membranes with an air bridge underneath the rib to serve as a lower cladding layer

4. Ge/Si heterostructure rib waveguides with the Ge rib on top of a Si substrate

5. hollow air core ARROW waveguides with a SiGe/Si antiresonant cladding

Channel waveguides have been fabricated and their losses measured in the mid-infrared (8.4 $\mu$m) using the first of these technologies in 2006 [80]. Waveguides fabricated using the second technology were demonstrated, but loss values were only reported in the near-IR around 1.5 $\mu$m [81]. Finally, technologies 3 – 5 have been theoretically investigated [82].

The widespread use of silicon-based electronics, especially Si-CMOS technology, has become a major driving force beyond the development of silicon photonics [83]. The ability to integrate both electronic and photonic capabilities onto a single silicon platform is one of the holy grails of optoelectronics. In 1985, Soref and Lorenzo [84] were the first to demonstrate an all silicon integrated optical component, specifically, an optical power divider. In 1987 Soref et al. analyzed the use of carrier injection to electro-optically modulate light in silicon waveguides via the free carrier plasma dispersion effect [85]. Up until 2004, only passive silicon photonic devices had been demonstrated. In 2004, however, the carrier dispersion effect was used to demonstrate optical switching and modulation speeds approaching 20 Gbit/s have now been achieved [86]. Raman-based waveguide lasers have also been reported [86], as well as gigahertz-speed optical detectors (GeSi), and silicon-based ridge waveguides with propagation losses on the order of 0.3 dB/cm at 1.55 $\mu$m [86]. The successful developments of these devices have aroused interests in deploying silicon for mid-infrared applications [82]. Silicon has low loss in the spectral bands 1.2 $\mu$m – 6 $\mu$m and 24 $\mu$m – 100 $\mu$m, while multiphonon absorption prevents its use between 6 $\mu$m and 24 $\mu$m. EO modulation using the free carrier plasma effect becomes more efficient at

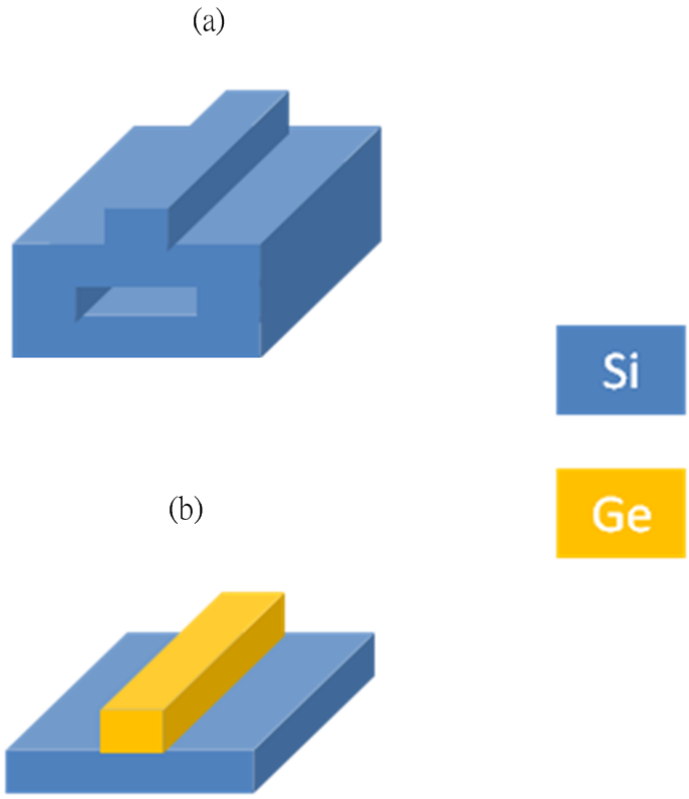


Figure 4.11: Proposed candidates for mid-infrared waveguide fabrication: (a) silicon rib membrane waveguide (b) Ge/Si heterostructure raised strip waveguide.

wavelength beyond near IR, thus enhancing the functionality of silicon optical circuits in the mid-infrared regions. Traditional substrate cladding materials, such as $SiO_2$, which are suitable at near-IR are too lossy to be used for device operation beyond approximately 2 $\mu$m. Suspended rib waveguides, as shown in Figure 4.11(a), consisting of silicon membrane clad below and above by air have been proposed as a potential solution [82]. Another promising approach is to use a Ge/Si heterostructure consisting of a Ge raised strip waveguide of strain-relaxed crystal Ge epitaxially grown upon a silicon substrate as shown in Figure 4.11(b) [82]. Crystalline Ge has low loss from 1.9 $\mu$m out to approximately 12.5 $\mu$m. The high refractive index difference between

Ge and Si may permit Si to be used as the lower cladding level even though it is lossy in the 6 $\mu$m – 12 $\mu$m band, since the optical field barely penetrates the cladding.

We will choose the Ge/Si heterostructure raised strip waveguide as the waveguide fabrication technique for our design example because of its transparency in the band of interest, i.e., the astronomical N band (8 $\mu$m – 12 $\mu$m). The other attractive reason for this waveguide technology is that the heteroepitaxial growth of multiple microns of high quality germanium film on silicon by multiple steps of growth and hydrogen annealing has been successfully demonstrated [87]. The practical fabrication of the proposed device seems promising.

### 4.7.2 Numerical design and calculation results

The schematic plot of the achromatic mode-evolution beam combiner and the equivalent two-waveguide system is shown in Figure 4.12 along with cross-section of the waveguide geometry based on Ge/Si raised strip waveguide. The refractive indices of the germanium strip and silicon substrate in the N band are taken from reference [88] and are summarized in Table 4.2.

| Temperature | $\lambda(\mu m)$ | $n$(Si) | $n$(Ge) |
|---|---|---|---|
| $20^o$C | 8 | 3.4158 | 4.0048 |
| | 10 | 3.415 | 4.0025 |
| | 12 | 3.4145 | 4.0012 |

Table 4.2: Dispersion of Si and Ge at $20^o$C and different mid-infrared wavelengths.

Due to relatively large refractive index difference between germanium and silicon, the optical mode of Ge/Si raised strip waveguide is well confined inside germanium strip. Thus, the results obtained for the buried waveguide as described in previous sections can be similarly applied to the waveguide geometry based on Ge/Si raised strip waveguide. Using the 3D structure together with a commercial, semi-vectorial 3D mode solver (RSoft BeamPROP), the waveguide parameters that correspond to

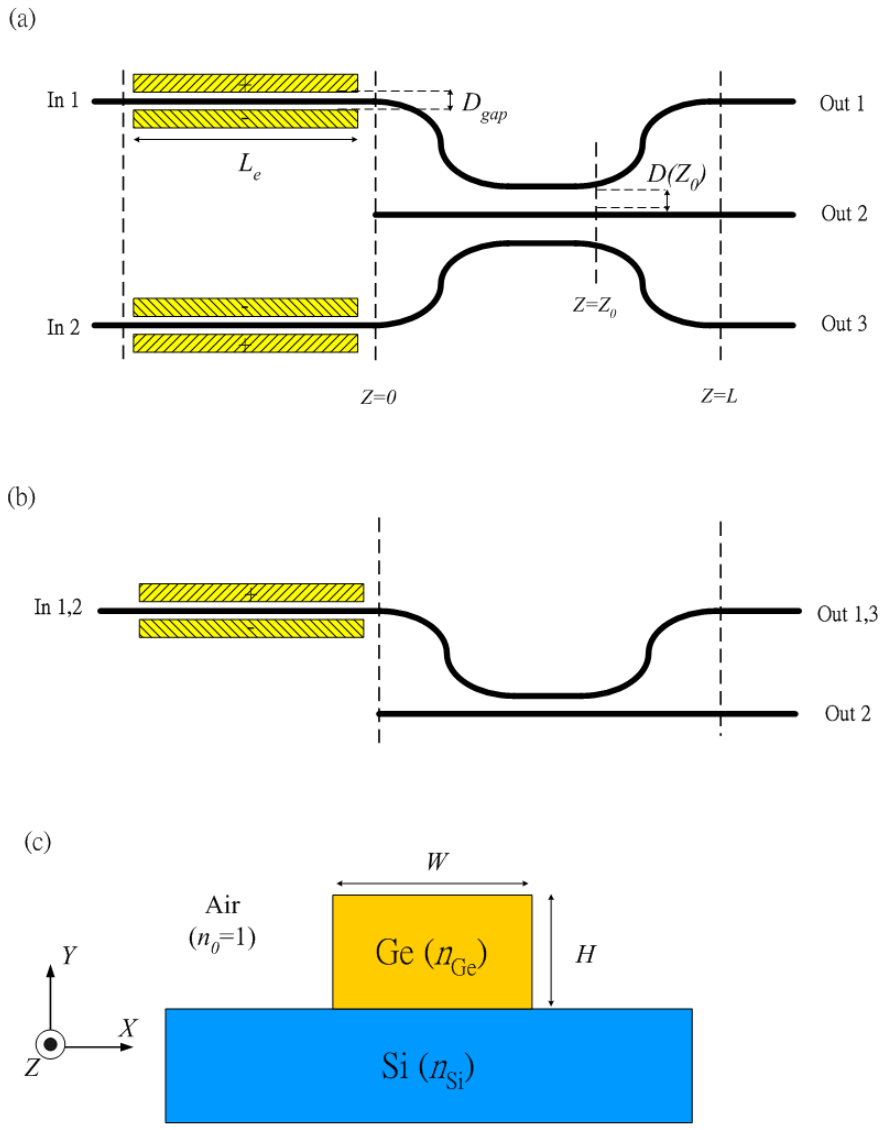


Figure 4.12: (a) Schematic of broadband achromatic beam combiner with on-chip EO modulation (b) Equivalent two-waveguide coupler for local normal mode coupling analysis of $\Psi_+(x, y; z)$ and $\Psi_-(x, y; z)$ (c) Cross-section of Ge/Si raised strip waveguide geometry for fundamental mode calculation by beam propagation method.

single-mode operation in the N band at a nominal wavelength of $\lambda_0 = 10$ $\mu$m for both TE and TM modes are determined. The Ge strip height $H$ is chosen to be 3.5 $\mu$m and the strip width $W$ for the center waveguide is fixed to be 3.5 $\mu$m as well, while the widths of the outer waveguides shown in Figure 4.12(a) are varied from 3.58 $\mu$m at $z = 0$ to 3.42 $\mu$m at $z = L$. Since the central waveguide is uniform with width $W$ = 3.5 $\mu$m, the last term of Eq. (4.122) vanishes, and thus the nonadiabatic term is reduced to

$$\xi_{+-}(z) = -\frac{1}{2}\frac{\partial\theta(z)}{\partial z} - \frac{\cos\theta(z)}{2\cos\phi(z)}\frac{\partial\phi(z)}{\partial z}. \tag{4.124}$$

Under weak coupling condition, $S(z) \approx 0$, and thus $\phi(z) \approx 0$ according to Eq. (4.116). Therefore $\xi_{+-}(z)$ is approximately given by

$$\xi_{+-}(z) \approx -\frac{1}{2}\frac{\partial\theta(z)}{\partial z}. \tag{4.125}$$

Thus, nearly adiabatic operation of the device can be achieved by minimizing $\frac{\partial\theta(z)}{\partial z}$, where (see Eq. (4.115))

$$\tan\theta(z) = \frac{\kappa'_{12}(z)}{\delta'_{12}(z)} \tag{4.126}$$

and (see Eqs. (4.117) and (4.118))

$$\delta'_{12}(z) \approx \frac{\beta_1(z) + \kappa_{11}(z) - (\beta_2(z) + \kappa_{22}(z))}{2} \tag{4.127}$$

$$\kappa'_{12}(z) \approx \frac{\kappa_{12}(z) + \kappa_{21}(z)}{2} \tag{4.128}$$

If the outer waveguides are identical to the center waveguide and uniform along the direction of propagation, it can be easily verified that

$$\kappa_{11}(z) = \kappa_{22}(z) \tag{4.129}$$

$$\kappa_{12}(z) = \kappa_{21}(z) \tag{4.130}$$

according to Eqs. (4.111) - (4.113). Thus if the variation of the width of the outer waveguides is much smaller than their nominal widths and the gap between the outer and the center waveguides, then the following relations approximately hold

$$\kappa_{11}(z) \approx \kappa_{22}(z) \tag{4.131}$$

$$\kappa_{12}(z) \approx \kappa_{21}(z) \tag{4.132}$$

Therefore, Eqs. (4.127) and (4.128) can be approximately written as

$$\delta'_{12}(z) \approx \frac{\beta_1(z) - \beta_2(z)}{2} = \frac{\Delta\beta(z)}{2} \tag{4.133}$$

$$\kappa'_{12}(z) \approx \kappa_{12}(z) \tag{4.134}$$

A three waveguide beam combiner is designed that achieves nearly adiabatic, achromatic operation for the TE mode at a center wavelength of $\lambda_0 = 10$ $\mu$m. The waveguide parameters (i.e., $\Delta\beta(z)$ and $\kappa_{12}(z)$) from $z = 0$ to $z = L$ are varied according to Table 4.1 such that $\frac{\partial\theta(z)}{\partial z}$ is small along the length of the device to achieve desired operation. The device's operation at 8 $\mu$m and 12 $\mu$m is also numerically evaluated.

The fundamental TE and TM modes profiles for $H = W = 3.5$ $\mu$m, and $\lambda_0 = 10$ $\mu$m are shown in Figure 4.13. The effective refractive index, $n_{eff}$, of TE and TM modes are 3.6017 and 3.6454, respectively. The mode profiles are used to compute the coupling coefficient, $\kappa_{12}$, at different center-to-center gap spacings between outer and center waveguides and the results are fitted and shown in Figure 4.14 for both TE and

TM polarizations. The dephasing term, $\Delta\beta = \frac{2\pi}{\lambda_0}(n_{eff_2} - n_{eff_1})$, is also computed and shown in Figure 4.15 as a function of the width of the outer waveguides. Although not shown here, the coupling coefficients and the dephasing terms at 8 $\mu$m and 12 $\mu$m wavelengths have also been computed for the purpose of device verification at other wavelengths in the N band. The coupling coefficient $\kappa_{12}(z)$ between the outer waveguides and the center waveguide is restricted to positive values, while the dephasing term $\Delta\beta(z) = \beta_2 - \beta_1$ can be either positive, 0 or negative. In order to estimate the power transferred from the $\Psi_+(x, y; z)$ to the $\Psi_-(x, y; z)$ local normal mode, we use the equivalent two-waveguide system described by Eq. (4.12) in Section 4.3. Recall (see Eq. (4.13)) that

$$\begin{aligned} a(z) &= a_2(z) \\ b(z) &= \sqrt{2}a_1(z) = \sqrt{2}a_3(z) \end{aligned} \tag{4.135}$$

where $a_1(z)$, $a_2(z)$, and $a_3(z)$ are the modal amplitude of each individual waveguide, and $a(z)$ and $b(z)$ are the equivalent modal amplitudes of the straight and curved waveguides as shown in Figure 4.12(a) and (b), respectively. The coupling coefficient $K(z)$ between the two waveguides in the two-waveguide system is related to the coupling coefficient $\kappa_{12}(z)$ between the outer and center waveguides of the three-waveguide system by $K(z) = \sqrt{2}\kappa_{12}$ (see Eq. (4.14)). As indicated earlier the design approach which will be taken is to vary $\Delta\beta(z)$ and $\kappa_{12}(z)$ along the length of the device in a manner consistent with Table 4.1 and in such a way that $\frac{\partial\theta}{\partial z} \approx 0$, where $\tan\theta(z) \equiv \frac{2\kappa_{12}(z)}{\Delta\beta(z)}$. Such a design can be realized by choosing

$$K(z) = K_{max} \sin\vartheta(z) \tag{4.136}$$

$$\Delta\beta(z) = -\Delta\beta_{max} \cos\vartheta(z) \tag{4.137}$$

where $K_{max}$ is the maximum coupling coefficient (which occurs at the device center

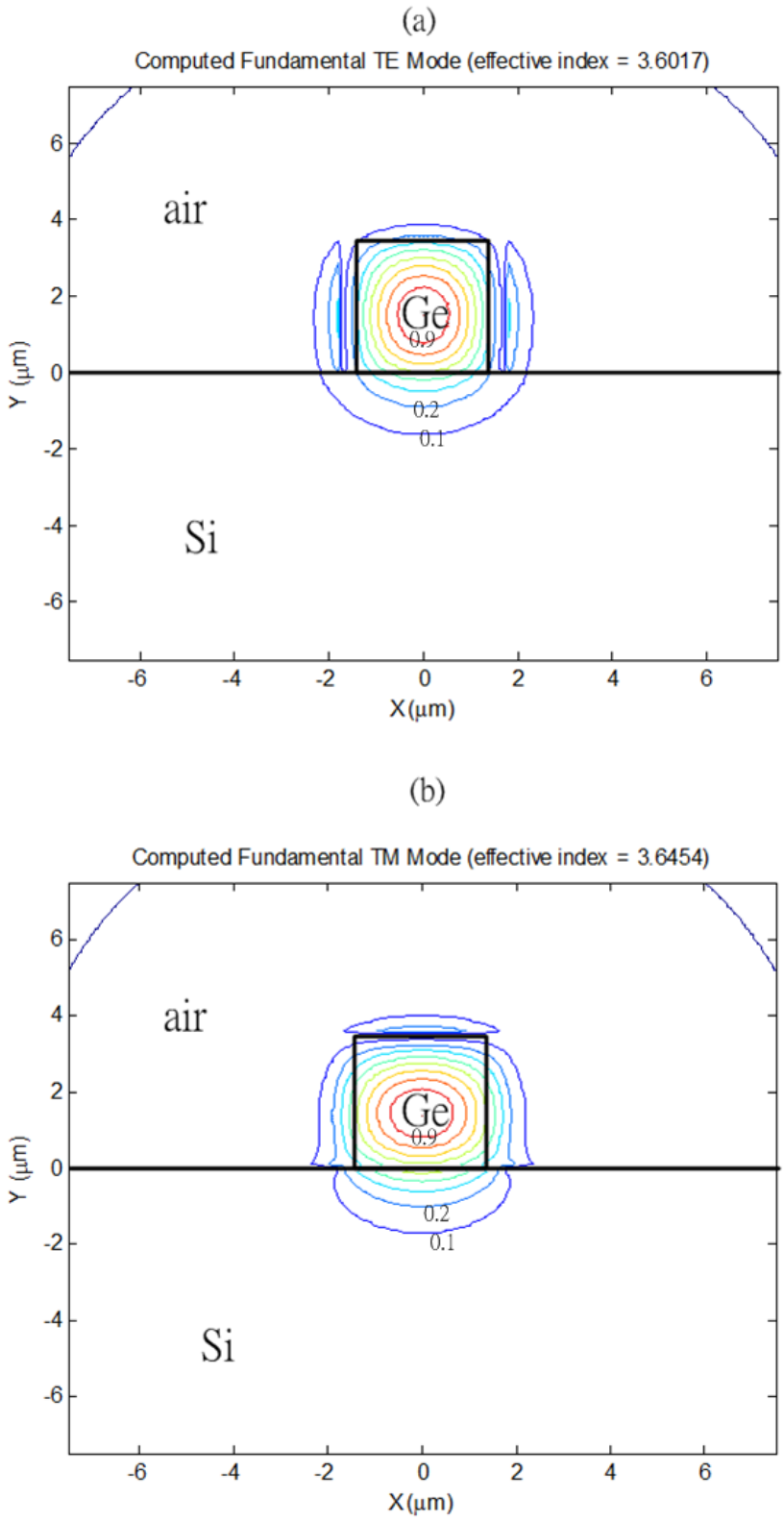


Figure 4.13: (a) TE mode profile at $\lambda_0 = 10$ $\mu$m, $n_{eff} = 3.6017$ (b) TM mode profile at $\lambda_0 = 10$ $\mu$m, $n_{eff} = 3.6454$ with nominal design ($H = W = 3.5$ $\mu$m).

(a)

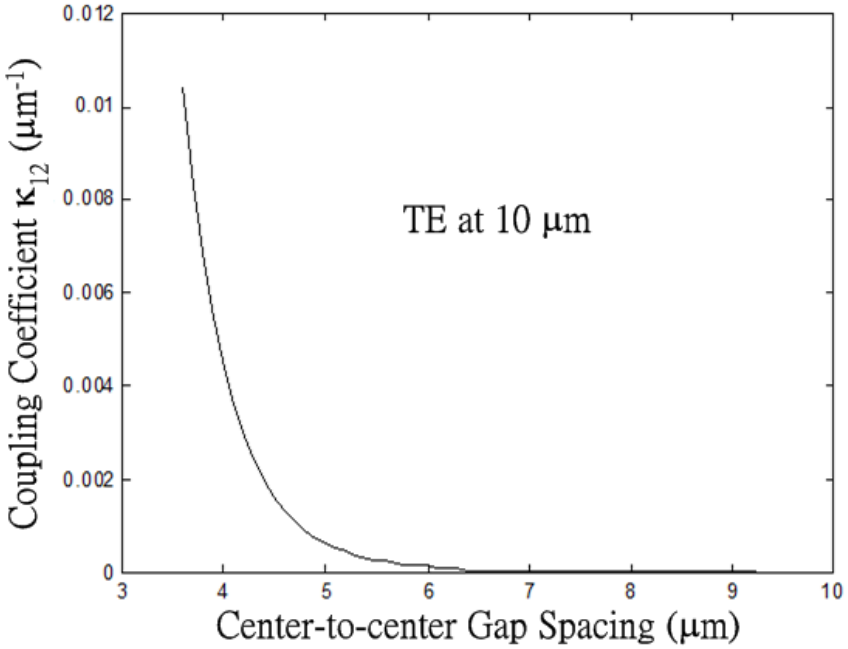


(b)

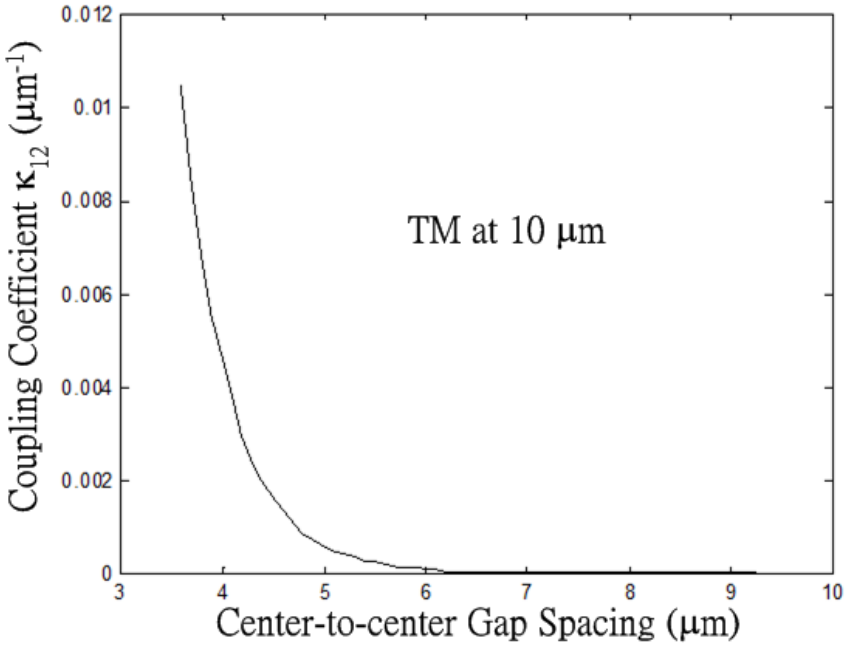


Figure 4.14: Coupling coefficient $\kappa_{12}$ with nominal design ($H = W = 3.5$ $\mu$m) for (a) TE mode (b) for TM mode at $\lambda_0 = 10$ $\mu$m.

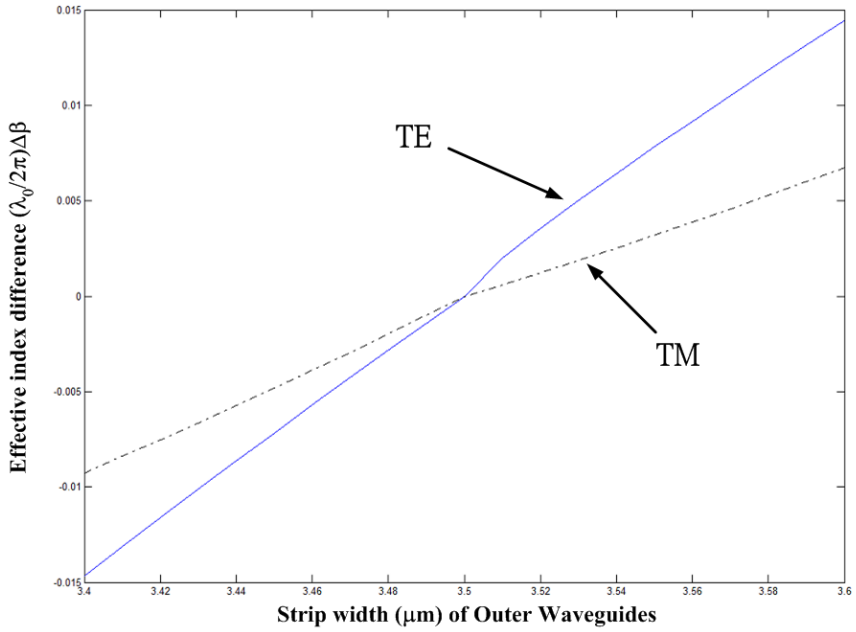


Figure 4.15: Plot of effective index difference, $\frac{\lambda_0}{2\pi}\Delta\beta$, as a function of the strip width of the outer waveguides. The width of the center waveguide is 3.5 $\mu$m.

$z = L/2$), $\Delta\beta_{max}$ is the maximum dephasing term (which occurs at the beginning and the end of the device, i.e., at $z = 0$ and $L$), and $\vartheta(z)$ is a monotonically (or nearly monotonically) increasing function of $z$, with $\vartheta(0) = 0$ and $\vartheta(L) = \pi$, that controls the rate of change of $\Delta\beta(z)$ and $\kappa_{12}(z)$. The waveguide parameter $X(z)$ given by Eq. (4.20) is equal to $\frac{\Delta\beta(z)}{2K(z)}$. The nonadiabatic term according to Eq. (4.125) can be written as

$$\xi_{+-}(z) \approx -\frac{1}{2}\frac{\partial\theta(z)}{\partial z} \tag{4.138}$$

where $\tan\theta(z) \approx 1/X(z)$. Therefore, the nonadiabatic term can be expressed in terms of the variation of the waveguide parameter, $X(z)$, as follows

$$\xi_{+-}(z) \approx \frac{1}{2(1+X^2)}\frac{\partial X}{\partial z} \tag{4.139}$$

The coupling between the local normal modes $\Psi_+(z)$ and $\Psi_-(z)$ for the TE mode at

$\lambda_0 = 10$ $\mu$m is computed with the nonadiabatic term described in Eq. (4.139) for the different $\vartheta(z)$ functions listed below [89]:

$$\vartheta(z) = \frac{\pi z}{L} : \text{Linear Function} \tag{4.140}$$

$$\vartheta(z) = \frac{\pi z}{L} - 0.5 \sin \frac{2\pi z}{L} : \text{Raised Cosine Function} \tag{4.141}$$

$$\vartheta(z) = \frac{\pi z}{L} - 0.426 \sin \frac{2\pi z}{L} : \text{Hamming Function} \tag{4.142}$$

$$\vartheta(z) = \frac{\pi z}{L} - 0.5952 \sin \frac{2\pi z}{L} + 0.0476 \sin \frac{4\pi z}{L} : \text{Blackman Function} \tag{4.143}$$

The maximum coupling coefficient, $K_{max}$, and the maximum dephasing term, $\Delta\beta_{max}$, are chosen to be 0.0068 $\mu\text{m}^{-1}$ and 0.012 $\mu\text{m}^{-1}$, respectively. These values are selected such that the single mode condition for each individual waveguide and the weak coupling condition between outer and center waveguides are maintained at wavelengths from 8 $\mu$m to 12 $\mu$m, as the waveguide parameters from $z = 0$ to $z = L$ are varied according to Table 4.1. The fraction of power transferred (i.e., $-10 \log_{10} |a_-(L)|^2$) from the $\Psi_+(x, y; z)$ local normal mode to the $\Psi_-(x, y; z)$ local normal mode is numerically computed using Eq. (4.96) with $a_+(0) = 1$ and $a_-(0) = 0$. The result is shown for $L$ between 0 and 10000 $\mu$m for the various $\vartheta(z)$ functions and plotted in Figure 4.16. Among different $\vartheta(z)$ functions, for $L > 3000$ $\mu$m, the Raised Cosine and the Blackman functions outperform (i.e., smaller fractional power transferred from $\Psi_+(x, y; z)$ to $\Psi_-(x, y; z)$) the others and the Blackman function is slightly better than the Raised Cosine function. Based on this observation, we choose $L = 6000$ $\mu$m for our device. Better performance can always be achieved by using a longer value of $L$. For the Blackman function and $L = 6000$ $\mu$m, the variation of the coupling term, $\kappa_{12}(z)$, and the dephasing term, $\Delta\beta(z)$, along with the corresponding nonadiabatic term, $\xi_{+-}(z)$, are shown in Figure 4.17, and the power transfer characteristics between the local normal modes along the propagation direction $z$ is shown in Figure 4.18.

Using the data presented in Figure 4.14 together with Eqs. (4.136), (4.137), and

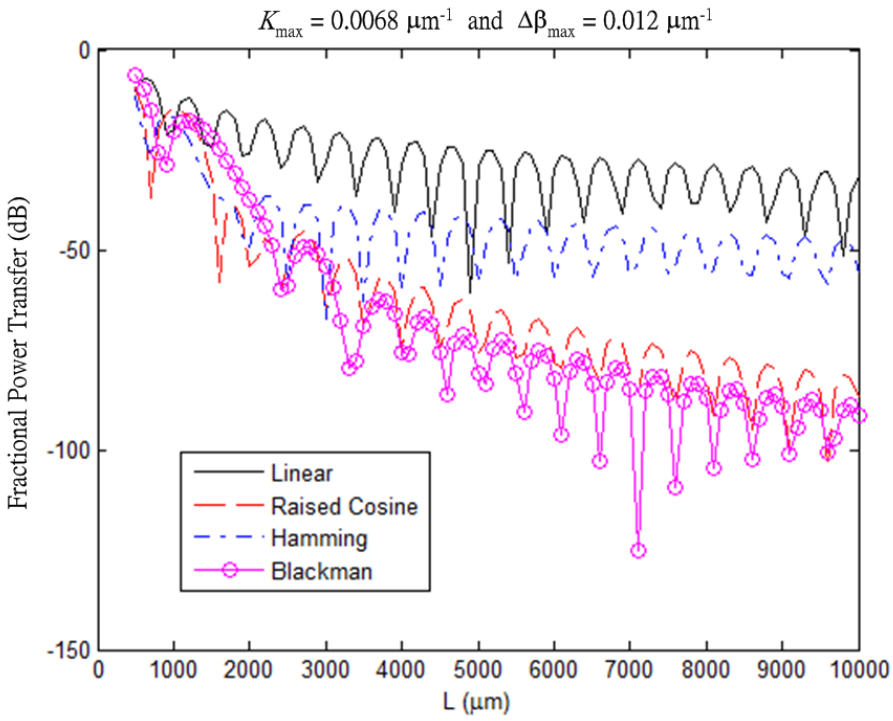


Figure 4.16: Power transferred to the TE local normal mode $\Psi_{-}(x, y; z)$ at $\lambda_0 = 10$ $\mu$m.

(4.143) with $K_{max} = 0.0068$ $\mu$m$^{-1}$, $\Delta\beta_{max} = 0.012$ $\mu$m$^{-1}$, $L = 6000$ $\mu$m, and $\lambda_0 = 10$ $\mu$m, the device layout is obtained. The width variation of the outer waveguides and the separation between the outer and center waveguides, as a function of the position $z$ along the device, are plotted in Figure 4.19 and 4.20, respectively.

The performance of the device design is also numerically evaluated using Eq. (4.96) at wavelengths of 8 $\mu$m and 12 $\mu$m and is summarized in Table 4.3.

| Wavelength | Residual Fraction of Power in $\Psi_{-}$ TE Mode | Residual Fraction of Power in $\Psi_{-}$ TM Mode |
|---|---|---|
| 8 $\mu$m | -34 dB | -24.1 dB |
| 10 $\mu$m | -82.2 dB | -39.5 dB |
| 12 $\mu$m | -33.4 dB | -40.6 dB |

Table 4.3: The residual power in $\Psi_{-}$ mode at other wavelengths for TE and TM polarizations at $z = 6000$ $\mu$m.

Based on this data, it is seen that the performance of our mode-evolution beam com-

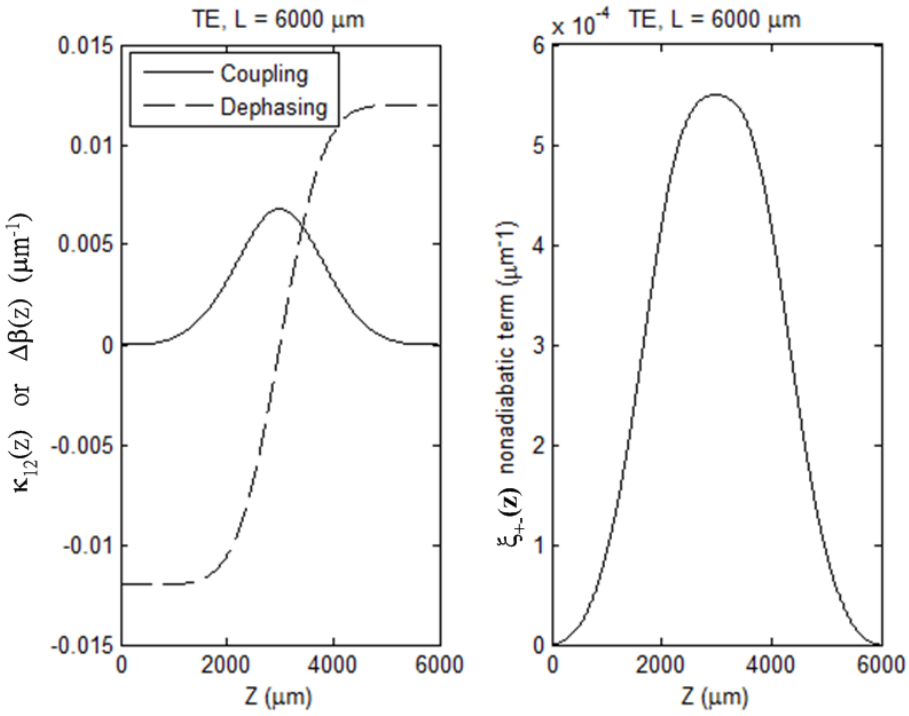


Figure 4.17: (Left) The variation of the coupling coefficient, $\kappa_{12}(z)$, and the dephasing term, $\Delta\beta(z)$, along propagation direction $z$ (Right) The nonadiabatic term, $\xi_{+-}(z)$, for the Blackman function for the TE mode at $\lambda_0 = 10$ $\mu$m.

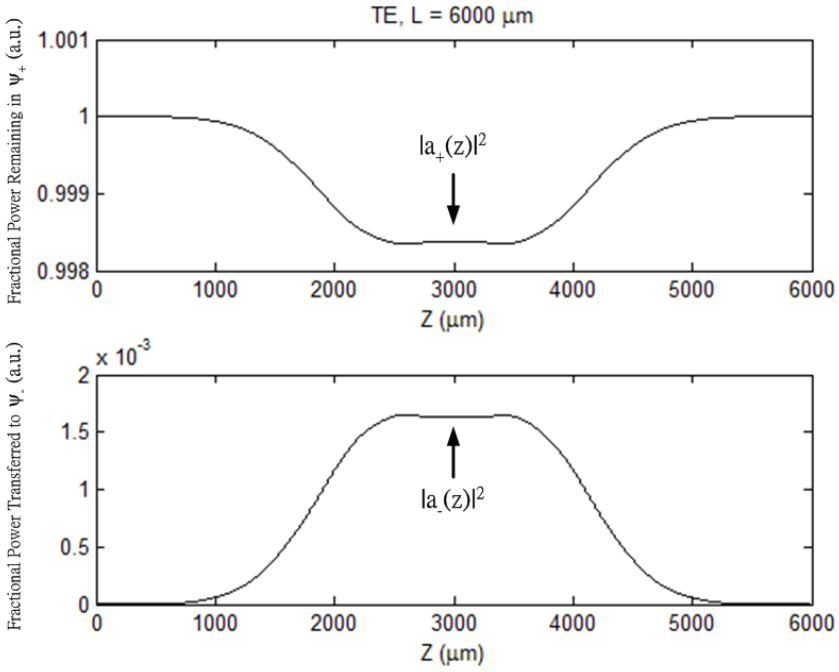


Figure 4.18: (Top) Total fraction of power remaining when only the local normal mode $\Psi_+$ is excited at $z = 0$, i.e., $a_+(0) = 1$ and $a_-(0) = 0$. (Bottom) Fraction of launched power in $\Psi_+$ mode ($a_+(0) = 1$ and $a_-(0) = 0$) transferred to the local normal mode $\Psi_-$.

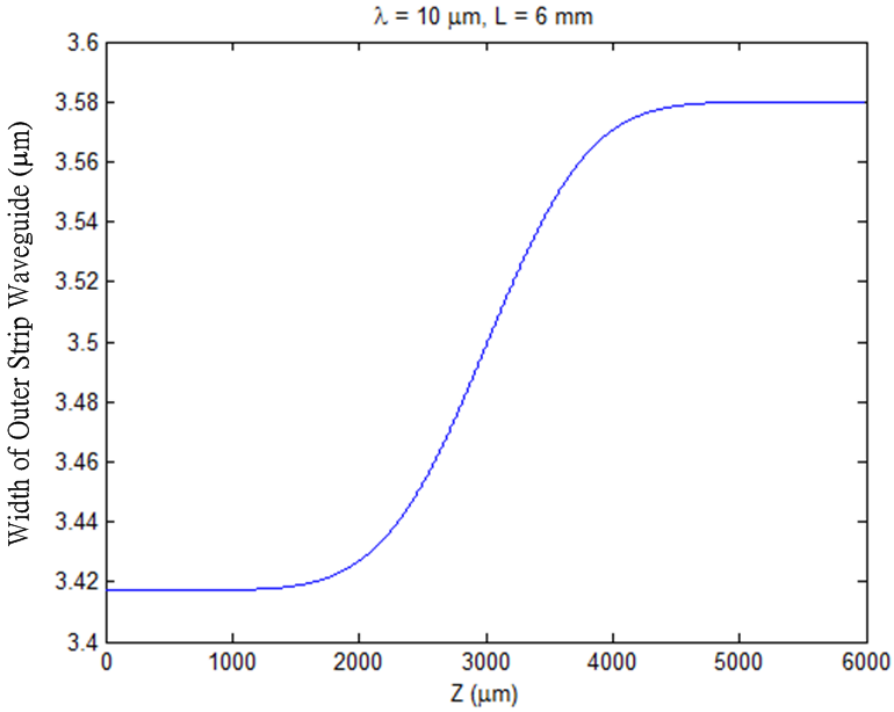


Figure 4.19: The width variation of the outer waveguides as a function of propagation distance.

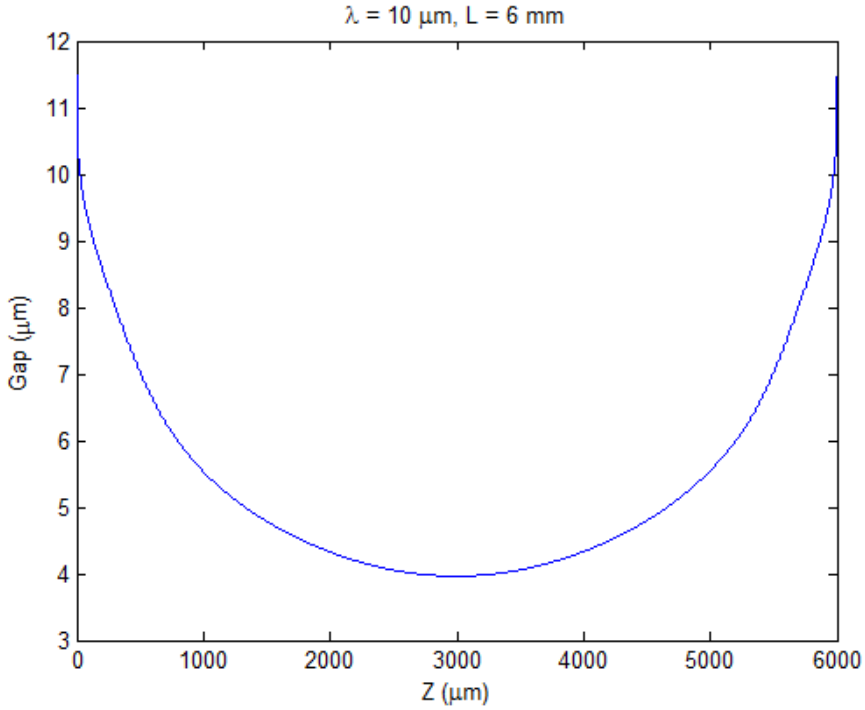


Figure 4.20: The gap variation between the outer and the central waveguides as a function of propagation distance.

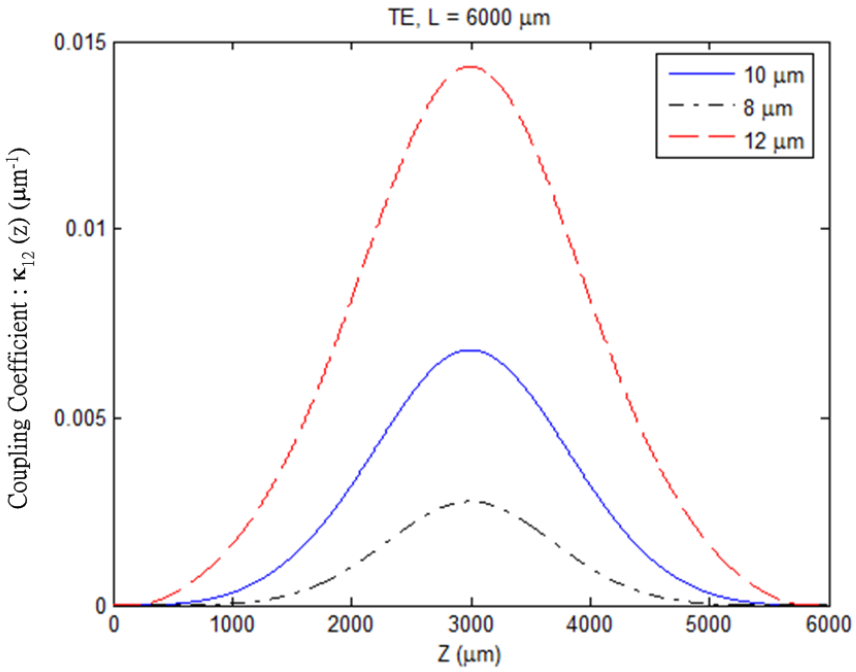


Figure 4.21: The coupling coefficients along propagation direction $z$ for different wavelengths

biner is relatively insensitive to the operating wavelength and the polarization, even though the coupling coefficient, $\kappa_{12}(z)$, and the dephasing term, $\Delta\beta(z)$, are highly wavelength-dependent as shown in Figure 4.21 and 4.22. The coupling coefficient, $\kappa_{12}(z)$, and the dephasing term, $\Delta\beta(z)$, are computed based on the waveguide geometry shown in Figure 4.19 and 4.20.

The design parameters are converted to the equivalent two-waveguide system and the device operation is verified by the beam propagation method as shown in Figure 4.23. The input excitation at a wavelength of $\lambda_0 = 10$ $\mu$m is launched into the curved waveguide, which represents the in-phase, equal amplitude input excitations to the outer waveguides 1 and 3 of the coupled three-waveguide system. Thus the local normal mode $\Psi_+(0)$ is excited. Except for the abrupt power drop at the interface between the straight input section and the curved beam combiner section, all the power is transferred nearly 100 % to the other straight waveguide in the end of simulation. The residual fraction power transferred from $\Psi_+$ local normal mode to $\Psi_-$

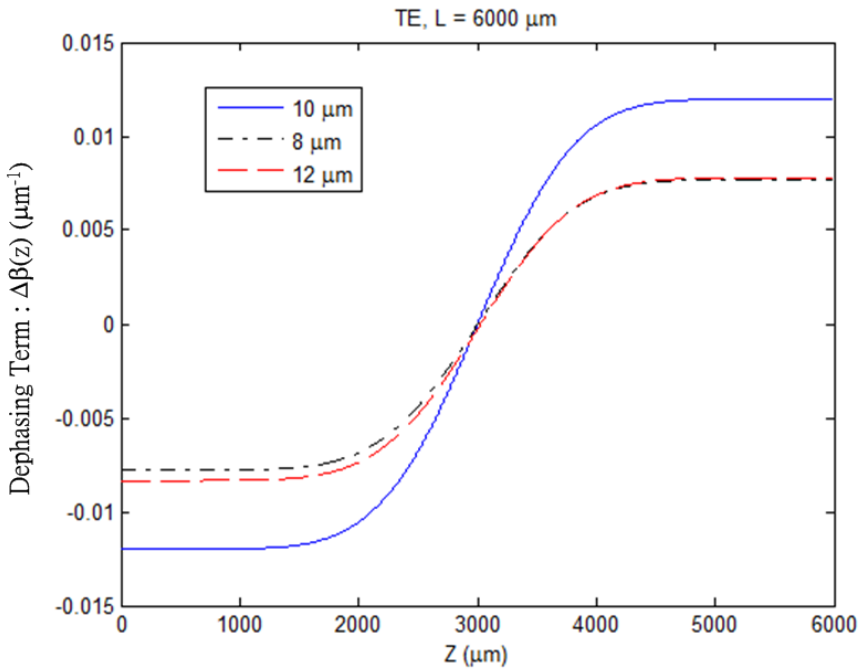


Figure 4.22: The dephasing term along propagation direction $z$ for different wavelengths

local normal mode is numerically determined to be approximately -30 dB. It is clear that the excited local normal mode $\Psi_+(0)$ has already adiabatically mode-evolved to the desired local normal mode $\Psi_+(L)$ at the output with negligible power coupling to $\Psi_-$ local normal mode.

## 4.8 Discussion

We have presented the numerical design of a broadband, polarization insensitive, achromatic beam combiner for the operation in the astronomical N band based on Ge/Si heterostructure raised strip waveguides. The beam combining is intrinsically achromatic because of the symmetric arrangement of the three coupled waveguides. As opposed to a reversed-Y junction combiner which suffers a 3 dB loss, our device is theoretically lossless. Furthermore on-chip EO modulation is also possible by utilizing the free carrier plasma dispersion effect [85] in silicon-based waveguides. Most

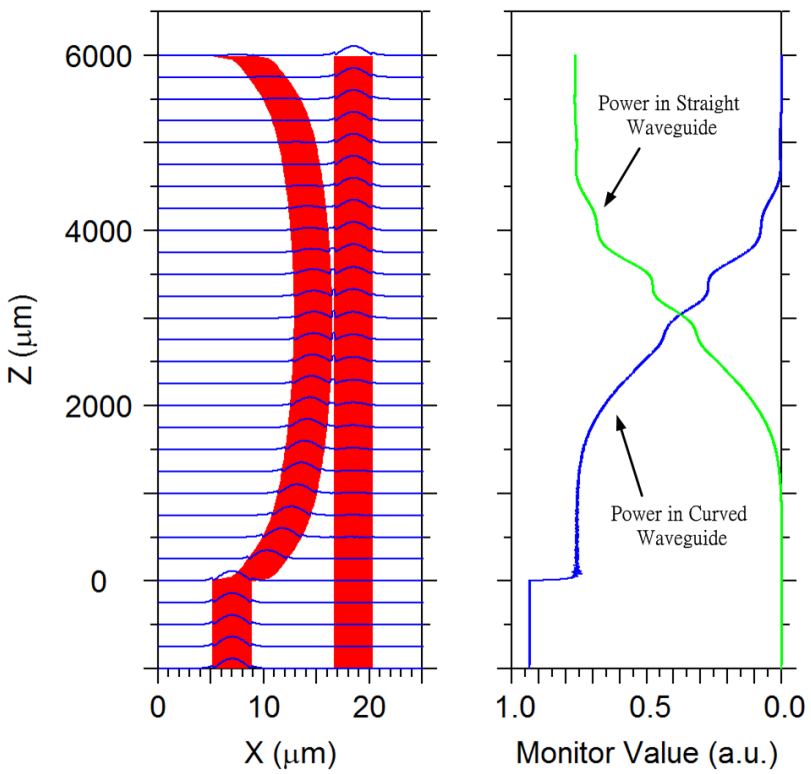


Figure 4.23: The mode evolution and power transfer characteristic for TE mode at $\lambda$ = 10 $\mu$m.

importantly, the technology needed to actually fabricate the proposed design is quite promising and plausible. We believe the realization of such beam combiner will increase the possibility of replacing current beam combiners with the integrated optic counterparts for space-based deep nulling interferometry.

# CHAPTER V

# Conclusion

## 5.1 Summary of research contributions

There are two main goals of the research topics reported in this dissertation. The first goal is to study the limitation and capabilities of optical rate gyroscopes for tactical grade rotation sensing by the introduction of gain into passive integrated optic ring resonator gyros. The ultimate spectral resolution obtainable using an active ring resonator is studied. An expression is derived for this quantum-limited resolution, and the result is applied to determine the fundamental performance limit of a resonant optical gyroscope implemented using an active ring resonator. With the addition of gain, the rms, angular rotation rate, random walk error is shown to decrease by a multiplicative factor equal to the square-root of the ratio of the resonator finesse measured with gain and without gain present. An active, integrated optic, ring resonator is fabricated in a Nd-doped glass by silver ion exchange waveguides. When the gain medium is pumped, the finesse of the 1.6 cm diameter ring resonator is observed to increase from approximately 11 to 250, corresponding to an improvement factor of approximately five.

The second goal is to study and to verify the limitation and capabilities of integrated optic beam combining devices for astronomical imaging. Two-beam and three-beam astronomical beam combiners are fabricated by titanium-indiffused $LiNbO_3$

waveguides. The devices operate in the astronomical L band and the white light fringe in the L band measured by the fabricated two-beam combiner was demonstrated for the first time in the laboratory environment. This result extends the previous integrated optic work for astronomical beam combining to wavelength up to 4 $\mu$m and proves the suitability of replacing traditional beam combining function by integrated optic counterparts for stellar interferometry. Furthermore, the on-chip electrooptic modulation is implemented for our beam combiners utilizing the large EO coefficients of $LiNbO_3$, which provides the potential fringe tracking application for stellar interferometry.

Theoretical design work of a broadband, fully achromatic, polarization-insensitive, mode evolution beam combiner operating in the astronomical N band is presented. The mathematical formulations for the analysis of the proposed device are detailed. The candidates of possible practical device fabrication technology are discussed. The design based on the heterostructure germanium on silicon raised strip waveguide is verified by the numerical simulation and the beam propagation methods. We believe the realization of such device will greatly contribute to the area of nulling interferometry, especially for the space-based mid-infrared nulling interferometers designed for the direct detection and the characterization of Earth-like planets around nearby stars.

## 5.2 Future work

We have demonstrated in this dissertation that active integrated optic devices for sensing applications are beneficial. For the active ring resonator project, we have shown the possibility of the realization of high finesse active ring resonators and lasers through rare earth doping of the ring, and also derived an expression to estimate the gyro performance in quantum limit. In the future, it will be very interesting to verify this performance prediction by optimized design of the optical gyro and the

experiments.

As for the astronomical beam combiners projects, efforts are on-going in our laboratory to characterize the three-beam combiner using a thermal source and an astronomical InSb focal plane array. The on-sky white light fringe measurement will be a good illustration of the application of IO devices to stellar interferometry. The recent and widespread introduction of the photonic devices for the astronomical instrumentation has led to a new field and the associated neologism *astrophotonics* [90]. The field of mid-infrared integrated optics is still in its infancy. There is every reason to believe, however, that the IO results presented in this dissertation can be extended beyond 4 $\mu$m to the mid-IR (7 $\mu$m – 20 $\mu$m). This effort will require substrate materials that are transparent at mid-infrared wavelengths, such as the chalcogenides [80, 91], germanium, or silicon. Future work includes exploring these longer wavelength materials, associated waveguide fabrication methods, and the fabrication and application of the new broadband, achromatic, IO beam combiners for the next generation stellar and nulling interferometers.

# APPENDICES

# APPENDIX A

# Derivation of Normal Modes of Three Waveguides System

One normal mode of the three coupled waveguides is derived from Eq. (4.6) by assuming that

$$\begin{aligned} a_1(z) &= -a_3(z) = \exp(j\beta_0 z) \\ a_2(z) &= 0 \end{aligned} \tag{A.1}$$

Substituting Eq. (A.1) into Eq. (4.6) yields the antisymmetric normal mode

$$E_0(x, y, z) = \Psi_0(x, y) \exp(j\beta_0 z) \tag{A.2}$$

where

$$\beta_0 = \beta_1 - \kappa_{13} \tag{A.3}$$

$$\Psi_0(x, y) = \begin{pmatrix} \Phi_1(x, y) & \Phi_2(x, y) & \Phi_3(x, y) \end{pmatrix} A_0 \tag{A.4}$$

and

$$A_0 = \begin{pmatrix} 1/\sqrt{2} \\ 0 \\ -1/\sqrt{2} \end{pmatrix} \tag{A.5}$$

Similarly to obtain the two symmetric normal modes we substitute $a_1(z) = a_3(z) = \exp(j\beta_{\pm}z)$ into Eq. (4.6). The two symmetric normal modes can then be expressed as a linear combination of the uncoupled modes $\Phi_a$ and $\Phi_b$, where $\Phi_a = \Phi_2$ and $\Phi_b = 1/\sqrt{2}(\Phi_1 + \Phi_3)$. The amplitudes are chosen such that the normal modes are orthogonal:

$$\begin{aligned} \varphi_+ &= d\Phi_a + e\Phi_b \\ \varphi_- &= -e\Phi_a + d\Phi_b. \end{aligned} \tag{A.6}$$

where $d^2 + e^2 = 1$ and $e, d > 0$. Therefore, the symmetric normal modes of the coupled three waveguides system are of the following forms:

$$E_+(x, y, z) = \Psi_+(x, y) \exp(j\beta_+ z) \tag{A.7}$$

$$E_-(x, y, z) = \Psi_-(x, y) \exp(j\beta_- z) \tag{A.8}$$

where

$$\Psi_+(x, y) = \left[\frac{e}{\sqrt{2}}\Phi_1(x, y) + \frac{e}{\sqrt{2}}\Phi_3(x, y)\right] + d\Phi_2(x, y) \tag{A.9}$$

$$\Psi_-(x, y) = \left[\frac{d}{\sqrt{2}}\Phi_1(x, y) + \frac{d}{\sqrt{2}}\Phi_3(x, y)\right] - e\Phi_2(x, y) \tag{A.10}$$

$\beta_+$ and $\beta_-$ are the corresponding propagation constants of these normal modes. Sub-

stituting $E_+(x, y, z)$ into Eq. (4.6), we obtain

$$\begin{aligned} e \cdot (\beta_+ - \kappa_{13} - \beta_1) &= \kappa_{12}\sqrt{2} \cdot d \\ d \cdot (\beta_+ - \beta_2) &= \kappa_{12}\sqrt{2} \cdot e \end{aligned} \tag{A.11}$$

Letting

$$\begin{aligned} \bar{\beta} &= \frac{1}{2}(\beta_1 + \beta_2 + \kappa_{13}) \\ \Delta\beta &= \beta_2 - \beta_1 - \kappa_{13} \\ K &= \sqrt{2}\kappa_{12} \\ X &= \frac{\Delta\beta}{2\sqrt{2}\kappa_{12}} = \frac{\Delta\beta}{2K}, \end{aligned} \tag{A.12}$$

and eliminating $d, e$ from Eq. (A.11), we obtain

$$\beta_+ = \bar{\beta} + K\sqrt{1 + X^2}. \tag{A.13}$$

Substituting $\beta_+$ into Eq. (A.11) and squaring both sides, we get

$$\frac{d^2}{e^2} = \frac{\sqrt{1 + X^2} + X}{\sqrt{1 + X^2} - X} \tag{A.14}$$

From Eq. (A.14) and the constraints $d^2 + e^2 = 1$ and $e, d > 0$, we derive

$$\begin{aligned} d &= \sqrt{\frac{1}{2}(1 + \frac{X}{\sqrt{1 + X^2}})} \\ e &= \sqrt{\frac{1}{2}(1 - \frac{X}{\sqrt{1 + X^2}})} \end{aligned} \tag{A.15}$$

Applying a similar procedure to the $E_-(x, y; z)$ mode yields $\beta_- = \bar{\beta} - K\sqrt{1 + X^2}$ as well as Eq. (A.15).

# APPENDIX B

## Proof of Hermiticity of $B(z)$ Operator

In order to show that $B(z)$ operator is Hermitian, it is sufficient to show that $\partial^2/\partial x^2$ and $\partial^2/\partial y^2$ are Hermitian. We note that if operator $p$ is Hermitian, so is operator $-p^2$ since

$$\begin{aligned} < \Phi_1| - p^2|\Phi_2 > &=< \Phi_1| - p \cdot p|\Phi_2 > \\ &= - < p\Phi_1|p|\Phi_2 > \text{ since p is Hermitian} \\ &= - < p(p\Phi_1)|\Phi_2 >=< -p^2\Phi_1|\Phi_2 > \end{aligned} \tag{B.1}$$

Now let $p = i\frac{\partial}{\partial x}$ or $i\frac{\partial}{\partial y}$, then

$$\begin{aligned} < \Phi_1|p|\Phi_2 > &= \int_y \int_x \Phi_1^*(i\frac{\partial}{\partial x})\Phi_2 \, dxdy \\ &= \int_y \Phi_1^*(i\Phi_2)|_{x=-\infty}^{x=+\infty} \, dy + \int_y \int_x (-i\Phi_2)(\frac{\partial}{\partial x})\Phi_1^* \, dxdy \\ &= \int_y \int_x -i\Phi_2(\frac{\partial}{\partial x})\Phi_1^* \, dxdy =< p\Phi_1|\Phi_2 > . \end{aligned} \tag{B.2}$$

where the last line follows from the fact that $\Phi_2(x, y) = 0$ when $x \to \pm\infty$ for any physical waveguide mode. Therefore, $i\frac{\partial}{\partial x}$ and $\partial^2/\partial x^2$ are Hermitian. Similarly, $i\frac{\partial}{\partial y}$

and $\partial^2/\partial y^2$ are Hermitian too. Thus the $B(z)$ operator is Hermitian.

# APPENDIX C

## Eigenvalue Equation for Coefficients $C_{iq}(z)$

Substituting the $\Psi_+(x, y; z)$ local normal mode of the coupled system as given by Eq. (4.108) into Eq. (4.101), we obtain

$$\begin{aligned} B_{1+2+3} \cdot \Psi_+ &= c_{1+} B_{1+2+3} \Psi_1 + c_{2+} B_{1+2+3} \Psi_2 \\ &= c_{1+} \left( B_{1+3} + \frac{k_0^2 \Delta n_2^2}{2\beta_0} \right) \Psi_1 + c_{2+} \left( B_2 + \frac{k_0^2 (\Delta n_1^2 + \Delta n_3^2)}{2\beta_0} \right) \Psi_2 \\ &= \beta_1 c_{1+} \Psi_1 + \beta_2 c_{2+} \Psi_2 + c_{1+} \frac{k_0 \Delta n_2^2}{2n_0} \Psi_1 + c_{2+} \frac{k_0 (\Delta n_1^2 + \Delta n_3^2)}{2n_0} \Psi_2 \\ &= \beta_+ \Psi_+ \\ &= \beta_+ c_{1+} \Psi_1 + \beta_+ c_{2+} \Psi_2. \end{aligned} \tag{C.1}$$

By forming inner product of Eq. (C.1) with $\Psi_1$ and using Eq. (4.107), we get

$$\beta_1 c_{1+} + \beta_2 c_{2+} S + c_{1+} \kappa_{11} + c_{2+} \kappa_{12} = \beta_+ c_{1+} + \beta_+ c_{2+} S, \tag{C.2}$$

where $\kappa_{ij}$ is defined by Eq. (4.111), (4.112), and (4.113). Similarly, by forming inner product of Eq. (C.1) with $\Psi_2$, we get

$$\beta_1 c_{1+} S + \beta_2 c_{2+} + c_{1+} \kappa_{21} + c_{2+} \kappa_{22} = \beta_+ c_{1+} S + \beta_+ c_{2+}. \tag{C.3}$$

By applying a similar procedure to the $\Psi_-(x, y; z)$ local normal mode, we obtain

$$\beta_1 c_{1-} + \beta_2 c_{2-} S + c_{1-}\kappa_{11} + c_{2-}\kappa_{12} = \beta_- c_{1-} + \beta_- c_{2-} S, \tag{C.4}$$

$$\beta_1 c_{1-} S + \beta_2 c_{2-} + c_{1-}\kappa_{21} + c_{2-}\kappa_{22} = \beta_- c_{1-} S + \beta_- c_{2-}. \tag{C.5}$$

It is easily verified that Eqs. (C.2), (C.3), (C.4), and (C.5) can be written as

$$\begin{pmatrix} B_{11}(z) & B_{12}(z) \\ B_{21}(z) & B_{22}(z) \end{pmatrix} \cdot \begin{pmatrix} c_{1+}(z) & c_{1-}(z) \\ c_{2+}(z) & c_{2-}(z) \end{pmatrix} = \begin{pmatrix} 1 & S(z) \\ S(z) & 1 \end{pmatrix} \cdot \begin{pmatrix} c_{1+}(z) & c_{1-}(z) \\ c_{2+}(z) & c_{2-}(z) \end{pmatrix} \cdot \begin{pmatrix} \beta_+(z) & 0 \\ 0 & \beta_-(z) \end{pmatrix} \tag{C.6}$$

where the matrix representation of the $B(z)$ operator of the coupled system is defined as

$$\begin{pmatrix} B_{11}(z) & B_{12}(z) \\ B_{21}(z) & B_{22}(z) \end{pmatrix} = \begin{pmatrix} 1 & S(z) \\ S(z) & 1 \end{pmatrix} \cdot \begin{pmatrix} \beta_1(z) & 0 \\ 0 & \beta_2(z) \end{pmatrix} + \begin{pmatrix} \kappa_{11}(z) & \kappa_{12}(z) \\ \kappa_{21}(z) & \kappa_{22}(z) \end{pmatrix} \tag{C.7}$$

# APPENDIX D

## Derivation of Coefficients $C_{iq}(z)$

In order to solve equations (4.109) and (4.114) simultaneously, it is useful to introduce a square root matrix Q such that

$$\Lambda = \begin{pmatrix} 1 & S(z) \\ S(z) & 1 \end{pmatrix} = \begin{pmatrix} q_{11}(z) & q_{12}(z) \\ q_{21}(z) & q_{22}(z) \end{pmatrix}^2 = Q^2. \tag{D.1}$$

$\Lambda$ is a Hermitian matrix, and hence it can be diagonalized. Thus Q is easily found to be

$$\begin{aligned} Q &= \begin{pmatrix} q_{11}(z) & q_{12}(z) \\ q_{21}(z) & q_{22}(z) \end{pmatrix} \\ &= \frac{1}{2} \begin{pmatrix} \sqrt{1+S} + \sqrt{1-S} & \sqrt{1+S} - \sqrt{1-S} \\ \sqrt{1+S} - \sqrt{1-S} & \sqrt{1+S} + \sqrt{1-S} \end{pmatrix} \\ &= \begin{pmatrix} \cos\frac{\phi(z)}{2} & \sin\frac{\phi(z)}{2} \\ \sin\frac{\phi(z)}{2} & \cos\frac{\phi(z)}{2} \end{pmatrix}. \end{aligned} \tag{D.2}$$

Let a new matrix, $C'_{iq}(z)$, be defined by

$$\begin{pmatrix} c'_{1+}(z) & c'_{1-}(z) \\ c'_{2+}(z) & c'_{2-}(z) \end{pmatrix} = \begin{pmatrix} q_{11}(z) & q_{12}(z) \\ q_{21}(z) & q_{22}(z) \end{pmatrix} \cdot \begin{pmatrix} c_{1+}(z) & c_{1-}(z) \\ c_{2+}(z) & c_{2-}(z) \end{pmatrix} \tag{D.3}$$

Substituting Eq. (D.1), Eq. (D.2), and Eq. (D.3) into equations (4.109) and (4.114), we obtain

$$\begin{aligned} &\begin{pmatrix} B'_{11}(z) & B'_{12}(z) \\ B'_{21}(z) & B'_{22}(z) \end{pmatrix} \begin{pmatrix} c'_{1+}(z) & c'_{1-}(z) \\ c'_{2+}(z) & c'_{2-}(z) \end{pmatrix} \\ &= \begin{pmatrix} c'_{1+}(z) & c'_{1-}(z) \\ c'_{2+}(z) & c'_{2-}(z) \end{pmatrix} \begin{pmatrix} \beta_+(z) & 0 \\ 0 & \beta_-(z) \end{pmatrix} \end{aligned} \tag{D.4}$$

$$\begin{pmatrix} c'_{1+}(z) & c'_{1-}(z) \\ c'_{2+}(z) & c'_{2-}(z) \end{pmatrix}^t \begin{pmatrix} c_{1+}(z) & c_{1-}(z) \\ c_{2+}(z) & c_{2-}(z) \end{pmatrix} = \begin{pmatrix} 1 & 0 \\ 0 & 1 \end{pmatrix} \tag{D.5}$$

where

$$\begin{pmatrix} B'_{11}(z) & B'_{12}(z) \\ B'_{21}(z) & B'_{22}(z) \end{pmatrix} = Q^{-1} \begin{pmatrix} B_{11}(z) & B_{12}(z) \\ B_{21}(z) & B_{22}(z) \end{pmatrix} Q^{-1}. \tag{D.6}$$

From Eq. (D.2), we can compute the inverse of Q matrix to get

$$\begin{aligned} Q^{-1} &= \frac{1}{2\sqrt{1-S^2}} \begin{pmatrix} \sqrt{1+S}+\sqrt{1-S} & \sqrt{1-S}-\sqrt{1+S} \\ \sqrt{1-S}-\sqrt{1+S} & \sqrt{1+S}+\sqrt{1-S} \end{pmatrix} \\ &= \frac{1}{\cos\phi} \begin{pmatrix} \cos\frac{\phi(z)}{2} & -\sin\frac{\phi(z)}{2} \\ -\sin\frac{\phi(z)}{2} & \cos\frac{\phi(z)}{2} \end{pmatrix}. \end{aligned} \tag{D.7}$$

Substituting Eq. (D.7) into Eq. (D.6) and using Eq. (4.110), we obtain

$$\begin{pmatrix} B'_{11}(z) & B'_{12}(z) \\ B'_{21}(z) & B'_{22}(z) \end{pmatrix} = \begin{pmatrix} \bar{\beta}(z) + \delta'_{12}(z) & \kappa'_{12}(z) - \gamma(z) \\ \kappa'_{12}(z) + \gamma(z) & \bar{\beta}(z) - \delta'_{12}(z) \end{pmatrix}. \tag{D.8}$$

where

$$\bar{\beta}(z) = \frac{\beta_1 + \kappa_{11} + \beta_2 + \kappa_{22}}{2(1-S^2)} - \frac{S}{2(1-S^2)}(\kappa_{12} + \kappa_{21} + S\beta_1 + S\beta_2). \tag{D.9}$$

$$\delta'_{12}(z) = \frac{\beta_1 + \kappa_{11} - (\beta_2 + \kappa_{22})}{2\sqrt{1-S^2}} \tag{D.10}$$

$$\kappa'_{12}(z) = \frac{\kappa_{12} + \kappa_{21}}{2(1-S^2)} - \frac{S}{1-S^2}\frac{\kappa_{11} + \kappa_{22}}{2}, \tag{D.11}$$

$$\gamma(z) = \frac{1}{2\sqrt{1-S^2}}(S\beta_1 - S\beta_2 + \kappa_{21} - \kappa_{12}). \tag{D.12}$$

When the coupling is weak (i.e. $S^2 \ll 1$), $\gamma(z)$ can be approximated as [1] by neglecting terms of order $S^2$ and smaller in the numerator

$$\gamma(z) \approx \frac{1}{2(1-S^2)}(S\beta_1 - S\beta_2 + \kappa_{21} - \kappa_{12}). \tag{D.13}$$

If we further make the reasonable assumption that $\frac{|\beta_2 - \beta_1|}{|\beta_2|} \ll 1$ and $\frac{|\kappa_{12} - \kappa_{21}|}{|\kappa_{12}|} \ll 1$, then $\gamma(z)$ can be neglected compared with $\kappa'_{12}(z)$. The matrix $B'$ is then Hermitian and is of the following form

$$\begin{pmatrix} B'_{11}(z) & B'_{12}(z) \\ B'_{21}(z) & B'_{22}(z) \end{pmatrix} = \begin{pmatrix} \bar{\beta}(z) + \delta'_{12}(z) & \kappa'_{12}(z) \\ \kappa'_{12}(z) & \bar{\beta}(z) - \delta'_{12}(z) \end{pmatrix}. \tag{D.14}$$

By diagonalizing matrix $B'$, the eigenvalues and eigenvectors of Eq. (D.4) can be found

[1] $\frac{1}{\sqrt{1-S^2}} = \frac{\sqrt{1-S^2}}{1-S^2} = \frac{1+O(S^2)}{1-S^2}$.

and the solutions automatically satisfy Eq. (D.5) since the matrix $B'$ is Hermitian and its eigenvectors are orthogonal. The simultaneous eigensolutions are found to be

$$\beta_{\pm}(z) = \bar{\beta}(z) \pm \sqrt{\delta'_{12}(z)^2 + \kappa'_{12}(z)^2} \tag{D.15}$$

and

$$\begin{aligned}
&\begin{pmatrix} c'_{1+}(z) & c'_{1-}(z) \\ c'_{2+}(z) & c'_{2-}(z) \end{pmatrix} = \frac{1}{\sqrt{(\delta'_{12}(z) + \sqrt{\delta'_{12}(z)^2 + \kappa'_{12}(z)^2})^2 + \kappa'_{12}(z)^2}} \\
&\times \begin{pmatrix} \delta'_{12}(z) + \sqrt{\delta'_{12}(z)^2 + \kappa'_{12}(z)^2} & -\kappa'_{12}(z) \\ \kappa'_{12}(z) & \delta'_{12}(z) + \sqrt{\delta'_{12}(z)^2 + \kappa'_{12}(z)^2} \end{pmatrix} \\
&\equiv \begin{pmatrix} \cos\frac{\theta(z)}{2} & -\sin\frac{\theta(z)}{2} \\ \sin\frac{\theta(z)}{2} & \cos\frac{\theta(z)}{2} \end{pmatrix}
\end{aligned} \tag{D.16}$$

where

$$\tan\theta(z) = \frac{\kappa'_{12}(z)}{\delta'_{12}(z)}. \tag{D.17}$$

Thus using Eq. (D.3) and (D.7), the coefficients $C_{iq}(z)$ can be found

$$\begin{aligned}
&\begin{pmatrix} c_{1+}(z) & c_{1-}(z) \\ c_{2+}(z) & c_{2-}(z) \end{pmatrix} = Q^{-1} \cdot \begin{pmatrix} c'_{1+}(z) & c'_{1-}(z) \\ c'_{2+}(z) & c'_{2-}(z) \end{pmatrix} \\
&= \frac{1}{\cos\phi(z)} \begin{pmatrix} \cos\frac{\phi(z)}{2} & -\sin\frac{\phi(z)}{2} \\ -\sin\frac{\phi(z)}{2} & \cos\frac{\phi(z)}{2} \end{pmatrix} \cdot \begin{pmatrix} \cos\frac{\theta(z)}{2} & -\sin\frac{\theta(z)}{2} \\ \sin\frac{\theta(z)}{2} & \cos\frac{\theta(z)}{2} \end{pmatrix} \\
&= \frac{1}{\cos\phi(z)} \begin{pmatrix} \cos\frac{\theta(z)+\phi(z)}{2} & -\sin\frac{\theta(z)+\phi(z)}{2} \\ \sin\frac{\theta(z)-\phi(z)}{2} & \cos\frac{\theta(z)-\phi(z)}{2} \end{pmatrix}.
\end{aligned} \tag{D.18}$$

# APPENDIX E

## Derivation of Nonadiabatic Term $\xi_{+-}(z)$

If we denote $\frac{\partial}{\partial z}\Psi_i = \dot{\Psi}_i$, then the nonadiabatic term, $\xi_{+-}(z)$, can be evaluated as follows by using Eq. (4.108)

$$\begin{aligned}
\xi_{+-}(z) &= < \Psi_+ | \dot{\Psi}_- > \\
&= < c_{1+}\Psi_1 + c_{2+}\Psi_2 | \dot{c}_{1-}\Psi_1 + c_{1-}\dot{\Psi}_1 + \dot{c}_{2-}\Psi_2 + c_{2-}\dot{\Psi}_2 > \\
&= c_{1+}\dot{c}_{1-} + c_{1+}\dot{c}_{2-} < \Psi_1 | \Psi_2 > + c_{1+}c_{2-} < \Psi_1 | \dot{\Psi}_2 > \\
&\quad + c_{2+}\dot{c}_{1-} < \Psi_2 | \Psi_1 > + c_{2+}c_{1-} < \Psi_2 | \dot{\Psi}_1 > + c_{2+}\dot{c}_{2-} \\
&= c_{1+}\dot{c}_{1-} + c_{1+}\dot{c}_{2-}S + c_{1+}c_{2-} < \Psi_1 | \dot{\Psi}_2 > \\
&\quad + c_{2+}\dot{c}_{1-}S + c_{2+}c_{1-} < \Psi_2 | \dot{\Psi}_1 > + c_{2+}\dot{c}_{2-}. \qquad \text{(E.1)}
\end{aligned}$$

Note that by integrating by parts, it is easily shown that

$$< \Psi_1 | \dot{\Psi}_2 > = - < \Psi_2 | \dot{\Psi}_1 > . \qquad \text{(E.2)}$$

Therefore, the nonadiabatic term becomes

$$\begin{aligned}\xi_{+-}(z) =& c_{1+}\dot{c}_{1-} + c_{1+}\dot{c}_{2-}S - c_{1+}c_{2-} < \Psi_2|\dot{\Psi}_1 > \\ &+ c_{2+}\dot{c}_{1-}S + c_{2+}c_{1-} < \Psi_2|\dot{\Psi}_1 > + c_{2+}\dot{c}_{2-}.\end{aligned} \tag{E.3}$$

Using Eq. (4.119) and the fact that $S = \sin\phi$ (can be derived from Eq. (D.2)), each term of right hand side of Eq. (E.3) can be calculated as follows

$$c_{1+}\dot{c}_{1-} = \frac{\cos\frac{\theta+\phi}{2}}{\cos\phi}\left[\frac{-\cos\phi\cos\frac{\theta+\phi}{2}\cdot(\dot{\theta}+\dot{\phi})}{2\cos^2\phi} - \frac{\sin\frac{\theta+\phi}{2}\sin\phi\cdot\dot{\phi}}{\cos^2\phi}\right] \tag{E.4}$$

$$Sc_{1+}\dot{c}_{2-} = \sin\phi\frac{\cos\frac{\theta+\phi}{2}}{\cos\phi}\left[\frac{-\cos\phi\sin\frac{\theta-\phi}{2}\cdot(\dot{\theta}-\dot{\phi})}{2\cos^2\phi} + \frac{\cos\frac{\theta-\phi}{2}\sin\phi\cdot\dot{\phi}}{\cos^2\phi}\right] \tag{E.5}$$

$$(c_{2+}c_{1-} - c_{1+}c_{2-}) < \Psi_2|\dot{\Psi}_1 >= -\frac{1}{\cos\phi} \tag{E.6}$$

$$Sc_{2+}\dot{c}_{1-} = -\sin\phi\frac{\sin\frac{\theta-\phi}{2}}{\cos\phi}\left[\frac{\cos\phi\cos\frac{\theta+\phi}{2}\cdot(\dot{\theta}+\dot{\phi})}{2\cos^2\phi} + \frac{\sin\frac{\theta+\phi}{2}\sin\phi\cdot\dot{\phi}}{\cos^2\phi}\right] \tag{E.7}$$

$$c_{2+}\dot{c}_{2-} = \frac{\sin\frac{\theta-\phi}{2}}{\cos\phi}\left[\frac{-\cos\phi\cos\frac{\theta-\phi}{2}\cdot(\dot{\theta}-\dot{\phi})}{2\cos^2\phi} + \frac{\cos\frac{\theta-\phi}{2}\sin\phi\cdot\dot{\phi}}{\cos^2\phi}\right] \tag{E.8}$$

After rearranging the terms, Eq. (E.3) can be further simplified as

$$\begin{aligned}\xi_{+-}(z) =& -\frac{1}{\cos\phi} < \Psi_2|\dot{\Psi}_1 > \\ &- \frac{\dot{\theta}}{2\cos^2\phi}\left[\frac{1+\cos(\theta+\phi)}{2} + \frac{1-\cos(\theta-\phi)}{2} + 2\sin\phi\sin\frac{\theta-\phi}{2}\cos\frac{\theta+\phi}{2}\right] \\ &+ \frac{\dot{\phi}}{2\cos^2\phi}\left\{\cos\theta\cos\phi + \frac{\sin\phi[\sin(\theta+\phi)-\sin(\theta-\phi)]}{\cos\phi} - \frac{2\cos\theta\sin^2\phi}{\cos\phi}\right\} \\ =& -\frac{1}{\cos\phi} < \Psi_2|\dot{\Psi}_1 > -\frac{1}{2}\dot{\theta} - \frac{\cos\theta}{2\cos\phi}\dot{\phi}\end{aligned} \tag{E.9}$$

# BIBLIOGRAPHY

# BIBLIOGRAPHY


[1] S. E. Miller, "Integrated Optics: an introduction," Bell Syst. Tech. J. **48,** 2059 (1969).

[2] P. Kern, F. Malbet, I. Schanen-Duport, and P. Benech, "Integrated optics single-mode interferometric beam combiner for near infrared astronomy," AstroFib '96, Integrated Optics for Astronomical Interferometry pp. 195–204 (1996).

[3] H. Ishikawa, "Fully Adiabatic Design of Waveguide Branches," J. Lightwave Technol. **25,** 1832–1840 (2007).

[4] C. K. Madsen, G. Lenz, A. J. Bruce, M. A. Cappuzzo, L. T. Gomez, and R. E. Scotti, "Integrated all-pass filters for tunable dispersion and dispersion slope compensation," IEEE Photon. Technol. Lett. **11,** 1623–1625 (1999).

[5] S. T. Chu, B. E. Little, W. Pan, T. Kaneko, and K. Y., "A second-order filter response from parallel coupled glass microring resonators," IEEE Photon. Technol. Lett. **11,** 1426–1428 (1999).

[6] G. Priem, P. Dumon, W. Bogaerts, D. V. Thourhout, G. Morthier, and B. R., "Optical bistability and pulsating behavior in silicon-on-insulator ring resonator structures," Opt. Express **13,** 9623–9628 (2005).

[7] Q. Xu and M. Lipson, "All-optical logic based on silicon micro-ring resonators," Opt. Express **15,** 924–929 (2007).

[8] A. Ksendzov and Y. Lin, "Integrated optics ring-resonator sensors for protein detection," Opt. Lett. **30,** 3344–3346 (2005).

[9] P. Mottier and P. Pouteau, "Solid state optical gyrometer integrated on silicon," Electron. Lett. **33,** 1975–1977 (1997).

[10] R. B. Smith, *Selected papers on fiber optic gyroscopes* (SPIE Optical Engineering Press, Bellingham, Washington, 1989).

[11] W. K. Burns, *Optical fiber rotation sensing* (Academic Press, San Diego, CA., 1993).

[12] S. Ezekiel and S. R. Balsamo, "Passive ring resonator laser gyroscope," Appl. Phys. Lett. **30,** 478–480 (1977).

[13] R. E. Meyer, S. Ezekiel, D. W. Stowe, and V. J. Tekippe, "Passive fiber-optic ring resonator for rotation sensing," Opt. Lett. **8,** 644–646 (1983).

[14] J. Haavisto and G. A. Pajer, "Resonance effects in low-loss ring waveguides," Opt. Lett. **5,** 510–512 (1980).

[15] R. G. Walker and C. D. W. Wilkinson, "Integrated optical ring resonators made by silver ion-exchange in glass," Appl. Opt. **22,** 1029–1035 (1983).

[16] G. Li, K. A. Winick, H. C. Griffin, and J. Hayden, "Systematic modeling study of channel waveguide fabrication by thermal silver ion exchange," Appl. Opt. **45,** 1743–1755 (2006).

[17] R. Adar, M. R. Serbin, and V. Mizrahi, "Less than 1 dB per meter propagation loss of silica waveguides measured using a ring resonator," J. Lightwave Technol. **12,** 1369–1372 (1994).

[18] T. Kitagawa, K. Hattori, Y. Hibino, and Y. Ohmori, "Laser Oscillation in Erbium-Doped Silica-Based Planar Ring Resonators," In Proceedings of $18^{th}$ European Conf. on Optical Commun. **Th PD-II 5,** 907–910 (1992).

[19] W. Sohler, B. K. Das, D. Dey, S. Reza, H. Suche, and R. Ricken, "Erbium-doped lithium niobate waveguide lasers," IEICE Trans. Electron. **E88-C,** 990–997 (2005).

[20] T. A. Dorschner, H. A. Haus, H. M., I. W. Smith, and H. Statz, "Laser gyro at quantum limit," J. Quantum Electron. **QE-16,** 1376–1379 (1980).

[21] N. Yazdi, F. Ayazi, and K. Najafi, "Micromachined inertial sensors," Proc. IEEE **86,** 1640–1659 (1998).

[22] H. Xie and G. K. Fedder, "Integrated micro electromechanical gyroscopes," J. Aerosp. Engrg. **16,** 65–75 (2003).

[23] S. Ezekiel, S. P. Smith, and F. Zarinetchi, in *Optical fiber Rotation Sensing* (Academic Press, New York, US, 1994), Chap. 1.

[24] L. F. Stokes, M. Chodorow, and H. J. Shaw, "All-single-mode fiber resonator," Opt. Lett. **7,** 288–290 (1982).

[25] K. Suzuki, K. Takiguchi, and K. Hotate, "Monolithically integrated resonator microoptic gyro on silica planar lightwave circuit," J. Lightwave Technol. **18,** 66–72 (2000).

[26] H. Ma, X. Zhang, Z. Jin, and C. Ding, "Waveguide-type optical passive resonator gyro using phase modulation spectroscopy technique," Optical Engineering Letters **45,** 080506–1–080506–3 (2006).

[27] H. Okamura and K. Iwatsuki, "A finesse-enhanced Er-doped-fiber ring resonator," J. Lightwave Technol. **9,** 1554–1560 (1991).

[28] J. T. Kringlebotn, "Amplified fiber ring resonator gyro," IEEE Photon. Technol. Lett. **4,** 1180–1183 (1992).

[29] J. T. Kringlebotn, P. R. Morkel, C. N. Pannell, D. N. Payne, and R. I. Laming, "Amplified fibre delay line with 27000 recirculations," Electron. Lett. **28,** 201–202 (1992).

[30] W. T. Silfvast, in *Laser Fundamentals* (Cambridge University Press, 2004), Chap. 6.

[31] W. T. Silfvast, in *Laser Fundamentals* (Cambridge University Press, 2004), Chap. 7.

[32] T. Izawa and H. Nakagome, "Silver ion-exchanged glass waveguides," Appl. Phys. Lett. **21,** 584–586 (1972).

[33] S. I. Najafi, *Introduction to glass integrated optics* (Artech House, Boston, US, 1992).

[34] T. Findakly, "Glass waveguides by ion exchange: a review," Opt. Eng. **24,** 244–250 (1985).

[35] R. V. Ramaswamy and R. Srivastava, "Recent advances in ion-exchanged optical waveguides and components," J. Mod. Opt. **35,** 1049–1067 (1988).

[36] R. V. Ramaswamy and R. Srivastava, "Ion-exchanged glass waveguides: a review," J. Lightwave Technol. **6,** 984–1001 (1988).

[37] G. Li, Ph.D. thesis, University of Michigan, Ann Arbor, 2006.

[38] S. P. Divakaruni and S. J. Sanders, "Fiber optic gyros - a compelling choice for high precision applications," paper MC2, Optical Fiber Sensors (OFS) (2006).

[39] J. P. Berger and D. Segransan, "An introduction to visibility modeling," New Astronomy Reviews **51,** 576–582 (2007).

[40] M. Born and E. Wolf, in *Principles of optics*, seventh ed. (Cambridge University Press, 1999), Chap. 10.

[41] A. A. Michelson, "Measurement of Jupiter's satellites by interference," Nature(London) **45,** 160 (1891).

[42] T. T. Brummelaar, M. Creech-Eakman, and J. Monnier, "Probing stars with optical and near-IR interferometry," Physics Today pp. 28–33 (2009).

[43] J. I. Lunine, B. Macintosh, and S. Peale, "The detection and characterization of exoplanets," Physics Today pp. 46–51 (2009).

[44] S. Brustlein, L. D. Rio, A. Tonello, L. Delage, F. Reynaud, H. Herrmann, and W. Sohler, "Laboratory demonstration of an infrared-to-visible up-conversion interferometer for spatial coherence analysis," Phys. Rev. Lett. **100,** 153903 (2008).

[45] J. P. Berger, K. Rousselet-Perraut, P. Kern, F. Malbet, I. Schanen-Duport, F. Reynaud, P. Haguenauer, and P. Benech, "Integrated optics for astronomical interferometry. II. First laboratory white-light interferograms," Astron. Astrophys. Suppl. Ser. **139,** 173–177 (1999).

[46] P. Haguenauer, J. P. Berger, K. Rousselet-Perraut, P. Kern, F. Malbet, I. Schanen-Duport, and P. Benech, "Integrated optics for astronomical interferometry. III. Optical validation of a planar optics two-telescope beam combiner," Appl. Opt. **39,** 2130–2139 (2000).

[47] J. Berger, P. Haguenauer, P. Kern, K. Rousselet-Perraut, F. Malbet, I. Schanen, M. Severi, R. Millan-Gabet, and W. Traub, "Integrated optics for astronomical interferometry. IV. First measurements of stars," Astron. Astrophys. **376,** L31–L34 (2001).

[48] E. Laurent, K. Rousselet-Perraut, P. Benech, J. P. Berger, S. Gluck, P. Haguenauer, P. Kern, F. Malbet, and I. Schanen-Duport, "Integrated optics for astronomical interferometry. V. Extension to the K band," Astron. Astrophys. **390,** 1171–1176 (2002).

[49] J. B. LeBouquin *et al.*, "Integrated optics for astronomical interferometry. VI. Coupling the light of the VLTI in K band," Astron. Astrophys. **450,** 1259–1264 (2006).

[50] B. Mennesson, J. M. Mariotti, V. C. d. Foresto, G. Perrin, S. Ridgway, W. A. Traub, N. P. Carleton, M. G. Lacasse, and G. Mazé, "Thermal infrared stellar interferometry using single-mode guided optics: first results with the TISIS experiment on IOTA," Astron. Astrophys. **346,** 181–189 (1999).

[51] G. Li, T. Eckhause, K. A. Winick, J. D. Monnier, and J. P. Berger, "Integrated optic beam combiners in lithium niobate for stellar interferometer," Proc. SPIE **6268,** 626834 (2006).

[52] R. A. Becker, R. H. Rediker, and T. A. Lind, "Wide-bandwidth guided-wave electro-optic intensity modulator at $\lambda = 3.39$ $\mu$m," Appl. Phys. Lett. **46,** 809–811 (1985).

[53] M. A. Johnson, A. L. Betz, and C. H. Townes, "10-micron heterodyne stellar interferometer," Phys. Rev. Lett. **33,** 1617–1620 (1974).

[54] A. Labeyrie, "Interference fringes obtained on Vega with two optical telescopes," Astrophys. J. **196,** L71–L75 (1975).

[55] J. Breckinridge and C. Lindensmith, "The astronomical search for origins," Optics and Photonics News **16,** 24–29 (2005).

[56] C. V. M. Fridlund, "The Darwin mission," Advances in Space Research **34,** 613–617 (2004).

[57] P. R. Lawson, W. A. Traub, and S. C. Unwin, "Exoplanet Community Report," Technical report, NASA (2009) .

[58] R. N. Bracewell, "Detecting nonsolar planets by spinning infrared interferometers," Nature **274,** 780–781 (1978).

[59] P. R. Lawson *et al.*, "Terrestrial planet finder interferometer 2007-2008 progress and plans," Proc. SPIE **7013,** 70132N (2008).

[60] W. A. Traub, K. W. Jucks, and C. Noecker, "Biomarkers on extrasolar terrestrial planets: estimates of detectability," $197^{th}$ AAS Meeting, #49.03, Bulletin of the Ameri. Astro. Society **32,** 1485 (2000).

[61] A. Labeyrie, S. G. Lipson, and P. Nisenson, *An introduction to optical stellar interferometry* (Cambridge University Press, New York, US, 2006).

[62] R. V. Roussev, Ph.D. thesis, Stanford University, 2006.

[63] K. S. Chiang, "Construction of refractive-index profiles of planar dielectric waveguides from the distribution of effective indexes," J. Lightwave Technol. **3,** 385–391 (1985).

[64] E. Strake, G. P. Bava, and I. Montrosset, "Guided modes of Ti:$LiNbO_3$ channel waveguides: a novel quasi-analytical technique in comparison with the scalar finite-element method," J. Lightwave Technol. **6,** 1126–1135 (1988).

[65] K. K. Wong, in *Properties of Lithium Niobate* (INSPEC, 2002), Chap. 8.

[66] J. D. Monnier, "Asymmetric beam combination for optical interferometry," Publications of the Astronomical Society of the Pacific **113,** 639–645 (2001).

[67] W. J. Minford, S. K. Korotky, and R. C. Alferness, "Low-loss Ti:$LiNbO_3$ waveguide bends at $\lambda = 1.3$ $\mu$m," IEEE Journal of Quant. Elect. **QE-18,** 1802–1806 (1982).

[68] Y. Sakamaki, T. Saida, M. Tamura, T. Hashimoto, and H. Takahashi, "Low loss crosstalk waveguide crossings designed by wavefront matching method," IEEE Photon. Technol. Lett. **18,** 2005–2007 (2006).

[69] R. C. Alferness, R. V. Schmidt, and E. H. Turner, "Characteristics of Ti-diffused lithium niobate optical directional couplers," Appl. Opt. **18,** 4012–4016 (1979).

[70] K. Okamoto, in *Fundamentals of Optical Waveguides* (Academic Press, 2000), Chap. 4.

[71] K. Kishioka, "A design method to achieve wide wavelength-flattened responses in directional coupler-type optical power splitters," J. Lightwave Technol. **19,** 1705–1715 (2001).

[72] R. O. Gappinger, R. T. Diaz, A. Ksendzov, P. R. Lawson, O. P. Lay, K. M. Liewer, F. M. Loya, S. R. Martin, E. Serabyn, and J. K. Wallace, "Experimental evaluation of achromatic phase shifters for mid-infrared starlight suppression," Appl. Opt. **48,** 868–880 (2009).

[73] R. O. Gappinger, J. K. Wallace, R. D. Bartos, D. R. Macdonald, and K. A. Brown, "Current progress on TPFI nulling architectures at Jet Propulsion Laboratory," Proc. SPIE **5905,** 55–61 (2005).

[74] R. D. Peters, O. P. Lay, and M. Jeganathan, "Broadband phase and intensity compensation with a deformable mirror for an interferometric nuller," Appl. Opt. **47,** 3920–3926 (2008).

[75] M. Born and E. Wolf, in *Principles of Optics*, seventh ed. (Cambridge University Press, 1999), Chap. 8.

[76] J. Gay, Y. Rabbia, and P. Baudoz, "Le coronographe interferential achromatique," C.R. Acad. Sci. Paris **325,** 51–56 (1997).

[77] G. T. Paloczi, A. Eyal, and A. Yariv, "Wavelength-insensitive nonadiabatic mode evolution couplers," IEEE Photonics Technology Letters **16,** 515–517 (2004).

[78] T. Tamir, in *Guided-Wave Optoelectronics*, 2nd ed. (Springer-Verlag, 1990), Chap. 3.

[79] H. Haus, W. Huang, S. Kawakami, and N. Whitaker, "Coupled-mode theory of optical waveguides," J. Lightwave Technol. **5,** 16–23 (1987).

[80] N. Ho, M. C. Phillips, H. Qiao, P. J. Allen, K. Krishnaswami, B. J. Riley, T. L. Meyers, and N. C. Anheier Jr., "Single-mode low-loss chalcogenide glass waveguides for mid-infrared," Opt. Lett. **31,** 1860–1862 (2006).

[81] J. Hu, V. Tarasov, N. Carlie, N.-N. Feng, L. Petit, A. Agarwal, K. Richardson, and L. Kimerling, "Si-CMOS-compatible lift-off fabrication of low-loss planar chalcogenide waveguides," Opt. Express **15,** 11798–11807 (2007).

[82] R. A. Soref, S. J. Emelett, and W. R. Buchwald, "Silicon waveguide components for the long-wave infrared region," J. Opt. A: Pure Appl. Opt. **8,** 840–848 (2006).

[83] R. A. Soref, "The Past, Present, and Future of Silicon Photonics," J. Sel. Top. Quantum Electron. **12,** 1678–1687 (2006).

[84] R. A. Soref and J. P. Lorenzo, "Single-crystal silicon: a new material for 1.3 and 1.6 $\mu$m integrated optical components," Electron. Lett. **21,** 953–954 (1985).

[85] R. A. Soref and B. R. Bennett, "Electrooptical Effects in Silicon," J. Quantum Electron. **QE-23,** 123–129 (1987).

[86] M. Lipson, "Silicon photonics: the optical spice rack," Electron. Lett. **45,** 576–578 (2009).

[87] A. Nayfeh, Ph.D. thesis, Stanford University, 2006.

[88] H. H. Li, "Refractive index of silicon and germanium and its wavelength and temperature derivatives," J. Phys. Chem. Ref. Data **9,** 561–658 (1980).

[89] V. M. Schneider and H. T. Hattori, "High-tolerance power splitting in symmetric triple-mode evolution couplers," IEEE Journal of Quant. Elect. **36,** 923–930 (2000).

[90] J. Bland-Hawthorn and P. Kern, "Astrophotonics: a new era for astronomical instruments," Optics Express **17,** 1880–1884 (2009).

[91] L. Labadie *et al.*, "Recent progress in mid infrared integrated optics for nulling interferometry," Proc. SPIE **6268,** 62682E (2006).